IJCOE
COASTAL, OFFSHORE & ENVIRONMENTAL ENGINEERING

Volume 5 | Issue 3 | Oct 2020

Seismic Design of Subsea Spool per ISO: Part III- Analysis & Design
Sirous Yasseri

Underwater Terrain and Gravity aided inertial navigation based on Kalman filter
Mohammad Reza Khalilabadi

The effect of Caspian Sea level rise on the environment of the sand dunes of Mazandaran, Iran
Homayoun Khoshravan; Tahereh Alinejad; Alireza Naqinezhad; Samereh Tirgan

Positioning Using Classification and Regression: Case study of Oman Sea
Ali Ghorbani; Mohammad Reza Khalilabadi

An analytical and field study on influence of breakwaters on beach morphological evolution: a case study (Astara Port)
Sahar Javansamadi; Ali Karami khaniki; Abbas Ali Aliakbari Bidokhti; Kamran Lary; Majid Ghodsi Hasanabad

A Parametric Study of Critical Buckling Force in Snaked Lay Pipelines under HP/HT Condition
Yasaman Rezaie; Seyed Mohammad Hossein Sharifi; Gholam Reza Rashed; Farzad Numani

www.ijcoe.org info@ijcoe.org 19

International Journal of Coastal, Offshore and Environmental Engineering (IJCOE) Vol. 5, Issue 3

Since 2015

International Journal of Coastal, Offshore & Environmental Engineering

ISSN: 2980-8731 (online)

Volume 5 | Issue 3| Oct 2020

IJCOE

Editor-in-Chief: Prof. Hamid S. Dana

International Journal of Coastal, Offshore & Environmental Engineering
Since 2015
ISSN: 2980-8721 (online)

In The Name of God

Message from the Editor-in-Chief

The IJCOE journal office was established in 2015,and its first issue was published in 2016. TheIJCOE covers a wide range of research in thefields of oceanography & ocean technology, aswell as marine industries & marine engineering.The editorial board of IJCOE consists of nearly130 of the greatest scientists and researchersfrom over 30 countries worldwide, and thejournal's review board comprises 1,000 membersfrom all five continents. The membership andapplication process for joining the editorial andreview boards of this journal is ongoing. IJCOE isa research-academic quarterly journal that haspublication and distribution permissions fromthe Press Organization and permission topublish scientific-research articles from theMinistry of Science, Research, and Technology(MSRT) with an "A" rating. It also holds a "Q1"rating from the ISC institute with an impactfactor (IF) of approximately 0.43 and isconsidered a "core journal" (prestigious andoutstanding journal). IJCOE is an open-accessjournal and allows the download and receipt ofaccepted articles in full text for free. It respectsand adheres to copyright and COPE regulations.The journal's office operates 24/7, providingservices to researchers. In addition to publishinga regular quarterly journal, IJCOE has 16 specialissues on specific topics in preparation. It alsoprovides conditions for publishing specializedbooks, references, and handbooks. Moreover, itis ready to cooperate with the secretariats ofreputable international conferences to publishtheir selected and outstanding articles. IJCOEevaluates, appraises, and publishes books,articles, and the scientific achievements andfindings of esteemed researchers and scientistsworldwide who are innovating and conductingin-depth research in the "important and strategicfield of the maritime technology & Oceanengineering." It welcomes any form of jointcooperation with universities, research institutes,and related research centers at the national,regional, and international levels, and extends ahand for collaboration.

Classification of Editorial Board in IJCOE

Editor-in-Chief

Director-in-Chief

Deputy Editor

Executive Managers

English Text Editor

Technical Editor

International Editorial Board

National Editorial Board

Editorial Board Associate

Editorial Board Assistant

Guest Editorial Board

Advisory Board

Administrative Coordinator

Honorary Board Member

Methodology Advisor

Author Benefits

- Open Access
- Rapid Publication
- Thorough Peer-Review
- No Copyright Constraints
- Coverage by Leading Indexing Services
- Discounts On Article Processing Charges (APC)
- No Space Constraints, No restriction on the maximum length of the papers, number of figures or colors

INTERNATIONAL JOURNAL OF IJCOE COASTAL, OFFSHORE & ENVIRONMENTAL ENGINEERING

Aims of IJCOE

Hydrodynamics

Marine equipment

Structural mechanics

Ocean environmental predictions

Stochastic calculations Experimental

Automatic Control of Marine Systems

Scope of IJCOE

Marine Hazards

Ocean Acoustics

Naval Architecture

Ocean Engineering

Coastal Engineering

Marine Meteorology

Marine Earth Sciences

Underwater Technology

Marine Renewable Energy

Polar & Arctic Engineering

Marine Renewable Energy

Marine Geography & Geodesy

Marine Environmental Engineering

Automatic Control of Marine Systems

Hydro Physics & Physical Oceanography

Type of papers

- Case Studies
- Book Reviews
- Review Article
- Letters to the Editor
- Methodology Papers
- Editorials and Commentaries
- Response or Rejoinder Papers
- Perspective or Opinion Papers
- Conceptual or Theoretical Papers
- Meta-Analysis and Systematic Reviews
- Short Communications or Brief Reports
- Research Articles (Original Research Papers)

Scientific Research Journal

Ministry of Science, Research And Technology (MSRT)

Jurnal Ranking 2023: A

Ministry Of Science, Research And Technology (ISC)

Citation Impact 2022: 0.429

Quartile 2022 : Q1

Core Collection

IJCOE is a Member of

Cantact Us

Office 1 | Research Institute of Meteorology and Atmospheric Science

Address | Tehran, Shahid Kharrazi Highway, Pajoohesh Blvd, Research Institute of Meteorology and Atmospheric Science, Sand and Dust Storm International Research Center (SDS-IRC), No. 13, 1st floor.

Phone | +982144787652

Postal code | 13611-14977

website | www.rimac.ac.ir

Office 2 | Iranian National Institute for Oceanography and Atmospheric Science

Address | Tehran, Dr. Fatemi Gharbi St., Shahid Etemadzade St., No. 3, third floor.

Phone | +982166944873

Postal code | 13389 – 14118

website | www.inio.ac.ir

Email | Info@ijcoe.org

Website | www.ijcoe.org

Follow Us

www.ijcoe.org

INTERNATIONAL JOURNAL OF IJCOE COASTAL, OFFSHORE & ENVIRONMENTAL ENGINEERING

Volume & Issue:

Volume 5, Issue 3, October 2020

Number of Articles: 6

Content

INTERNATIONAL JOURNAL OF
COASTAL & OFFSHORE ENGINEERING IJCOE Vol.5/No. 3/Fall 2020 (1-14)

Available online at www. ijcoe.org

Seismic Design of Subsea Spool per ISO: Part III- Analysis & Design

Sirous F. Yasseri

Brunel University London; Sirous.Yasseri@Brunel.ac.uk;

ARTICLE INFO

Article History:
Received: 28 Aug. 2020
Accepted: 29 Dec. 2020

Keywords:
Subsea Spools
Abaqus modeling
ISO 19902
ISO 19901
ASME VIII 2011a
ALE and ELE

ABSTRACT

This is the final part of a three-part paper that presents the methodology, data needed, code check of 12-inch ID rigid pools, describing the design methodology, and key design parameters for performing the analyses. Discussion of the state of art regarding the soil data is covered in Part I. Part II is dedicated to describing ISO 19901 and 19902 seismic qualification and the derivation of design time histories.

For each cluster end, there are two parallel flowlines each individually terminated with a Flowline Termination Assembly (FTA). The FTA is free to move axially on its foundation to absorb movement caused by the flowline expansion and walking. Lateral movement is restricted by lateral stops on the foundation. Two separate spools will then be connected to a single Pigging Loop Module with a piled foundation. A diver-less horizontal collet connector system will be used for the tie-in at both ends of the spool.

The analysis methodology which assumes the seabed is a compliant plate, is described in this paper. For validation purposes, a couple of configurations were used to create a full three-dimensional model where the soil was modeled using the solid element with Moh-Columb behavior. These results are not presented in this paper.

1. Introduction

This is the Part III of a three-part paper [12 and 13] which describes the spool design, FE analyses, and the resulting geometrical configuration and also covers the following areas:

- Detailed design by analyses demonstrating spools are fit for purpose
- Checks of spool-ends reaction loads at connection-points to PMA and FTA under operational and seismic events

The following issues are not addressed here

- Assessment of the susceptibility of spools to VIV and FIV
- Fatigue due to flowline cyclic thermal expansion and contraction
- The design of the connector system, PMA, and foundation.

A typical layout of the manifold and well clusters including the PMA to FTA & PMA to PMA spools is shown in Figure 1.

The design methodology to be employed in the spool design is present in this part.

There are several design constraints imposed by the current architecture and installation equipment which limit the spool size.

Chang et al [5] and Peng et al [11] described in some detail the effect of ISO code on the seismic design; see also [9] and [10].

2. Key design parameters

Key design parameters are given in this section. It is to be noted that all of these parameters were used in the design of spools. There were many hundreds of analysis, but only a handful of results are given in this paper.

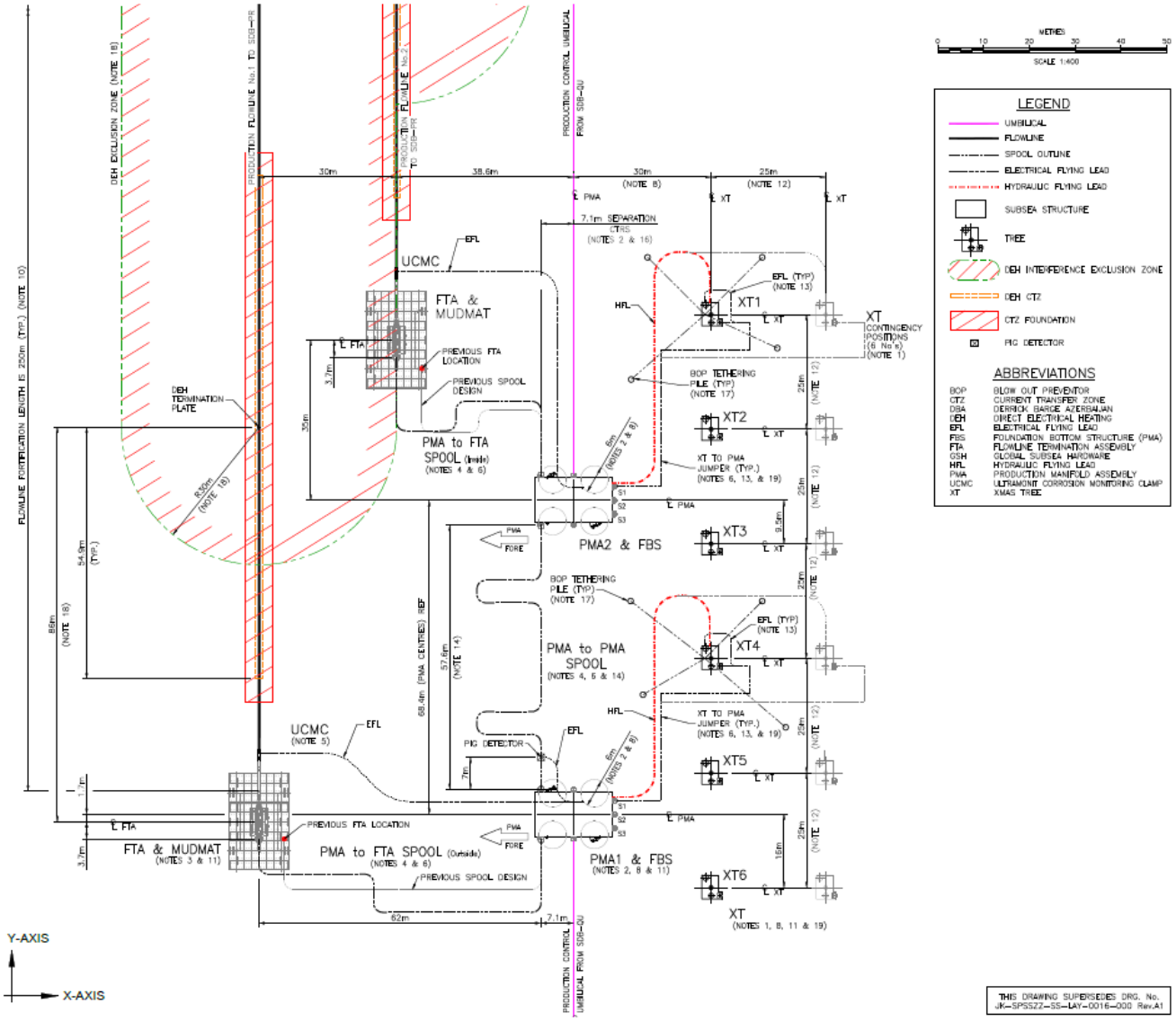

Figure 1: Cluster Layout – Plan View

Design Code-Spools were designed using "Design by Analysis Method" following ASME VIII 2011a, Div. 2 Part 5 [3].

Table 1: Material Data

Parameter	Value
Pipe	SMLS
Grade	X65
Steel Density	7850 kg/m^3
Young's Modulus @ 20°C	207 GPa
Poisson ratio	0.3
SMYS @ 20°C	450 MPa
SMTS @ 20°C	535 MPa
Thermal Expansion Coefficient	11.7 x 10^{-6}
Thermal Conductivity	45 W/m.K
Ovality	1% OD (Max. 4mm)
Wall Thickness Tolerance	+/-12.3%

Table 2: Wall Thickness Data

Parameter	PMA to FTA Spool and FTA Piping
Nominal Diameter	304.8mm ID 391.3mm OD
Nominal Wall Thickness	38.75mm +/-12.3%
CRA Total Overlay	4.5mm
CRA overlay wastage allowance	3mm

Material Data -The pipe material data for the spools and the flowlines are presented in Table 1

Spool Wall Thickness- The spool wall thickness determination has employed a 'no burst' criteria at SIWHP (785 barg). The nominal design wall thickness is 36mm however due to manufacturing limitations a suitably sized pipe has been selected (Table 2). An internal Corrosion Resistant Alloy overlay of Alloy 625 (UNS N06625) is attached to the carbon steel pipe. The CRA strength has not been accounted for in the

wall thickness determination. The thickness selected is based on a predicted accumulated erosion loss of 3mm over the entire field life. The spools shall be of constant ID to allow the passage of intelligence pigs.

Design Pressure and Temperature- Pressure and temperature data for the FTA spools are presented in Table 3.

Table Error! No text of specified style in document.**: Pressure and Temperature Data.**

Parameter	Value
Design Pressure	325barg
Burst Pressure Rating	785barg (SIWHP)
Max Design Temp	90 °C
Min Design Temp	-29 °C

Table4: Process Conditions

Analyzed Loading Condition	Pressure (barg)	Temperature (°C)	Density (kg/m^3)
Installation (Flooded)	0	ambient	1010
Leak test	358	ambient	1010
Design	325	90 (1)	50-200 (1120 (2))
SIWHP	785	90	200
Seismic	325	90	200
Shutdown/restart (3)	0 to 325	-29°C to 90°C	50-1120

Notes: 1) Maximum expected FTA inlet temperature during normal operation is 62°C, 2) Maximum operation density used in the analysis is taken as MEG density, 3) Operating values can be considered instead of these values.

Loading and Process Data- Table 4 shows the loading conditions to be analyzed and the respective pressure and temperatures that have been rationalized for each load condition considered in the design for the design conditions including start-up and shut down.

Product Densities- The assumed content densities of the flowlines in various conditions are given in Table 5

Temperature De-rating No de-rating of the steel is required for in the spool design as per ASME VIII, whereby de-rating of the steel does not occur until 121°C (250°F), [4]. However, the current analyses conservatively consider de-rating (SMYS de-rated from 450MPa to 435MPa @ 62ºC).

Table 5. Content Densities

Condition	Density (kg/m3)
Empty	0
Flooded / Hydro-test	1010
Production Flowlines Operation(1)	50 to 200
MEG90	1120

Notes: 1) Typical operational variation excluding liquid slugs potentially accumulated during shutdown/restart.

Wave and Current data - Omni-directional wave data with an associated current and design currents with associated waves have been presented for each location. This has been rationalized to a single set of Metocean data applicable for a generic spool design as shown in Table 6.

Table 6: Simplified Metocean Data to be applied to all Flowlines (Design Current and Associated Wave)

Parameter	1 Yr	10 Yr	100 Yr
Hmax (m) (Most Probable)	9.0	11.6	13.9
THmax (s) (Best Estimate)	7.9	9.0	9.7
Current at 1m above seabed (m/s)	0.49	0.68	0.88
Current at 3m above seabed (m/s)	0.58	0.80	1.03
Current at 5m above seabed (m/s)	0.59	0.83	1.07

Marine Growth- The marine growth will be 30mm with a density of 1325 kg/M^3 which is included in the weight calculations.

Table 7: Summary of Embedment, Axial, and Lateral Friction Factors

Parameter	For Manifolds		
	LB	BE	UB
Embedment (%/D_{oc} [1])	8%	26%	39%
Axial Friction Factor	0.20	0.39	0.97
Lateral Breakout Friction Factor	0.20	0.33	0.90
Lateral Residual Friction Factor	0.32	0.50	0.84

Note 1: Overall external diameter, D_{oc} is taken as 607.8 mm

Pipe-Soil Interaction Data - The non-linear spools-soil interaction responses using the recommendation of [14] methodology are presented as 'friction factors', μ (i.e. soil resistance divided by vertical pipe load). The evaluated spool embedment, axial, and lateral friction factors for the spools-piece are summarised in Table. These parameters are to be used in the PMA-FTA and

PMA-PMA spools-piece FE analysis design.

Seismic- Two levels of seismic activity (see Part II [12]) are used, namely:

- Extreme Level Earthquake (ELE);
- Abnormal Level Earthquake (ALE);

Time-domain direct integration analyses were used for seismic analyses. Each record has two horizontal and vertical acceleration components. Sets of seven 3-component time histories provided for ELE and ALE levels were used.

Initially, a set of 10 real strong-motion accelerograms was selected for the analysis. Table 8 lists the time-histories selected, and the specific components of each record used for the analysis. Out of these 10 records, seven histories were chosen to carry out seismic analyses. They are highlighted in blue in Table 8.

Manifold Interface Loads Limits- Connector loads limits on the inboard hub, inner support, and connector cradle at the PMA are provided by the manifold design for the different load cases.

Table 8: Earthquake Time Histories for Analysis

Event	Date	Country	Station	Mag.	Distance (km)	Comp	PGA (g)
Kern County	07/21/1952	USA	Taft Lincoln School Tunnel	7.4	43.5	Y	0.18
Loma Prieta	10/18/1989	USA	Saratoga-Aloha Ave	6.9	27.6	X	0.51
Northridge	01/17/1994	USA	Arleta-Nordhoff Ave. Fire Station	6.7	9.9	X	0.34
Tabas	09/16/1978	Iran	Tabas	7.4	52.0	Y	1.10
Ierissos	08/26/1983	Greece	Ierissos-Police Station	5.1	8.0	X	0.18
Kalamata	09/13/1986	Greece	Kalamata-OTE Building	5.9	11.0	Y	0.27
Imperial Valley	10/15/1979	USA	Cerro Prieto	6.5	26.7	X	0.17
Landers	06/28/1992	USA	Coolwater	7.3	23.0	Y	0.42
Landers	06/28/1992	USA	Desert Hot Spring	7.3	23.0	X	0.17
Izmit	08/17/1999	Turkey	Goynuk-Delvet Hastanesi	7.6	73.0	X	0.14

End Expansion- End expansions were determined in the flowline buckling and walking assessment. The recommended expansion/contraction at this stage is currently +2.2m/-1.0m respectively, to encompass a standard FTA and FTA to PMA spool design across the field.

Settlement- Due to the 'very soft' to 'soft' clays expected in the area with low shear strength, significant embedment may occur. Initial settlement of each structure will vary; a piled PMA structure will differ from a skirted mud-mat FTA foundation causing a greater spool misalignment. Differential settlement of the spool compared with the structures was considered in the spool design. Total long term FTA settlement is 135mm with short term settlement of 10mm, for the FTA, mud-mat, flowline. The maximum post-seismic settlement of FTA is estimated to be 260mm. For the PMA, a long term settlement of around 100mm has been used.

Tie-in Elevations- The PMA tie-in elevation from the seabed to hub centers has been taken as 2.5m with a tolerance of +1.7/-0.0m. The elevation of the center of the FTA inboard hub relative to the seabed is 1.5m, and therefore the minimum height from the seabed of 2.5m was used in the analyses conservatively.

3. Spool Design Methodology

3.1 General

The overall spool design methodology is as follows:

- Determine initial spool dimensions due to the field architecture constraints;
- Determine the shortest and longest spool dimension due to installation tolerances of the tie-in structures considering which legs of the spools will be variable and if any clashes would occur (Figure 2);
- Determine if spool size and weight is installable by available vessels/barges and satisfies crane lift capacities, crane reach, and spool transportation requirements;
- Review Operational safety including any dropped objects/fishing interaction and whether protection is required i.e. mattress protection;
- Review soil conditions to determine soil frictions and whether additional foundation/support is required; Consider end conditions, application of loads from/to interfacing parties;
- Determine boundary conditions (metrology/manufacturing tolerances including allowable tolerances for connector and connector stroking loads);
- Consider differential embedment of the structures and the spool piece. Initial and long term settlement should be considered;
- Perform static non-linear elastic FE analyses;
- Review connector loads and satisfies capacity

checks with interfacing party;

- Perform cyclic analysis, considering start-up and shut down;
- Perform seismic analysis;
- Determine the natural frequency for spool shape, for calculating allowable span lengths ascertaining if VIV may be an issue;
- Perform FIV and FLIP screening
- Perform fatigue assessment including ECA for the welds;
- Perform code stress checks following "Design by Analysis Method" ASME VIII 2011a, Div. 2 Part 5 [3].
- Use spool dimensions that provide the longest total length (including tolerances) to determine if suitable for Process conditions i.e. MEG volumes are feasible;
- Determine Anode requirements.

It is noted that spool wall thickness has been determined using a 'No burst' probability method [Ref. **Error! Reference source not found.**] that does not account for any additional benefit of the CRA strength. Weight and stiffness due to the thickness of the CRA are accounted for in the FE analyses; however, the CRA thickness is ignored in the stress calculations.

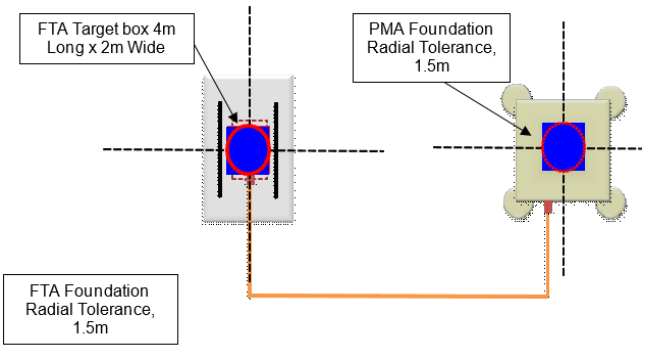

Figure 2 Installation tolerances at the PMA and FTA location

3.2 Design Constraints

There were several design constraints imposed by the combinations of operational and installation system requirements:

- Spool lengths are limited to the transportation barge envelope whereby the maximum envelope is 66m x 14m x 5.5m;
- Increasing spool lengths would impact MEG flush volumes and will have to be reassessed after determining final spool geometry;
- The current separation between FTA centers is approximately 30m laterally with an axial offset of approximately 10m. PMA center to the nearest FTA center separation is currently 30.0m laterally;
- Sizing and weight to remain within crane lift capacities;
- Loads at the PMA spool end has to be checked for limiting loads imposed by the PMA design.

Ensuring the design conforms to the constraints listed above resulted in a complex spool design, particularly for the inner spool. This is due to the minimum lengths required to clear the spool from the DEH influence zone and available space for spool routing whilst remaining within the installation barge envelope and avoiding clashes with the outer spool.

The spool design requires a long lever arm suitable for absorbing the large expansion loads which were challenging based on the current cluster configuration and barge limitations. A significant number of bends (complex geometry) was required to allow sufficient flexibility to avoid overstressing the spool or overloading connectors at the structure of the end (PMA/FTA) if they were to be designed according to ASME B31.8 [4]. An alternative to this (having complex geometry) was to allow for some yielding in the pipe wall following ASME Section VIII 2011a, Division 2 Part 5 [3] "Design by Analysis Method" which was adopted for our design.

Spool sizing has to be determined based on field layout with consideration given to the sizing as a result of installation tolerances.

3.3 Seismic Analyses Methodology

The time history direct integration method was used for seismic analyses. Each record has two horizontal and vertical acceleration components. Sets of seven 3-component time histories of the Manifold locations and for ELE and ALE levels were used to conduct seismic analyses [see part II]. These time histories were specifically produced for Cluster spools matching their fundamental natural period. The time histories have been scaled to the expected natural period of the cluster spools.

The design is in line with the ISO 19901-2 [8] requirements, where for the time history analysis method covering the ALE and ELE event all 7 events have been checked and the design should pass 4 of the 7, in line with the functional requirements associated with each.

Spool's FTA and PMA end were assumed to be connected to FTA and PMA via springs (Which represent FTA and PMA's connector stiffness in each direction) and after applying all static loads including pipeline walking to the FTA end, seismic acceleration records were applied to these two locations plus rigid surface's reference point where the seabed is modeled as rigid surface. Direct integration was conducted to calculate strain and stress at different times.

The main factor in seismic analyses of any structure is considering a suitable form of damping. Two sources of damping in any structure resting on soil are soil hysteretic damping and radiation damping, which are major sources of energy dissipation. These can be implemented by dashpots. Full details of all damping sources and their implementations in soil-structure interaction problems are explained in Appendix C.

In the design of spools, Equation 1(see Part I, [12]) was used to introduce dashpots into the model. In the axial, transverse, and vertical directions the dashpot constant is assumed to be

$$\boldsymbol{C_{rx} = C_{ry} = C_{rz} = D\rho V_s} \qquad (1)$$

Here D is the spool diameter, ρ and v_s are Soil density and shear wave velocity [12]. The recommended values are half as much as recommended by some researchers [2], and less than 1/8 of allowed by ASCE4-98 (quoted Part I, [12]; see also Eurocode [7].

In this work damping related to the rotational degrees of freedom is neglected as per the Berger approach (see [6] and [12].

Using **Error! Reference source not found.** and assuming the following $\rho = 1340\,\frac{\mathrm{kg}}{\mathrm{m}^3}$ and $G_0 = 0.5$ MPa, and assuming the minimum possible ratio of $\frac{G}{G_0} = 0.1$, dashpot constant will be $C = 5000\ \frac{N}{m/s}\ /\mathrm{m}$ and since element length is 0.250m, dashpot to be used is $C = 1250\ \frac{N}{m/s}$. This value was reduced again and value of $C = 750\ \frac{N}{m/s}$ was used in the Abaqus.

The added mass of the pipe, drag, and inertia forces are included in the analyses using Morrison Equations.

The seismic events are described in [13]

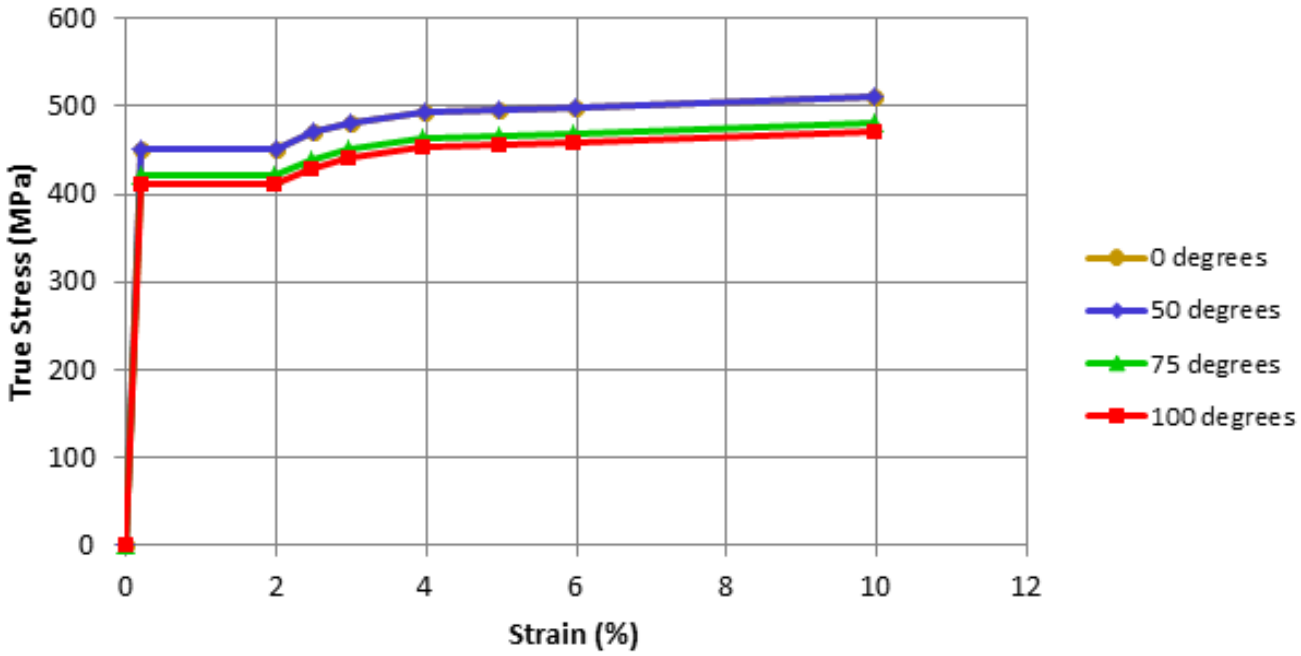

Figure 3: Engineering Stress-Strain Curve

3.4 ASME VIII acceptance criteria

ASME Section VIII 2011a, Division 2 Part 5 [3] "Design by Analysis Method" was used as the guiding code to demonstrate that the designed spools are fit for purpose. This is because as stated in Section 0 using ASME B31.8 [4] factors the spool design required a long lever arm suitable for absorbing the large expansion loads while the spool has to stay in the elastic region behaviour which was challenging based on the current cluster configuration and barge limitations. A significant number of bends (complex geometry) required to allow sufficient flexibility to avoid overstressing the spool. The alternative to this (having complex geometry) is to allow for some yielding in the pipe wall following ASME Section VIII 2011a, Division 2 Part 5 "Design by Analysis Method" [3].

Elastic-Plastic stress analyses following Section 5.2.4.of the code were performed. The assumed engineering stress-strain curves as shown in Figure 2, have been used. The stress-strain curves include the Lüder's plateau effect (typical for heat-treated pipes).

The design-by-analysis requirements are organized based on protection against the failure modes listed below. The component shall be evaluated for each applicable failure mode. If multiple assessment procedures are provided for a failure mode, only one of these procedures must be satisfied to qualify the design of a component. It is noted that the Limit-Load Analyses of 5.2.3 is not applicable as stated in 5.2.3.2

Limitation (b): "Components that experience a reduction in stiffness with deformation, e.g. a pipe elbow under in-plane bending, shall be evaluated using paragraph 5.2.4."; from [3]

(a) Protection against Plastic Collapse

(b) Protection against Local Failure

(c) Protection against Collapse from Buckling

(d) Protection against Failure from Cyclic Loading and temperature de-rating. The stress-strain curve at 62°C has been linearly interpolated and converted to the true stress-strain curve [1] to be used in the Abaqus modelling.

The material elastic perfectly plastic model is based on the minimum yield obtained from Fig 2 (and NOT the smallest of 1/3 SUT and 2/3SyT) hence:

450-14 (for de-rating case T for 62 degree Centigrade) = 436 MPa

The hysteresis loop stress-strain curve of material is schematically shown in Figure 4.

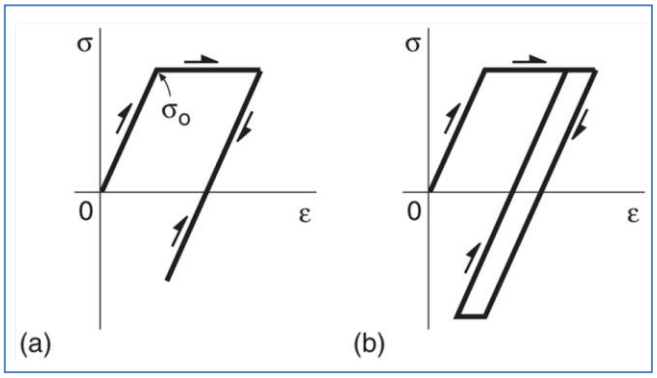

Figure 4: Cyclic Stress-Strain Hysteresis Model

The specific number of load cases due to combinations of the imposed end displacement (misalignment at the connectors due to fabrication and metrology tolerances) is 256 cases. These 256 were run with the identified soil characteristics a) Upper bound soil friction and b) Lower bound soil friction. It is also to be noted that due to installation tolerances (these are tolerances relating to the landing targets of the two ends structures that we can account for it by "cut to suit" during fabrication for each spool) there is a need to analyse two spool sizes, Short and Long spool for each "Inner FTA to PMA", "Outer FTA to PMA" and "PMA to PMA" spool. Therefore the required number of basic analysis runs for one spool is 256x2x2 = 1024 cases for each spool.

4. Abaqus Modeling

4.1 General

The spools were modelled in the general FE program Abaqus. The models were extended from the PMA to the FTA. PMA piping was not included in the model.

The pipe is modelled using a 2-node Elbow 31 element capable of predicting global spool behaviour, particularly in spool bends. Deformation nonlinearity as well as material nonlinearity was included in the analyses. A contact pair is established between the seabed, which is the master surface, and the spool elements which form the slave surface. The seabed reference node is fully fixed throughout the analysis. The seabed surface has the vertical stiffness in such a way to model pipe penetration and seabed friction is also used to provide axial and lateral restraint. The elastoplastic stress-strain relationship (Figure 3) is modelled with temperature de-rated SMYS and SMTS.

The spool analysis does not include any FTA and PMA piping, only the outboard hub of the connector was modelled by including a stiffer element than the spool pipe. The effects of FTA and PMA are modelled using 6 non-linear springs at each end to represent the effect of FTA and PMA stiffness.

Initial analysis will apply boundary conditions, operating loads, expansion, and walking conditions. These initial results will be used to determine a final geometry for developing more sophisticated models and applying seismic and cyclic load conditions.

The spool design will use a generic design for all cluster ends therefore, only three sets of spool geometry will be analyzed; namely inner and outer spools to connect the FTAs to the PMA and middle spool to connect PMA to PMA (see Figure 1).

Different combinations of boundary conditions from FTA and PMA end tolerances have been considered in the analyses. Having six degrees of freedom at each end will produce $(2^6)^2 = 4096$ load cases. To reduce the number of load cases and consider only the critical load cases, two assumptions are considered:

- Two series of analyses for each spool is carried out assuming lower bound friction between spool and seabed and upper bound values. In using lower bound friction values, two ends of the spool are raised vertically up by the total vertical tolerance value and in using upper bound friction values, two ends of the spool are pressed down by the total vertical tolerance. This is because assuming lower bound friction and pressing down two ends of spool does not produce critical results, and also, assuming upper bound friction and raising two ends of the spool is not critical as well.
- Within the connector itself the carrier pipe is free to rotate torsionally during the initial laydown of

the connector, only after tie-in is complete is the torsional movement restricted. So there is no need to consider this degree of freedom in the initial load cases.

Considering the above assumption the number of degrees of freedom to be applied in the analysis reduces from 6 to 4 at each end so the total number of critical load cases reduces to $(2^4)^2$=256 load cases for each of lower bound and upper bound friction factors.

The critical load case which gives higher von-Misses stress is used to perform seismic and cyclic analysis. The spools will be assessed for SIWHP to ensure no loss of containment occurs .i.e. strain-based design.

4.2 Soil Friction

Pipe-soil friction plays an important role in spool design. A typical plot of frictional resistance against displacement is shown in Figure 5 and Figure 6. In the FE analyses, a user subroutine is used to model both residual friction coefficients (axial and lateral) and breakout lateral resistance.

A typical axial pipe-soil interaction relationship used in the present study is defined in Figure 5.

A typical lateral pipe-soil interaction relationship used in the present study is defined in Figure 6.

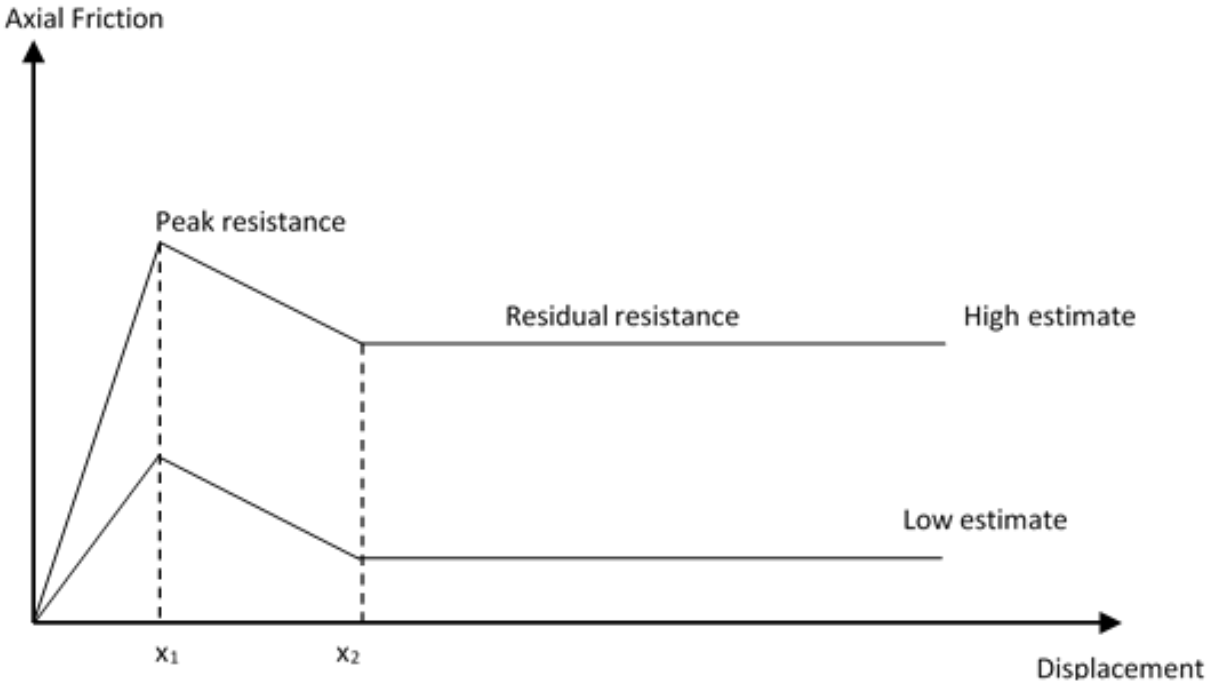

Figure 5: Typical Axial Friction Coefficients

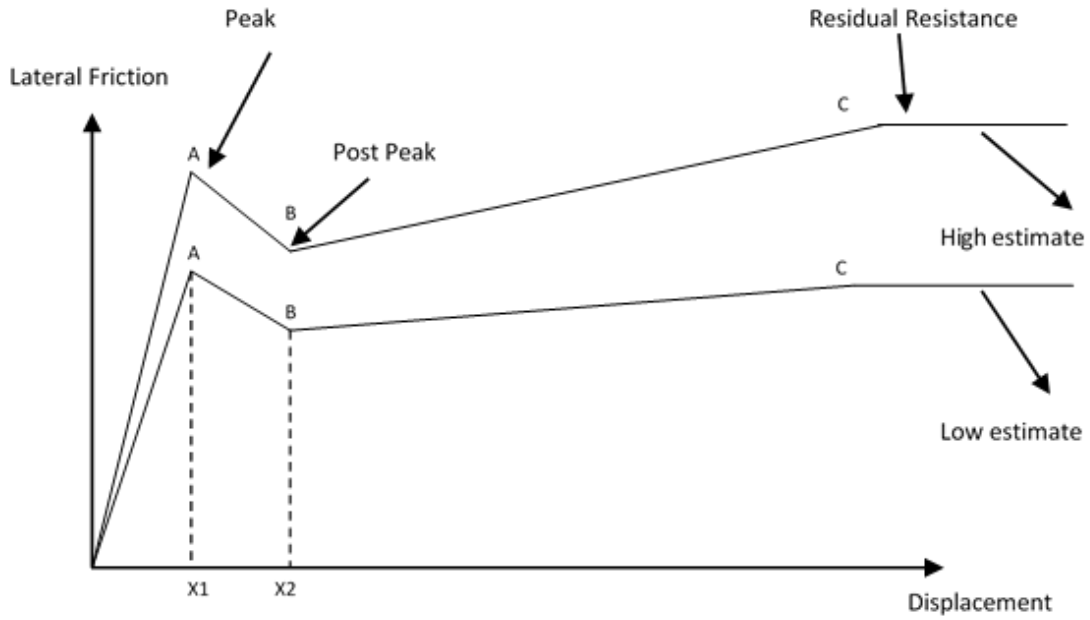

Figure 6: Typical Lateral Friction Coefficients

4.3 FTA and PMA Stiffness

Two ends of the spools are connected to FTA and PMA; both are assumed to be flexible. Assuming fixed ends for spool yield to very unrealistic spools end reactions, so both FTA and PMA stiffness are included in the analyses. Six independent springs at two ends of the spool are assumed to model FTA and PMA stiffness, each of them is to model stiffness of FTA and PMA in each direction (there are 6 degrees of freedom at each end of spool). FTA spring stiffness has been evaluated by JP Kenny Structural team and is in Ref. **Error! Reference source not found.** and PMA stiffness has been evaluated by FMC in Ref. **Error! Reference source not found.**.

4.4 Model geometry

The spool may be modelled using a 2-node Elbow 31 element [1]. Geometric nonlinearity, as well as material nonlinearity, must be accounted for in the analyses. The seabed can be modelled as a rigid analytical surface defined using finite elements. A contact pair is defined between the seabed, which is the master surface, and the spool elements which form the slave surface. The seabed reference node is fully fixed throughout the analysis. The seabed surface has the vertical stiffness to represent the soil vertical stiffness, but the spool is free to lift off. The friction at the interface of the spool and the seabed in axial and lateral directions are defined appropriately.

Different combinations of boundary conditions from FTA and PMA end tolerances have been considered in the analyses. Having six degrees of freedom at each end will produce (26)2 = 4096 load cases. To reduce the number of load cases and consider only the critical load cases, two assumptions are considered:

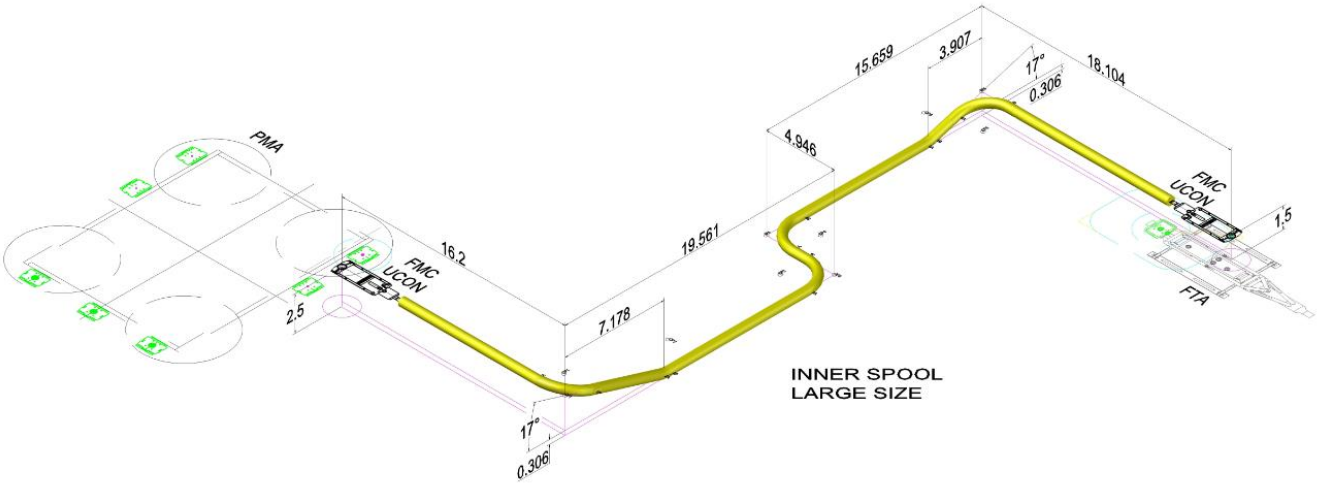

Figure 7: Configuration of Possible Largest Size of Outer Spool based on Installation Tolerances

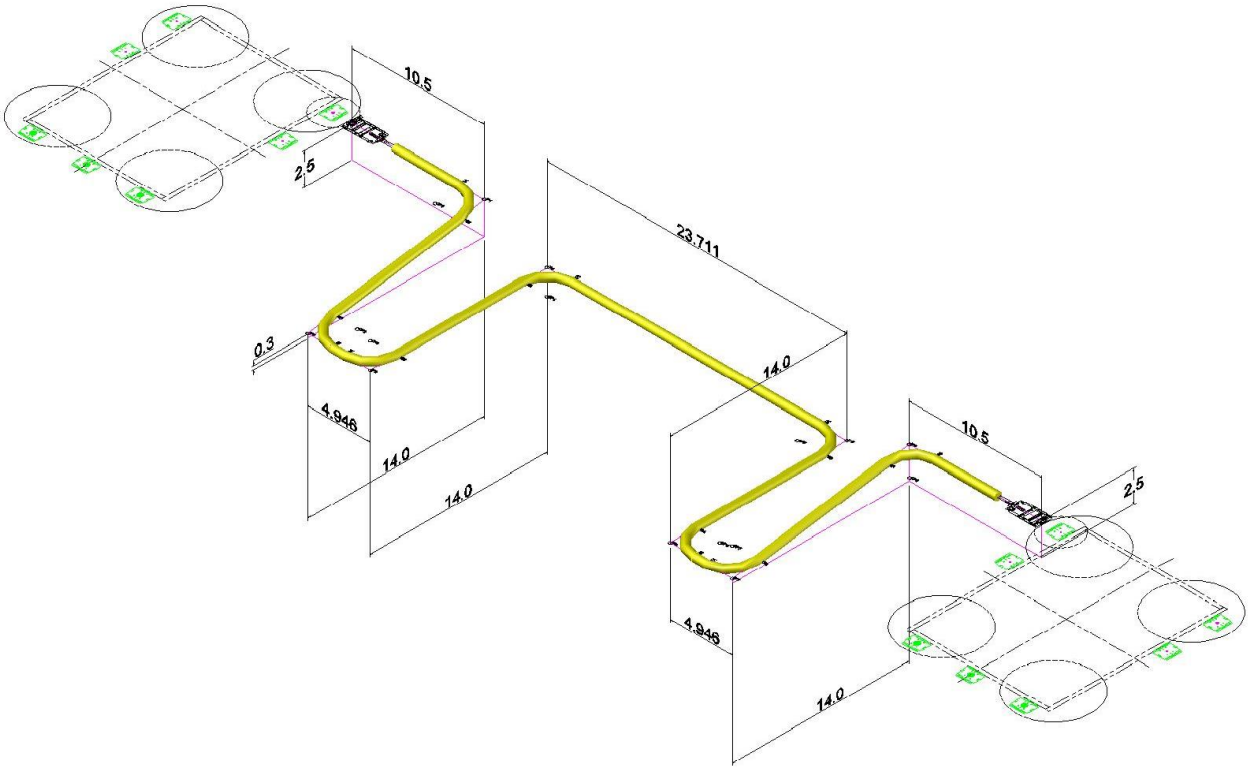

Figure 8: Configuration of Possible Smallest Size of Middle Spool based on Installation Tolerances

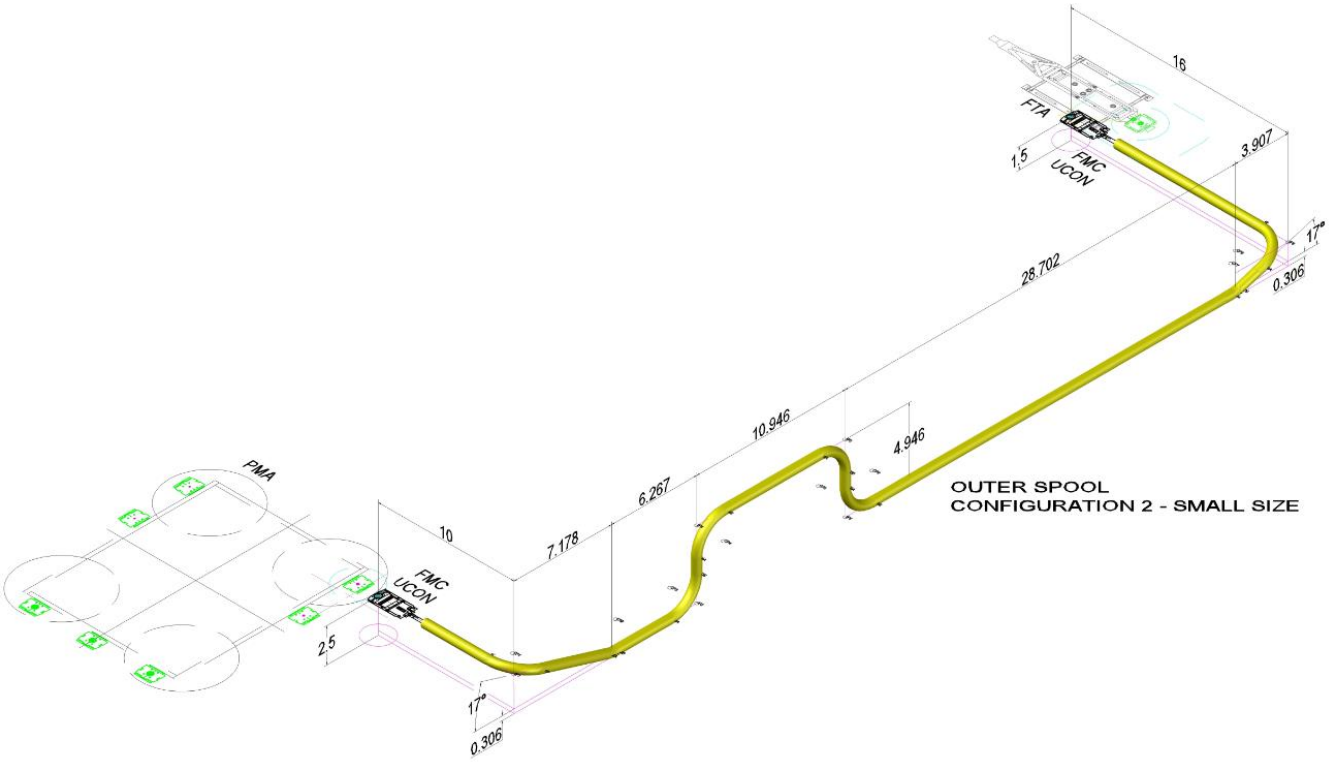

Figure 9: Configuration of Possible Smallest Size of Outer Spool– Configuration 2 based on Installation Tolerances

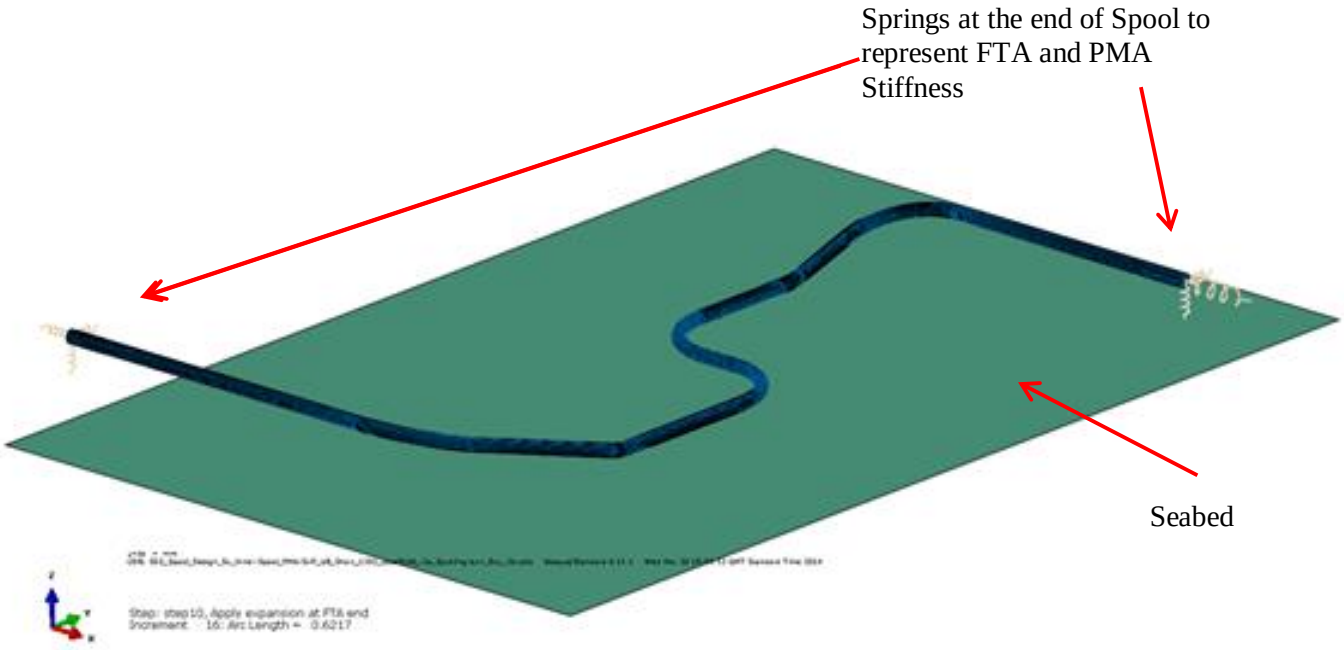

Figure 10- Finite Element Model of Inner Spool using 3D Shell Elements

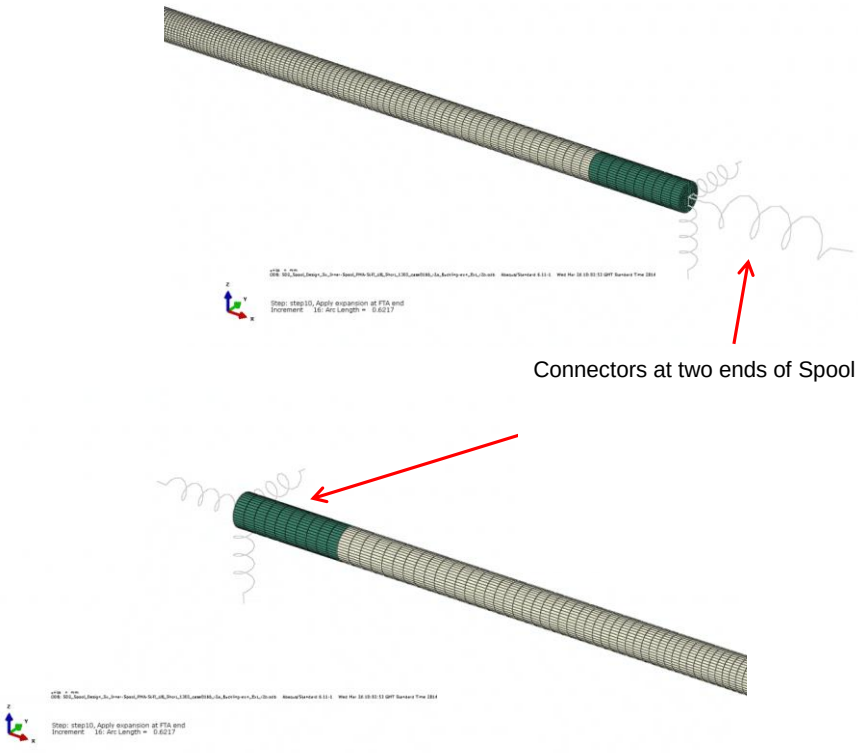

Figure 11- Finite Element Model of Inner Spool using 3D Shell Elements

The final configuration for each spool considering the smallest and longest possible sizes based on installation tolerances was modeled for inner, middle, and outer spools. Figures 7 to 9 show a few examples.

FTA and PMA ends of the spool are connected to 6 springs at each end to represent FTA and PMA stiffness in each degree of freedom (Figure 10). The seabed has been modeled using a rigid surface with vertical stiffness so that spool can embed into it and friction in longitudinal and lateral direction has been given between spool and seabed.

4.5 Abaqus Load Steps

The load steps to be applied in the Abaqus model for a realistic spool model:

1) Submerged weight in empty condition, zero friction, fit pipeline to the seabed;
2) Apply external pressure
3) Restore friction coefficients
4) Release restraints
5) Apply submerged weight in operational condition. For spool analyses, the water-filled spool is assumed.
6) Apply Metrology/ Fabrication/ Land Survey tolerances
7) Stroke FTA end of the spool
8) Stroke PMA end of the spool
9) Apply internal pressure and fix torsional degrees of freedom at two ends of the spool
10) Apply design temperature
11) Apply expansion and walking to FTA end
12) Reduce internal Pressure and temperature to shut-down condition
13) Apply pipeline contraction

Note that friction between pipe and seabed is set initially to zero to facilitate numerical convergence when settling the pipeline on seabed. This value is set to the appropriate value soon after the pipe is settled on the seabed.

Note that seabed was assumed flat in the analyses. Conservatively, the smallest value for PMA height (2.5m) was used. The true variation in height will be known after metrology and can be accounted for by combinations of slight changes to the angles before welding.

Figure11: Inner spool - Smallest Size – Envelope of Von-Mises Stress (MPa)

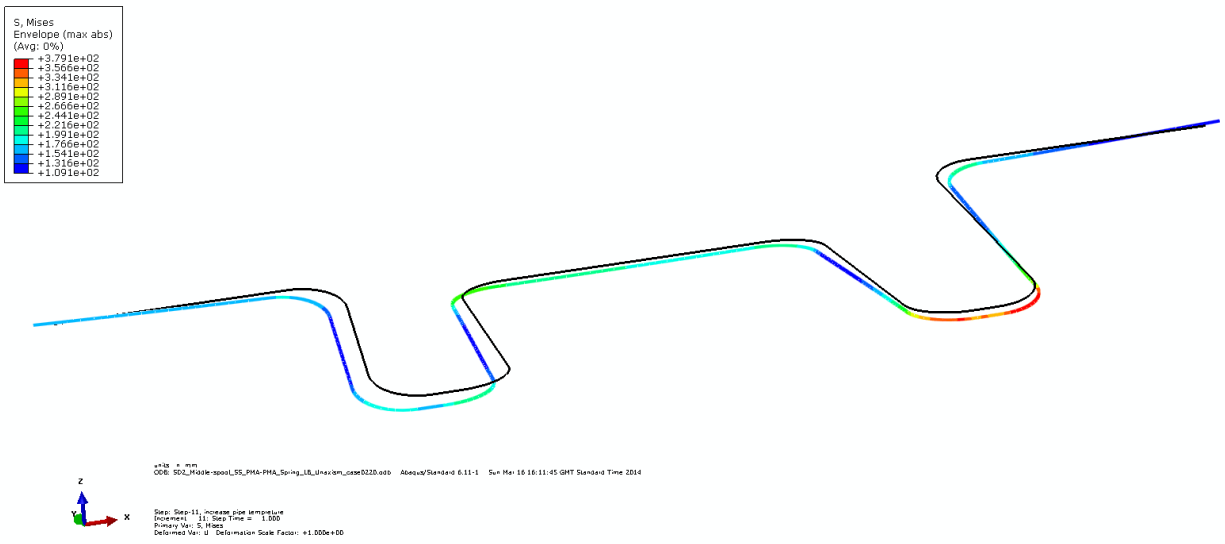

Figure 12: Middle spool - Smallest Size – Envelope of Von-Mises Stress (MPa)

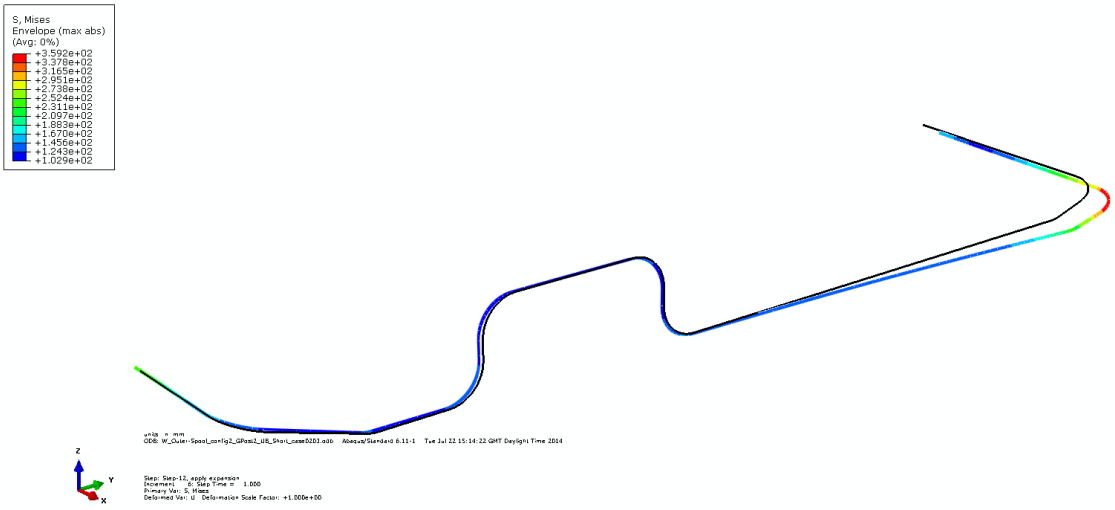

Figure 13: Outer spool – Configuration 2 – Envelope of Von-Mises Stress (MPa)

Figures 11 to 13 show examples of Abaqus' results

Two series of analyses for each spool is carried out assuming lower bound friction between spool and seabed and upper bound values. In using lower bound friction values, two ends of the spool are raised vertically up by the total vertical tolerance value and in using upper bound friction values, two ends of the spool are pressed down by the total vertical tolerance. This is because assuming lower bound friction and pressing down two ends of spool does not produce critical results, and also, assuming upper bound friction and raising two ends of the spool is not critical as well.

Within the connector itself the carrier pipe is free to rotate torsionally during the initial laydown of the connector, only after tie-in is complete is the torsional movement restricted. So there is no need to consider this degree of freedom in the initial load cases.

Considering the above assumption the number of degrees of freedom to be applied in the analysis reduces from 6 to 4 at each end so the total number of critical load cases reduces to $(2^4)^2$=256 load cases for each of lower bound and upper bound friction factors.

5. Concluding Remark

Seismic analysis of rigid spools was presented. Another check must be performed to ensure that the interface loads at the connector ends are compatible with the limiting conditions of the connectors. It is shown that to identify feasible geometries for spools that are fit for purpose according to Design by Analyses method of ASME Viii, Division 2, Part Five [3].

Results for a few of several hundred cases analyzed are presented in this paper. The following observations were made.

- It is reminded that the first step of the cluster spool design is to check spools end reactions against their allowable limit given by subsea connectors
- The shortest size of the Inner spool is the most critical spool in terms of end reactions.
- The reported case is a 12in ID pipe. If the thickness of the ID increases then a practical geometry may not exist, except if the tolerances are tightened or the capacity of the connector is increased. In such a situation flexible pipe might be necessary.
- The larger spool size has enough flexibility to pass the minimum requirement of 5 out of 7 records pass for ELE and ALE.
- As the length increase so does the margin to pass 6 out of 7 seismic records.
- Fatigue life calculations are not reported here, but as assessed using SN were satisfactory.
- Vortex indicated Vibration (VIV) screening checked (not reported here) no potential for VIV was detected.
- FLIP/FIV screening checked (not reported here) and passed, so there is no issue for FLIP/FIV.
- It was shown that suitable geometries can be found that pass the unity checks relating to the loads limit at the PMA for all spools and all conditions of operation and seismic events.
- all translational reactions (i.e. Resultant of FL, FT, and FV) were below allowable resultant of translational loads given by the connector vendor for different conditions,

- torsional reaction (ML) was compared against its corresponding value given by the vendor and resultant bending moment (i.e. Resultant of MT and MV) is compared with their allowable resultant bending moment provided by the vendor.

6. References

1. Abaqus, Simulia by Desualt systems, 2014. Version 13.
2. American Society of Civil Engineers (ASCE), ASCE 7-10, Virginia (2010). *Minimum Design Loads for Buildings and Other Structures*
3. ASME VIII 2011a, Div2 Part 5 *Design By Analysis Requirements*
4. ASME B31.8 Gas *Transmission and Distribution Piping Systems*
5. Chang, B., Abraham, M., and B.-F. Peng, B.F., (20015), *Comparison of ISO and API Seismic Design Guidelines Using Three Existing Offshore Platforms*, OTC 17285, Offshore Technology Conference, Houston, TX, U.S.A., 2–5 May 2005.
6. El Naggar, M. H. & Bentley, K. J., (2000), *Dynamic analysis for laterally loaded piles and dynamic p-y curves*. Canadian Geotechnical Journal, 37, 1166-1183
7. Eurocode 8: Seismic Design of Buildings
8. ISO 19901-2, (2004) Petroleum and Natural Gas Industries - *Specific Requirements for Offshore Structures - Part 2: Seismic Design Procedures and Criteria*
9. Marshall, P.W. and Chang, B, (1996), *Structural Design Considerations*" OTC 8107, Offshore Technology Conference, Houston 1996.
10. Naeim, Farzard, (1989), *The Seismic Design Handbook*, Van Nostrand Reinhold, USA.
11. *Peng. B.F., Abdel Ghoneim, G., (2009), Comparison of ISO and API Seismic Design Requirements for Offshore Structures* Proceedings of the Nineteenth (2009) International Offshore and Polar Engineering Conference Osaka, Japan, June 21-26, 2009
12. Yasseri, S, (2020*), Seismic Design of Subsea Jumper per ISO: Part I- Preliminaries,* IJCOE Vol.4/No. 1/Spring 2020 (31-43)
13. Yasseri, S. (2020), *Seismic Design of Subsea Spool per ISO: Part II- Seismic Requirements*, IJCOE Vol.4/No. 2/Summer 2020 (1-13)
14. SAFEBUCK JIP – Safe Design of Pipelines with Lateral Buckling, Design Guideline, Safebuck III

Abbreviation/ Acronym	**Description**
A	Absolute
BPT	Ball Penetrometer Test
CD	Chart Datum
CDT	Cool Down Time
CPT	Cone Penetrometer Test
CRA	Corrosion Resistant Alloy
CMS	Corrosion Monitoring Spool
DEH	Direct Electrical Heating
ECA	Engineering Critically Assessment
FIV	Flow-Induced Vibration
FLIP	Flow-Induced Pulsation
FE	Finite Elements
FTA	Flowline Termination Assembly
ID	Inside Diameter
LB	Lower Bound
MEG	Mono Ethylene Glycol
PMA	Production Manifold Assembly
OD	Outside Diameter
SIWHP	Shut-in Wellhead Pressure
SMLS	Seamless
TBC	To be confirmed
UB	Upper Bound
VIV	Vortex-Induced Vibrations

INTERNATIONAL JOURNAL OF
COASTAL & OFFSHORE ENGINEERING
IJCOE Vol.5/No. 3/Fall 2020 (15-21)

Available online at: www. Ijcoe.org

Underwater Terrain and Gravity aided inertial navigation based on Kalman filter

Mohammad Reza Khalilabadi *

* *Assistant Professor, Faculty of Naval Aviation, Malek Ashtar University of Technology, Iran;*
khalilabadi@mut.ac.ir

ARTICLE INFO

Article History:
Received: 23 Nov. 2020
Accepted: 13 Jan. 2021

Keywords:
Navigation
Underwater
Terrain aided navigation
Gravity aided navigation
Kalman filter
Two maps aided navigation.

ABSTRACT

In this paper, we present a new method for terrain and gravity aided navigation. Gravity aided navigation and terrain aided navigation are map aided navigation methods for correcting Inertial Navigation System (INS) errors of Autonomous Underwater Vehicles (AUV). Map aided navigation uses the information of the geophysical field maps. For achieve the highest accuracy and reliability two or three map aided navigation systems are combined. In this paper, we proposed a new method that simultaneously uses gravity map data and terrain map data. For maps data fusion we use a Kalman filter which its measurement equation defined based on gravity and terrain of the experiment area. The experimental results are encouraging.

1. Introduction

Autonomous Underwater Vehicle (AUV) navigation is widely used to find the location of underwater vehicles that are doing military or commercial applications. According to the underwater environmental characteristics, the electromagnetic waves cannot propagate in the water, so the common navigation systems like the Global Position System (GPS) are not working in the underwater[1–5]. Also using active methods like active sonar may compromise the covertness of underwater vehicles. Therefore the underwater navigation has become an important military and commercial research issue. The inertial navigation system (INS) is commonly used in the autonomous navigation systems which are a navigation technique in which measurements provided by accelerometers and gyroscopes are used to track the position and orientation of a vehicle by using kinematic equations. Since the error of INS is increased over time then the external source is used to update the information of the INS system. Using the information of the geophysical field maps like topography, geomagnetic, and gravity is one of the external information sources[6–9]. The geophysical field maps are digitally stored in the underwater vehicle and one onboard installed sensor repeatedly measures these fields. Comparing field map features and onboard sensor measurements and combine with INS location information can provide accurate vehicle location[10,11]. In some researches [6,12,13] the navigation system is based on matching the measured positions which are obtained from INS with contours of constant field value of the geophysical maps. In in some cases[14–16] the INS information and the field maps information are combined by Bayes filter like Kalman filter for modifying INS system error. To achieve high accuracy and low error navigation systems the information of two or three geophysical maps are combined[17,18,18,18–21]. In this paper, we use gravity and topography maps. The information of two maps is fused with INS information by a Kalman filter which its measurement equation is defined based on gravity and tertian of the experiment area.

In sec.2 we present a survey of Kalman filter which is the data fusion tool in our method. In sec.3 we consider two maps aided navigation systems based on Kalman filter, and in sec.4 the experimental issue and its simulation results are presented and in the last section, the conclusion is presented.

2. Materials and Methods

In signal processing and estimation applications, we encounter some problems that an unknown parameter has appeared in two equations and the Kalman filter has been applied to estimate that parameter by fusion data which obtains of two equations[22–24]. The first equation which called the state equation is modeling the evolving state of parameter and the second equation which called the measurement equation is modeling the relation between the state of parameter and observation of parameter. In the framework of Kalman filter

assume that state equation and measurement equation are linear and the noise distribution is Gaussian. If the unknown parameter in time step k is x_k, then the state equation can be written as:

$$x_k = F_{k-1} \times x_{k-1} + v_{k-1} \qquad (1)$$

Where

- x_{k-1} is the previous state
- F_{k-1} is the state transition matrix;
- v_{k-1} is the process noise which is assumed to be a zero mean normal multivariate distribution with covariance Q_{k-1}.

The measurement in time step k, z_k of the state x_k is made according to the measurement equation:

$$z_k = H_k \times x_k + w_k \qquad (2)$$

Where

- H_k is the observation matrix
- w_k is the observation noise which is assumed to be a zero mean normal multivariate distribution with covariance R_k.

The Kalman filter is solved in two distinct step: "Prediction" and "Correction" [25]. The prediction step uses the state equation and previous state x_{k-1} to produce an estimation of the state at the current time step, it does not use observation information from the current time step. In the update step, the result of prediction step is combined with current observation information to correct the state estimate. This improved estimate is the output of Kalman filter. If the conditions hold then Kalman filter equation can be written as follow:

Prediction step:

$$\begin{aligned} x_{k|k-1} &= F_{k-1} \times x_{k-1} \\ P_{k|k-1} &= Q_{k-1} + F_{k-1} P_{k-1} F_{k-1}^T \end{aligned} \qquad (3)$$

Correction step:

$$x_k = x_{k|k-1} + K_k (z_k - H_k x_{k|k-1}) \qquad (4)$$

$$P_k = (I - K_k H_K) P_{k|k-1} \qquad (5)$$

Where the K_k is Kalman gain and can be obtained as

$$K_k = P_{k|k-1} H_k (H_k P_{k|k-1} H_k^T + R_k)^{-1} \qquad (6)$$

Two Maps Aided Navigation

Two maps aided navigation method uses the information of two geophysical maps to the improved output of INS navigation system. Information that comes from two geophysical maps and information of the INS navigation system is combined by the Kalman filter. The navigation state vector is defined

$$X = \begin{bmatrix} x \\ y \\ v_x \\ v_y \end{bmatrix} \qquad (7)$$

Where the x and y are coordinates of underwater vehicle, v_x and v_y are velocity of vehicle in directions of this coordinate axes. The INS state vector is denoted by X_k^*, which is include location and velocity of underwater vehicle. The real vector state of underwater vehicle is denoted by X_k. The error vector state δX_k is defined as follow:

$$\delta X_k = X_k - X_k^* = \begin{bmatrix} x - x^* \\ y - y^* \\ v_x - v_x^* \\ v_y - v_y^* \end{bmatrix} = \begin{bmatrix} \delta x \\ \delta y \\ \delta v_x \\ \delta v_y \end{bmatrix} \qquad (8)$$

In fact, δX_k is the INS error in time step k [7,26,27]. in two maps aided navigation system the error vector is considered as the state parameter of the Kalman filter. As discussed earlier for applying the Kalman filter to a problem we need two equations, the state equation, and the measurement equation. By considering the error vector as the state parameter of the Kalman filter it can be shown that state equation can be written:

$$\delta X_k = \begin{bmatrix} 1 & 0 & \tau & 0 \\ 0 & 1 & 0 & \tau \\ 0 & 0 & 1 & 0 \\ 0 & 0 & 0 & 1 \end{bmatrix} \delta X_{k-1} + V_k \qquad (9)$$

Where τ is the duration of the one timestep and v_k is the process noise which is assumed to be a zero-mean Gaussian distribution with covariance Q_k. The state equation can be written as follow:

$$\delta X_k = \Phi(\tau) \delta X_{k-1} + V_k \qquad (10)$$

In the map aided navigation, the measurement of vehicle state is generated by a sensor that installed in the vehicle. The measurement according to the field maps can be gravity, terrain, or geomagnetic. Another measurement of the vehicle state can be generated by referring to the fields map. INS system coordinates of vehicle can be found on the map and its equivalent field amount is the measurement. in map aided navigation when the Kalman filter is applied, the measurement is defined as the difference between the sensor measurement and the map referenced measurement [28,29]. If g_1 and g_1^* denote sensor and map reference measurement for first map and If g_2 and g_2^* denote sensor and map reference measurement for the second

map then measurement equation for the two maps aided navigation can be written:

$$z=\begin{bmatrix}\delta g_1\\ \delta g_2\end{bmatrix}=\begin{bmatrix}g_1-g_1^*\\ g_2-g_2^*\end{bmatrix}=\begin{bmatrix}h_{x1} & h_{y1} & 0 & 0\\ h_{x2} & h_{y2} & 0 & 0\end{bmatrix}\begin{bmatrix}x-x^*\\ y-y^*\\ v_x-v_x^*\\ v_y-v_y^*\end{bmatrix}+W_k \quad (11)$$

Where W_k is the observation noise which is assumed to be a zero mean Gaussian distribution with covariance R_k The surface of the maps are assumed to be plane shape in vicinity of (x^*, y^*) and h_{x1}, h_{y1}, h_{x2} and h_{y2} are slopes of the two planes. Generally the plane equation has the bellow form:

$$f(x,y)=a+h_x(x-x^*)+h_y(y-y^*) \quad (12)$$

Where the h_x and h_y are horizontal and vertical slopes of the plane. Due to the definition of state vector δX_k the measurement equation can be written as follow.

$$z_k=H_k\times\delta X_k+W_k \quad (13)$$

As mentioned in the previous part, Kalman filter is applied for the problems that have two linear equations with Gaussian noise. It is seen that the two maps aided navigation issue has the Kalman filter framework so that can be applied. By using the Kalman filter equations (3)-(6), the navigation problem equation can be obtained.

State and covariance in the prediction step become

$$\delta X_{k|k-1}=\Phi(\tau)\delta X_{k-1} \quad (14)$$

$$P_{k|k-1}=\Phi(\tau)P_{k-1}\Phi^T(\tau)+Q_k \quad (15)$$

State and covariance in the update step become

$$\delta X_k=\delta X_{k|k-1}+K_k\left(g_k-H_k\delta X_{k|k-1}\right) \quad (16)$$

$$P_k=\left(I-H_kK_k\right)P_{k|k-1} \quad (17)$$

Where the g_k is the measurement vector and the K_k is Kalman gain that is given by

$$K_k=P_{k|k-1}H_k^T\left(H_kP_{k|k-1}H_k^T+R_k\right)^{-1} \quad (18)$$

After the error state vector δX_k was estimated in (16), the real state of the underwater can be obtained by

$$X_k=X_k^*+\delta X_k \quad (19)$$

4. Results and Discussion

In order to test the accuracy and performance of the proposed method, experiments with real data were carried out. Field maps are topography and gravity with $1'*1'$ latitude-longitude resolution. The maps as shown in figure (1) have been taken of the Gulf of Oman in the Middle East (red rectangular). In recent years, a lot of research has been done on the environmental characteristics and waters of this region[30–34].

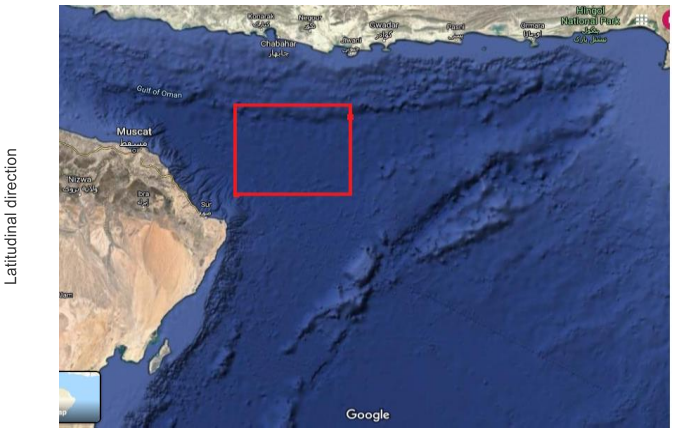

Figure 1. Study area in the Gulf of Oman

The Three-dimensional terrain and gravity maps of the experiment area are shown in figure (2). For the gravity map, we subtracted gravity value by the constant 9.8 and multiplied by 1000.

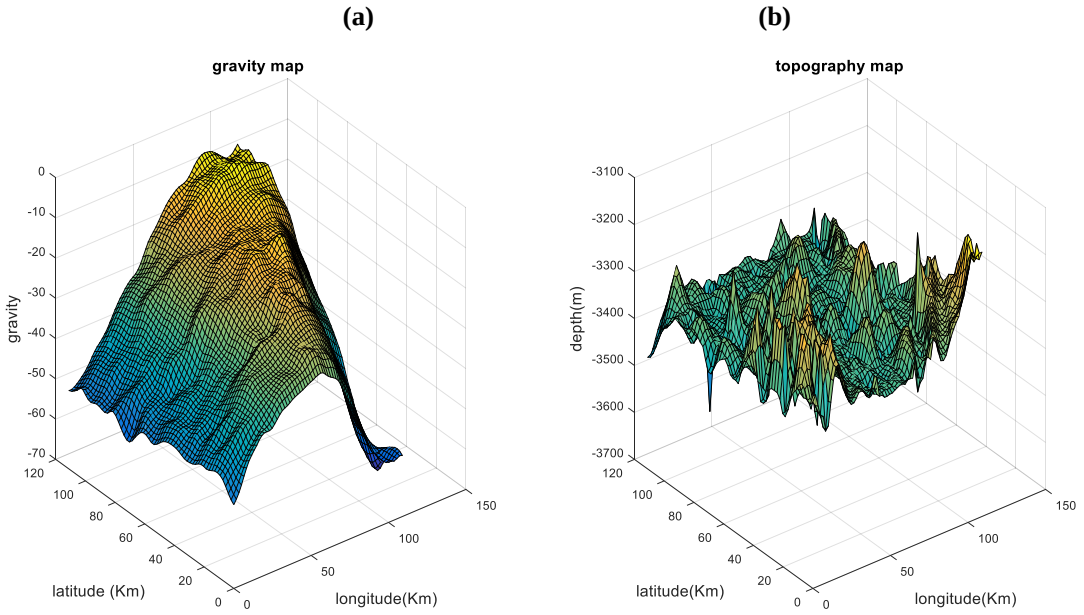

Figure 2. (a): 3-D gravity map, (b): 3-D terrain map of the study area

Suppose a vehicle that was in position (0,0) of the experiment area started its mission. The vehicle travels with a speed of 3 Km/h in the longitudinal direction and 4 Km/h in the latitudinal direction. For noise covariance in the state and measurement equation we have

$$Q_k = \begin{bmatrix} 1 & 0 & 0 & 0 \\ 0 & .1 & 0 & 0 \\ 0 & 0 & 1 & 0 \\ 0 & 0 & 0 & .1 \end{bmatrix}$$

$$R_k = \begin{bmatrix} .2 & 0 \\ 0 & .2 \end{bmatrix}$$

The timestep τ is considered 1 h and so the transition matrix become

$$\Phi(\tau) = \begin{bmatrix} 1 & 0 & 1 & 0 \\ 0 & 1 & 0 & 1 \\ 0 & 0 & 1 & 0 \\ 0 & 0 & 0 & 1 \end{bmatrix}$$

Geophysical maps are a nonlinear function of position and commonly stored as a square grid of field values. Therefore, the observation matrix H_k is obtained by linearization of the maps. As mentioned in sec.3 the field maps must be a plane surface which is a linear expression of filed value and positions. So for calculating the H_k, a plane surface is fitted to a small area in the nearby of the INS navigated position. For example, the small area of the topography map and its equivalent plane surface is shown in the figure (3). the equivalent plane surface is obtained by using linear regression techniques or neural network [35–38].

After obtaining the equivalent linear plane the elements of matrix H_k which are slopes of the equivalent planes can be obtained.

The absolute position error (Km) of these methods is shown in Figure (4). It can be seen from figure (4) that INS position error increase with time and it is shown that the proposed method has the lowest error level, subsequently the INS position errors can be corrected effectively by applying this method. The error of the two other navigation methods the gravity-map aided navigation and topography-map aided navigation is more than error of two maps aided navigation. Filed maps always do not have valid information, for example, the topography map in flat areas doesn't have valid information for the navigation systems, or some paths have the almost same field values so the navigation system may be confused which paths is the real path of the vehicle and navigation systems may not convergence to real position. In the table (1) we do 10000 runs of the navigation methods in this paper. This table shows that two maps aided navigation has the highest valid navigation probability.

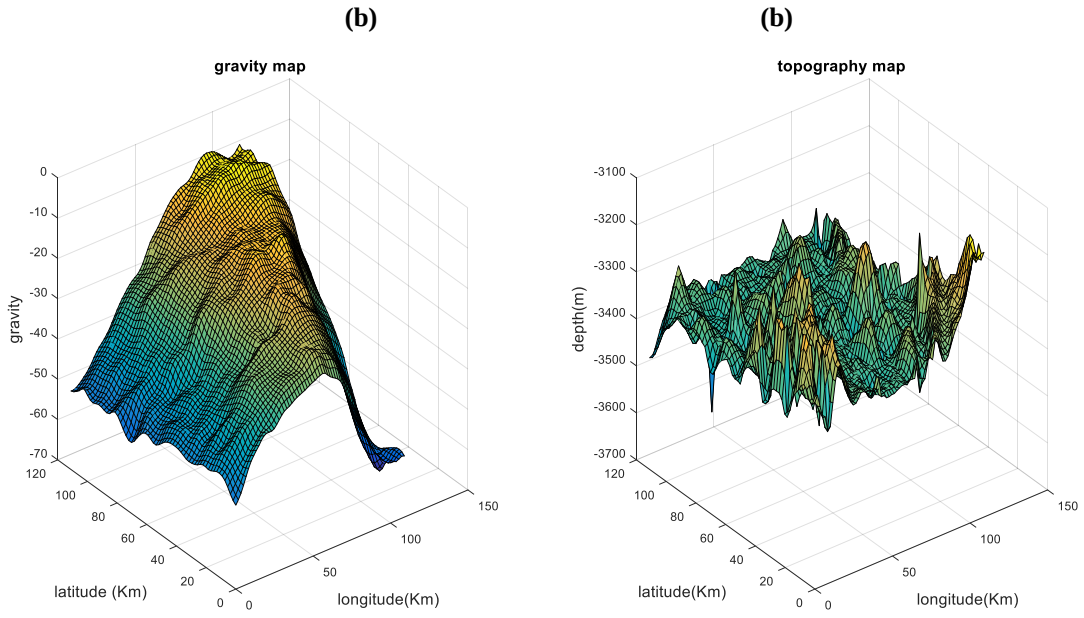

Figure 2. (a): 3-D gravity map, (b): 3-D terrain map of the study area

Table 1. Valid navigation probability or convergence probability

Navigation method	convergence probability
Gravity aided navigation	%79
Terrain aided navigation	%75
Two maps aided navigation	%99.8

5. Conclusions

We presented a method for underwater vehicle navigation by measuring gravity and terrain of the water .the Kalman filter is used to combining information that comes from maps, sensors, and INS. The results show this method has high accuracy more than other methods and have high valid navigation probability. Two maps aided navigation method that presented in this paper does navigation based one filtering stage, unlike the other two maps aided method which uses one Kalman filter for every map and so the valid navigation probability can be decreased.

List of Symbols

K_k	Kalman gain
w_k	observation noise
H_k	observation matrix
v_x and v_y	velocity components of vehicle
v_k	process noise
g_k	measurement vector

6. References

1. Paull, L., S. Saeedi, M. Seto and H. Li, 2013. AUV navigation and localization: A review. IEEE Journal of Oceanic Engineering, 39(1): 131–149.
2. Allotta, B., A. Caiti, R. Costanzi, F. Fanelli, D. Fenucci, E. Meli and A. Ridolfi, 2016. A new AUV navigation system exploiting unscented Kalman filter. Ocean Engineering, 113: 121–132.
3. Mu, X., J. Guo, Y. Song, Q. Sha, J. Jiang, B. He and T. Yan, 2017. Application of modified EKF algorithm in AUV navigation system, In OCEANS 2017-Aberdeen, IEEE, pp: 1–4.
4. Salavasidis, G., A. Munafo, C.A. Harris, S.D. McPhail, E. Rogers and A.B. Phillips, 2018. Towards arctic AUV navigation. IFAC-PapersOnLine, 51(29): 287–292.
5. Franchi, M., A. Ridolfi and M. Pagliai, 2020. A forward-looking SONAR and dynamic model-based AUV navigation strategy: Preliminary validation with FeelHippo AUV. Ocean Engineering, 196: 106770.
6. Kamgar-Parsi, B. and B. Kamgar-Parsi, 1999. Vehicle localization on gravity maps, In Unmanned Ground Vehicle Technology, International Society for Optics and Photonics, pp: 182–191.
7. Wu, L., J. Ma and J. Tian, 2010. A self-adaptive unscented Kalman filtering for underwater gravity aided navigation, In IEEE/ION Position, Location and Navigation Symposium, IEEE, pp: 142–145.
8. Wang, H., L. Wu, H. Chai, H. Hsu and Y. Wang, 2016. Technology of gravity aided inertial

navigation system and its trial in South China Sea. IET Radar, Sonar & Navigation, 10(5): 862–869.
9. Kuang, J., X. Niu, P. Zhang and X. Chen, 2018. Indoor positioning based on pedestrian dead reckoning and magnetic field matching for smartphones. Sensors, 18(12): 4142.
10. Li, M., Y. Liu and L. Xiao, 2014. Performance of the ICCP algorithm for underwater navigation, In 2014 International Conference on Mechatronics and Control (ICMC), IEEE, pp: 361–364.
11. Wang, H., X. Xu and T. Zhang, 2018. Multipath parallel ICCP underwater terrain matching algorithm based on multibeam bathymetric data. IEEE Access, 6: 48708–48715.
12. Bishop, G.C., 2002. Gravitational field maps and navigational errors [unmanned underwater vehicles]. IEEE Journal of Oceanic Engineering, 27(3): 726–737.
13. Zhang, H., L. Yang and M. Li, 2019. Improved ICCP algorithm considering scale error for underwater geomagnetic aided inertial navigation. Mathematical Problems in Engineering, 2019:.
14. Wu, M. and J. Yao, 2015. Adaptive UKF-SLAM based on magnetic gradient inversion method for underwater navigation, In 2015 International Conference on Unmanned Aircraft Systems (ICUAS), IEEE, pp: 839–843.
15. Melo, J. and A. Matos, 2017. Survey on advances on terrain based navigation for autonomous underwater vehicles. Ocean Engineering, 139: 250–264.
16. Bozorg, M., M.S. Bahraini and A.B. Rad, 2019. New Adaptive UKF Algorithm to Improve the Accuracy of SLAM. International Journal of Robotics, Theory and Applications, 5(1): 35–46.
17. Deng, Z., Y. Ge, W. Guan and K. Han, 2010. Underwater map-matching aided inertial navigation system based on multi-geophysical information. Frontiers of Electrical and Electronic Engineering in China, 5(4): 496–500.
18. Zheng, H., H. Wang, L. Wu, H. Chai and Y. Wang, 2013. Simulation research on gravity-geomagnetism combined aided underwater navigation. The Journal of Navigation, 66(1): 83–98.
19. Wang, H., L. Wu, H. Chai, Y. Xiao, H. Hsu and Y. Wang, 2017. Characteristics of marine gravity anomaly reference maps and accuracy analysis of gravity matching-aided navigation. Sensors, 17(8): 1851.
20. Wang, C., B. Wang, Z. Deng and M. Fu, 2020. A Delaunay Triangulation Based Matching Area Selection Algorithm for Underwater Gravity-Aided Inertial Navigation. IEEE/ASME Transactions on Mechatronics.
21. Bao, J., D. Li, X. Qiao and T. Rauschenbach, 2020. Integrated navigation for autonomous underwater vehicles in aquaculture: A review. Information Processing in Agriculture, 7(1): 139–151.
22. Michalski, J., P. Kozierski and J. Ziętkiewicz, 2019. The new approach to hybrid Kalman filtering, based on the changed order of filters for state estimation of dynamical systems. Poznan University of Technology Academic Journals. Electrical Engineering.
23. Cummins, D.P., D.B. Stephenson and P.A. Stott, 2020. A new energy-balance approach to linear filtering for estimating effective radiative forcing from temperature time series. Advances in Statistical Climatology, Meteorology and Oceanography, 6(2): 91–102.
24. Meslem, N. and N. Ramdani, 2020. A new approach to design set-membership state estimators for discrete-time linear systems based on the observability matrix. International Journal of Control, 93(11): 2541–2550.
25. Masnadi-Shirazi, H., A. Masnadi-Shirazi and M.-A. Dastgheib, 2019. A Step by Step Mathematical Derivation and Tutorial on Kalman Filters. ArXiv Preprint ArXiv:1910.03558.
26. Wu, L., H. Wang, H. Chai, H. Hsu and Y. Wang, 2015. Research on the relative positions-constrained pattern matching method for underwater gravity-aided inertial navigation. The Journal of Navigation, 68(5): 937–950.
27. Wei, E., C. Dong, J. Liu, Y. Yang, S. Tang, G. Gong and Z. Deng, 2017. A robust solution of integrated SITAN with TERCOM algorithm: weight-reducing iteration technique for underwater vehicles' gravity-aided inertial navigation system. NAVIGATION, Journal of the Institute of Navigation, 64(1): 111–122.
28. Wu, L., J. Gong, H. Cheng, J. Ma and J. Tian, 2007. New method of underwater passive navigation based on gravity gradient, In MIPPR 2007: Remote Sensing and GIS Data Processing and Applications; and Innovative Multispectral Technology and Applications, International Society for Optics and Photonics, p: 67901V.
29. Wu, L. and J. Tian, 2010. Automated gravity gradient tensor inversion for underwater object detection. Journal of Geophysics and Engineering, 7(4): 410–416.
30. Mashayekhpour, M., R. Emadi and M. Torabi Azad, 2018. Investigation on the Seasonal Variations of Tidal Constituents in the North Coasts of Persian Gulf and Oman Sea. Hydrophysics, 2(2): 67–77.
31. Hosseini hamid, M. and M. Akbarinasab, 2016. The Calculation of the Optimum Index Factor for Monitoring Water Resources pollution using Satellite Images: A Case Study of the Oman sea. Hydrophysics, 2(1): 35–45.
32. ghazi, E., M. Ezam, A. Aliakbari Bidokhti, M. Torabi Azad and E. Hasanzade, 2018. Modeling

Thermohaline Front of the Persian Gulf Outflow in the Oman Sea. Hydrophysics, 4(1): 1–17.
33. yazdanfar, salar, A. Amir Ashtari Larki, mohammad akbarinasab and A. Delbari, 2018. Study of surface fronts in the Oman Sea. Hydrophysics, 4(1): 19–31.
34. rahnemania, abdossamad, A.A. Aliakbari Bidokhti, M. Ezam, K. Lari and S. Ghader, 2019. The Role of Bottom Friction on the Changes of Salinity Front in the Persian Gulf. Hydrophysics, 4(2): 15–25.
35. Lubis, F.F., Y. Rosmansyah and S.H. Supangkat, 2014. Gradient descent and normal equations on cost function minimization for online predictive using linear regression with multiple variables, In 2014 International Conference on ICT For Smart Society (ICISS), IEEE, pp: 202–205.
36. Shanthamallu, U.S., A. Spanias, C. Tepedelenlioglu and M. Stanley, 2017. A brief survey of machine learning methods and their sensor and IoT applications, In 2017 8th International Conference on Information, Intelligence, Systems & Applications (IISA), IEEE, pp: 1–8.
37. Pillai, A.S., G.S. Chandraprasad, A.S. Khwaja and A. Anpalagan, 2019. A service oriented IoT architecture for disaster preparedness and forecasting system. Internet of Things, 100076.
38. Singh, S. and M. St-Hilaire, 2020. Prediction-Based Resource Assignment Scheme to Maximize the Net Profit of Cloud Service Providers. Communications and Network, 12(02): 74.

INTERNATIONAL JOURNAL OF
COASTAL & OFFSHORE ENGINEERING
IJCOE Vol.5/No. 3/Fall 2020 (23-33)

Available online at: www. Ijcoe.org

The effect of Caspian Sea level rise on the environment of the sand dunes of Mazandaran, Iran

Homayoun Khoshravan [1], Tahereh Alinejadtabrizi [2]*, Alireza Naqinezhad [3], Samereh Tirgan[4]

[1] *Water research institute, ministry of Energy; h_khoshravan@yahoo.com*
[2*] *Department of Environmental Engineering, Graduate Faculty of Environment, University of Tehran; n.alinejhad.t@gmail.com*
[3] *Department of Biology, Faculty of Basic Sciences, University of Mazandaran; anaqinezhad@gmail.com*
[4] *Department of Biology, Faculty of Basic Sciences, University of Mazandaran; samereh.tirgan@yahoo.com*

ARTICLE INFO

Article History:
Received: 01 Dec. 2020
Accepted: 24 Jan. 2021

Keywords:
Caspian Sea
sand dunes
fluctuation
erosion
environment

ABSTRACT

Sand dunes are crucial factors related to stability of the coasts, and vegetation plays a decisive role in their creation. In this research paper, analyzing the effects of the Caspian Sea level fluctuations and human intervention on transformation of habitats and biodiversity of coastal plants on sand dunes is assumed as the main goal. The morphological structure of coastal sand dunes and the biodiversity of their plant species were investigated by selecting 11 transects in the eastern coast of the central Mazandaran (Babolsar-Amirabad), also the major changes of the sand dunes in coastal lands were evaluated during the period of the Caspian Sea water level rise, 1978-1995, using the remote sensing. The results showed that coastal dunes in the southern coasts of the Caspian Sea are divided into three groups, intact or healthy, semi-healthy and completely destructed. In total, 174 plant species belonging to 134 genera and 75 families were identified in coastal embankment ecosystems as well as in active, middle and back sand dunes of the coast. The impacts of human intervention (changes in land cover and land use) and some increase in the Caspian Sea level during 1978-1995 were identified as factors affecting the damage of coastal sand dunes.

1. Introduction

Protecting coastal sand dunes is very important especially in integrated coastal zone management (ICZM) programs. As they play a very effective role in stability of coastal areas against erosive forces. loss of these important natural resources, increases sensitivity and severity of coastal vulnerability [1]. Moreover, the rise in the level of sea and ocean water levels, greatly lead to magnify the risk of erosion and flooding of coastal areas. Compatible plants with coastal environments play a very pivotal role in the formation, development and morphological stability of sand dunes [2]. They provide conditions for the formation of small sandy hills through different biological structures, and gradually, they create a small thickness of soil layer on the developed sand dunes and ultimately create specific environmental conditions for continuity of survival and sustainability of other flora species. Generally, the southern shores of the Caspian Sea are sandy in most areas, and sandy hills are extensively visible in some coastal areas. Unfortunately, during 1978-1995, the increase of the Caspian Sea level by 250 centimeters resulted in the destruction of a large part of coastal embankment and sand dunes [3]. Moreover, the development of human activities such as construction of commercial and fishing ports, coastal protection walls, roads and urban improvement over the last few decades, have caused irreparable damages to sand dunes and their biodiversity of flora species [4]. Therefore, in this scientific paper, studying the rate of sand dunes erosion, displacement of the coastline of the Caspian Sea and the ecological response of various habitats of flora species are considered as main problems which are affected by water level fluctuations. In other words, the main aim of the study is investigating changes in coastal complications (ditches and sand dunes) during the period of incensement in the Caspian Sea level, considering human interference and changes in the Caspian Sea level as factors affecting the damage and destruction of coastal land

and its morphological complications. Moreover, environmental impact assessment of flora communities has been conducted in this study. Sandy coastlines occupy only 20% of the total coastline of the world [5]. Sand dunes are usually observed in different regions with dry, semiarid and temperate climatic conditions, but their abundance decreases in tropical areas due to the highly dense vegetation in these areas, the low wind speed and moisture content in sand grains [6]. The sand dunes are affected by some important factors such as the amount of sediment processing, proper vegetation and physical properties of wind, as it can be created and developed gradually on the coastal areas in different forms [7]. Wind is very critical in erosion, while vegetation plays an important role in the stabilization of coastal hills [8]. The density and abundance of vegetation, adapted to the coastal dry environments, create small sandy hills, and gradationally, their morphological structure has been altered and sand dunes have been formed in various forms [9]. The severity of erosion vulnerability of the sand dunes depends on their morphology, climatic conditions and the hydrodynamic of the sea (tide height, wave energy, magnitude and frequency of storm) [10]. Glushko studies in 1996 on the sand dunes of the southern shores of the Caspian Sea have shown that the structure of these sandy hills is very similar to the Sand Barrier, connects to the shore after the fall of the sea level, and is separated from the sea by a wetland. Accordingly, he classified the structure of sand dunes into three groups. The first group is affected by seasonal fluctuations and sea waves. The second group consists of transient sandy hills divided into active and semi-active types. The third group includes well-established sand dunes by vegetation that is far from the beach. Most sandy dunes in the southern part of the Caspian Sea are parabolic and have been developed directly or sinusoidally in the coastal zone [12]. The results of Khoshravan study in 2013, on sand dunes on the southern shores of the Caspian Sea showed that, among total of 856 km of coastline in the southern part of the Caspian Sea, only 156 km of coastline has sand dunes, of which 98 km is located in the eastern part of Babolsar to the end of the central part of the Miankaleh peninsula. Also, the results of this study revealed that 73 km of sand dunes in Mazandaran province suffered from serious erosion. The sandy hills of the southern shores of the Caspian Sea have classified based on the disturbance rate and erosion into healthy (12.1%), semi-healthy (3.4%), leveled (9%) and 75% of them are completely destroyed in other areas. The severity of the damage to the sand dunes on the Amir Abad shore is very high due to port construction and the double impact of the Caspian Sea penetration [4]. The most important types of coastal ecosystems on a global scale are coral hills, sandy hills, mangrove forests, swamps, wetlands, rocky islands, rivers estuaries and sea ice. Comprehensive studies have been carried out around the world, on vegetation sequencing and zonation of coastal ecosystems, especially in Europe [13, 14, 15]. Morphological complications of dry sandy beaches include the coastal embankment, small hills, active sandstones, semi-stabilized and stabilized ones (Fig. 1).

Analysis of biodiversity of plants in coastal areas is one of the important factors for evaluation of environmental conditions [16]. It protects and fertilizes soil, preserves animal species and microorganisms and causes ecological balances through food chain maintenance. At the meantime it also regulates hydrological cycles (reduce runoff, increase groundwater storage), resiss against storms, floods, pests and diseases and preserves the environment through climate adjustment, carbon and nitrogen fixation, soil preservation, photosynthesis and pollutant uptake [17]. In this regard, various studies have been conducted on plant communities in the southern coast of the Caspian Sea. Important studies have been carried out on the ecological characteristics of the southern coast of the Caspian Sea and its different ecosystems have been identified [18]. Naghinezhad et al., (2006), investigated the flora and habitat diversity of vascular plants and mosses by physiognomic methods, in the Boujaq National Park, Iran's first marine-offshore national park. In another study in 2010, Naghinejad and Khoshravan studied biodiversity of plants in six international wetlands, located on the southern coast of the Caspian Sea. Threatened plant species were then examined in the Miankaleh wetland area [20, 21]. In 2007, Khodadadi has studied the habitats and flora of the Astara Steel Wetland. Seighali, (2008) studied floristic of coastal areas up to intermediate heights of Shellman River basin in Langrood city. In the present study, flora species of coastal sand dunes, located in the eastern part of Mazandaran province, in the area of Babolsar to Amirabad port are examined and identified. Meanwhile, the impact of water level fluctuations in the Caspian Sea and human interference is examined on damage of the habitat of the sand dunes.

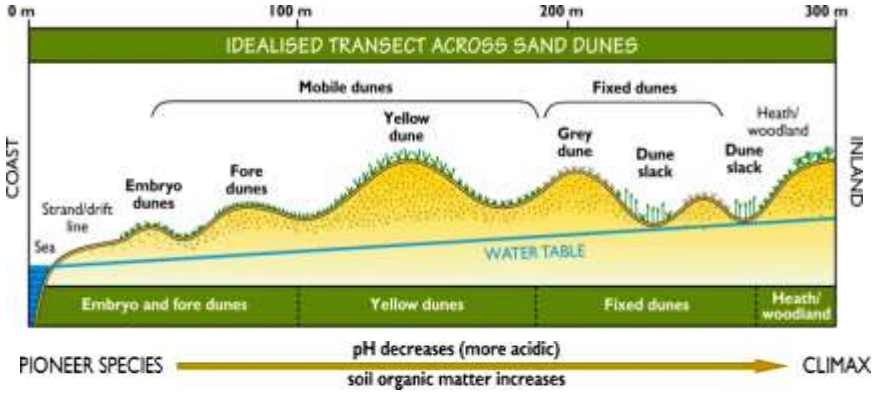

Figure 1. An overview of the sand sequence along the shoreline (www.macaulay.ac.uk)

2. Materials and Methods

The study area is located at the southern coast of the Caspian Sea, between the Neka Power Plant and the eastern margin of Babolsar, with the length of 58 km (Fig. 2). This area includes the coasts of Zaghmarz, Tuskola, Islamabad, Farahabad, Larim, Kohi Kheil, Bahnamir and Bagher Tangeh Villages, from east to west (Fig. 2). This part of the southern coast of the Caspian Sea lies in the morphological zone of east of central Mazandaran [24]. The geometrical structure of the coast in this region consists of a relatively broad coastal embankment and a relatively gentle offshore slope in dry and shallow marine depths. Overlying sediments of the coastal embankment contain fine to medium-grained sand that is relatively well sorted. In some areas of this part of the southern coast of the Caspian Sea, a complete coastal profile, including sand dunes, coastal embankment, coastal area and coastline is characterized. The human occupation in coastal areas has caused some changes in sand cover areas of coasts. Moreover, various agricultural or residential uses, replaced the old coasts. In this part of the Caspian coast, important rivers enter the Caspian Sea, such as Babol Rood, Talar, Larim, Tajan, Teskarud and Nekarud, and their sand load provide conditions for the deposition of sand material in the post-coastal area. The development of sand dunes in the area has been affected by this suitable sedimentary processing in the coastal area.

2.1. Analysis of morphological deformation rate of coastal complications

To study the deformation status of coastlines, coastal embankments and sand dunes over a period of time contemporaneous with some increase in the Caspian Sea water level (1978-1995), aerial photographs of 1983 at 1: 10,000 scale and PAN images of the IRS satellite with a resolution of 5.8 m related to 2004, was used. Initially, referring to 1983 aerial photographs and PAN images of IRS satellite using 1: 25000 topographic maps, the precise geographic location of the Caspian coastlines and morphological features of the coastal dry sections were determined. The information was then stored and updated as distinct digital layers in the Geographic Information System (GIS) environment for temporal and spatial processing. Then, by dividing the study area into 11 polygons measuring 5 × 5 km (Fig. 2), the rate of coastline displacement and the erosion rate of dry section of the coastal area and deformation of sand dunes, under the influence of the Caspian water level fluctuations and human interference were calculated during various periods using comparison and overlap of the information layers created in the software (Arc-GIS 10) environment.

2.2. Identification of plant species and their biological forms

This coastal zone has been chosen for the study of vegetation and biodiversity of existing species, due to the presence of diverse and extended sand dunes. Regarding the existence of suitable biodiversity in different coastal habitats, the study area was selected as a cross-sectional sample to evaluate the impact of the Caspian Sea water level fluctuations and human interference on sand dune vegetation biodiversity. Flora species settled in the coastal embankment, up to the dorsal end of the sand dunes were studied using a total of 78 plots measuring 5 × 5 m in 11 zones (Fig. 2) during spring and summer of 2018. In field operations, the precise geographic location of the 11 transects of study from Babolsar to Amirabad port in Behshahr was coordinated using a GPS device and placed on a digital map in the Geographic Information System (GIS) environment (Fig. 2).

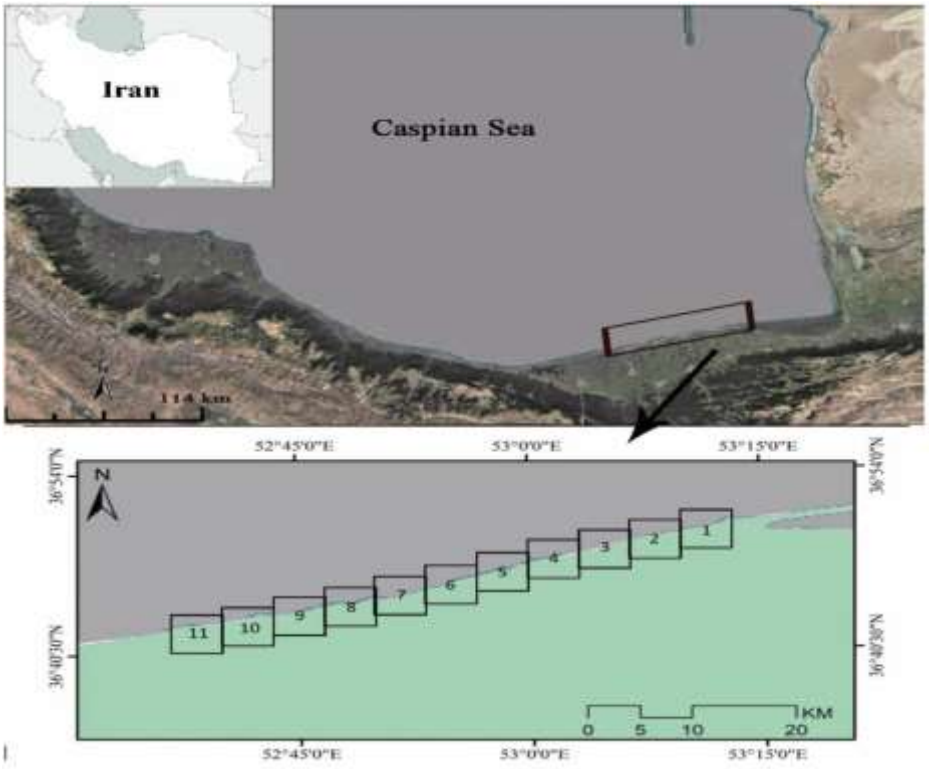

Figure 2. Geographical location of study area and 11 zones, examined in remote sensing studies

Most species were photographed at a collection site for easier identification. Information was collected about the location and date of collection, latitude and longitude, slope, direction of slop and habitat characteristics in each sample plot. After collecting the samples, the plants were scientifically dried, pressed and transferred to the herbarium of Mazandaran University for identification. To identify the plants, scientific sources of Flora Iranica [25], colored flora of Iran [26] were used.

3. Results

3.1. Shoreline displacement, coastal and sand dunes erosion

The results of comparing aerial and satellite imagery from 1983 to 2004 show that shoreline displacement rates have slightly different values in eleven selected zones due to some increase in the Caspian Sea water levels during the above-mentioned period (Table 1). In zone 1 (Neka Power Plant), Positive displacement of shoreline related to active sedimentation process in low depth marine environment, is equal to 200 m in the western part of Nekarud River. However, in the eastern part of power plant pier, seawater infiltration process and coastal erosion have reached a maximum of 120 m water advance in dry part of the shore (Table 1). The extent of the eroded beach is 55056 square meters and the amount of sedimentation area is equal to 293610 square meters. The sand dunes in this zone are completely destroyed and their area is about 424309 square meters (Table 1). The shoreline displacement in zone 2 (Nekarud River) is negligible during the study. The shoreline displacement is slight, even at the mouth of the Neka River. But the Caspian Sea water advancement process is observed gradually to the westward from the Neka power plant, and reaches a peak of 125 m. The eroded coastal land is equal to 294092 square meters. Also, 87 percent of sand dunes have been destroyed (1028649 m^2) (Table 1).

In zone 3 there are two major rivers, Teskarud and Tajan. This zone has the biggest eroded area compared to other zones. Generally, the rate of water progress in this zone is very high. The Caspian Sea has a minimum water progress of about 97m in the eastern margin of the sea, in the Teskarud River estuary, and a maximum of 205 m around the Tajan River estuary. The eroded beach area is 763067m2, and 42% of the sand dunes (417251m^2) have been located in the Farahabad of Sari, Zone 4 shows a nearly integral trend in seawater progression. The maximum rate of the Caspian Sea water progress varies from 110 meters to at least 75m in this zone.

Table 1. Shoreline displacement rate, coastal land erosion and sand dune deformation in the study area in 1983-2004

zone	Shoreline displacement (m)		Eroded Area (m^2)	Area of sedimentation (m^2)	Area of degraded sand dunes (m^2)	Degradation of sand dunes (%)
	Maximum	Minimum				
1	200+	120	55056	293610	424309	100
2	125	125	294092	0	1028649	77
3	205	97	763067	0	417251	42
4	110	75	584484	0	533604	86
5	130	40	454308	237	223079	51
6	125	40	602474	0	105319	13/5
7	120	90	601885	0	106955	8/5
8	125	40	511741	0	128776	8
9	155	80	578840	0	670050	31
10	150	65	520699	0	1609343	72/5
11	215	65	548808	0	648468	58

The eroded beach area is about 584484 square meters and more than 86 percent of the sand dunes in this zone (533604 square meters) have been extinct (Table 1). Zone 5 covers some part of Farahabad and Larim. The water progress in this area is maximum 130m while in the central part reaches 40m. The area of eroded coastal zone is 454308m2. Moreover, 51% of the sand dunes in this zone have been destroyed, equal to 223078m^2 (Table 1). Zone 6 is in the Larim and the Larim River is in this zone too. The trend of shoreline changes and the rate of water progress in this zone have been relatively the same. The water advance in this zone is maximum 125m while it has reached 40m in some parts of the eastern part. The eroded area is 602474m^2, and only 13% of the sand dunes in this zone have been destroyed (Table 1). The area also has broad sand dunes that remain intact, especially in the western part of the Larim River. Zone 7 contains parts of Larim and the area of Kuhi Khil village. The maximum amount of water advance in this zone is about 120m, which is occurred on the eastern and western margins of the zone. In the central part, the progress has been reduced to 90m. The eroded area is equal to 601885 square meters. About 9 percent of the sand dunes are destroyed in this zone. The area of eroded sand dunes is 106955 square meters. As zone 6, widespread sand dunes continue in this zone, with only minor changes just in the coastal face. Zone 8 is located in the areas of Chapakrood, Kohi Khel and Bahnamir villages. Widespread sand dunes are also found in this zone, which remained intact in 2004. The trend of shoreline changes and the rate of water advancement in this zone are mildly reduced from east to west. It reaches 60m in the coastal area, overlooking the Chapakrood mouth. The extent of the eroded area is 511741m2 and 8% of the sand dunes in this zone have been destroyed, with an area of 670050 m2 (Table 1). located in the Bahnamir area, In zone 9 the rate of water advance gradually increases from the east, the estuary of the Chapakrood river, to the west. with the lowest advancement in the eastern side of the zone, equal to 80m and the maximum in the western part, about 155m. There are also wide sand dunes that have been preserved during this period. The eroded coastal area is 578840 square meters. Moreover, 31 percent of the sand dunes with an area of 670050 square meters, have been destroyed (Table 1). Zone 10 is in the area overlooking the Talar River estuary, with a maximum advancement of about 150m in the eastern part and a minimum of 65m in the western part of the zone. In this area, there were relatively wide sand dunes in 1983 that remained somewhat intact during this period in the east of the Talar River; however, they completely disappeared in the western part of the river. The eroded coastal area is 520699m^2 and 72% of the sand dunes of this area, with an area of about 1609343m^2, have been destroyed (Table 1). Zone 11 overlooks the mouth of the Arab Kheil River and part of the east of Babolsar. The progress of water is less in the eastern part of the river and the minimum progress is about 65 meters. In the western part of the zone, the maximum amount of water advance is observed up to 215 meters. The extent of eroded area is 548808 square meters and 58 percent of the sand dunes in this zone, with an area of 648468 square meters, have been demolished (Table 1). A comparison of the quantities of shoreline displacement changes in the study area during 1983–2004, shows that the highest negative shoreline displacement occurred at zone 11, with amount of 215m. The lowest shoreline displacement also occurred in zones 5, 6, 8 of about 40m (Fig. 3). Only in zone 1, a positive displacement of shoreline, equal to 200m has happened during the period of some increase in the Caspian Sea level. The maximum amount of shoreline displacement was estimated to be in zone 1, equal to 320 m, followed by 150m in zone 11. Also, the smallest difference of the shoreline variations was determined to be 30m in zone 7, followed by zone 4 with changes of about 35m (Fig. 3). The maximum eroded coastal land area is 763067m^2 in zone 3, while the lowest is 55056m^2 in zone 1 (Fig. 4). The highest amount of sedimentation occurred in zone 1 is equal to 293610m^2 and the lowest reported in zone 5 is

237m^2 (Fig. 4). The highest extent of sand dunes destruction occurred in zone 10 (1609343m^2) is followed by zone 2 (1028649m^2). Also, the lowest amount of sand dunes destruction occurred in zone 6 (105319m^2) is followed by zone 7 (106955m^2) (Fig. 4).

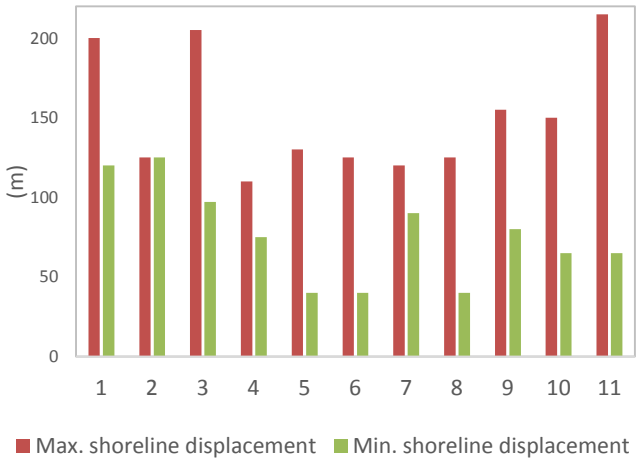

Figure 3. Comparison chart of maximum and minimum shoreline displacement due to increment in the Caspian Sea level in 1983-2004, in studied zones

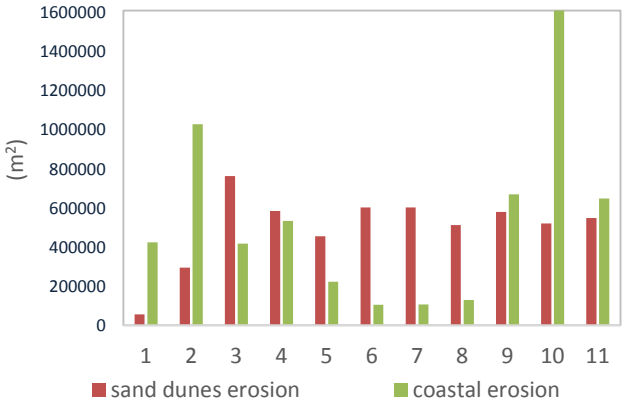

Figure 4. Comparison chart of coastal embankment and sandy dune erosion due to increment in the Caspian Sea level as well as human activities, in 1983-2004, in the studied zones

3.2. Identification of plant species in coastal dunes of the study area

174 plant species belonging to 134 genera and 45 families were identified in this study (Table 2). From these, one species belongs to Pteridophytes and 173 species belong to Angiosperms. Of the 173 species of Angiosperms, 49 belong to the monocotyledones and 124 species belong to the dicotyledones (Table 2). Poaceae strains with 41 species and 34 genera, Asteraceae with 23 species and 18 genera, Fabaceae with 14 species and seven genera and Caryophyllaceae with 10 species and seven genera are more abundant in the flora of the region.

3.3. Survey of the Biological Form and Geographical Distribution of Coastal Plants

Survey the life form spectrum of coastal plants showed that therophytes with 109 species (62.6%) had the most biodiversity in the realm of study. Then, there were hemicryptophytes with 29 species (16.6%), geophytes with 18 species (10.3%) including 15 rhizomatous geophytes and three bulbous (geophytes) plants, phanerophytes with 12 species (6.8%), chamaephytes with four species (2.2%) and helophytes with two species (1.1%) (Fig. 5).

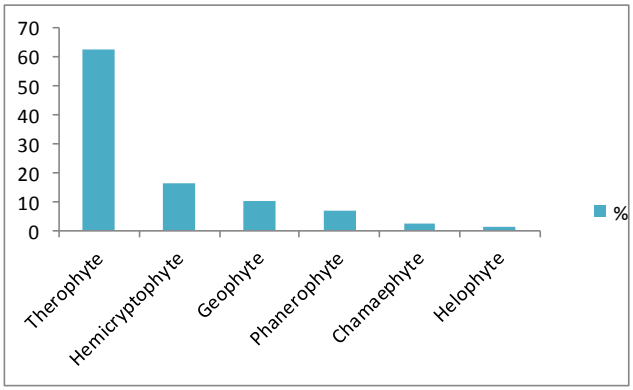

Figure 5. Comparison Percentage of plants in the realm of study

3.4. Introduction of coastal vegetation habitats

Three different vegetation habitats were identified in the study including coastal embankment habitat and primary sand dunes (Foredune), inter dunes habitat and back dune habitat. Each of these habitats contains specific vegetation cover.

3.4.1. Foredune coastal embankment and sand dunes

This coastal habitat is characterized by the presence of pioneer plant species in the coastal embankment

Table 2. Number of genera and plant species belongs to each family

Family	Genus	Species	Family	Genus	species
Equisetaceae	1	1	Meliaceae	1	1
Amaranthaceae	5	8	Moraceae	1	1
Amaryllidaceae	1	2	Onagraceae	1	1
Apiaceae	4	4	Orobanchaceae	1	1
Asparagaceae	1	1	Oxalidaceae	1	1
Asteraceae	18	23	Phytolaccaceae	1	1
Betulaceae	1	1	Plantaginaceae	1	2
Boraginaceae	2	2	Poaceae	34	41
Brassicaceae	7	7	Polygonaceae	2	4
Caprifoliaceae	1	1	Portulacaceae	1	1
Caryophyllaceae	7	10	Primulaceae	1	2
Convolvulaceae	2	4	Resedaceae	1	1
Crassulaceae	1	1	Rhamnaceae	2	2
Cucurbitaceae	1	1	Rosaceae	3	3
Cyperaceae	2	3	Rubiaceae	1	1
Euphorbiaceae	2	5	Scrophulariaceae	2	2
Fabaceae	7	14	Simaroubaceae	1	1
Gentianaceae	1	1	Solanaceae	3	6
Geraniaceae	2	2	Tamaricaceae	1	1
Juncaceae	1	2	Urticaceae	1	1
Lamiaceae	1	1	Verbenaceae	2	2
Lythraceae	1	1	Zygophylaceae	1	1
Malvaceae	2	2			

Figure 6. Indigenous plant species on coastal embankment

associated with extreme conditions on pioneering part of the beach (strandline and embryonic shifting dunes), which are usually small and low-lying. The most important plant species connected to strandline included *Cakile maritima*, *Convolvulus persicus*, *Salsola kali* and *Tournefortia sibirica* (Fig. 6), which are encountered with harsh environmental condition such as high wind velocity, sand movement and salt spray. The following part is embryonic shifting dunes which mainly associated with *Bromus madritensis*, *Bromus tectorum*, *Arundo donax*, *Lolium rigidum*, *Chrozophora tinctoria*, *Corynephorus articulates*, *Cynodon dactylon*, *Paspalum paspaloides*, *Agriophyllum squarrosum*, *Imperata cylindrica* (Fig. 7). The first stage of dune formation mainly related to embryonic shifting dunes.

Figure 7. Abundance of dominant species of Imperata cylindrica in active sand dune habitats

3.4.2. Interdune (Mobile dune)

The most important plant species correlated to sand dunes occurred on inter dunes included *Artemisia tschernieviana*, *Daucus littoralis* subsp. *hyrcanicus*, *Linaria simplex*, *Maresia nana*. The interdune is less environmentally extreme condition with large sand hills. In some areas in this habitat, the soil is well stabilized. In this coastal habitat, there are favorable environmental conditions for the growth of some plants, including *Juncus acutus*, *Phyla nodiflora*, *Equisetum ramosissimum*, *Saccharum ravennae* and *Cyperus rotundus*. The comparison of the abundance for coastal plants biodiversity in mobile dunes shows that *Artemisia tschernieviana* has the highest abundance on sand hill compared to other plant species (Fig. 8).

Figure 8. Presence of Artemisia tschernieviana and Juncus plant species in interdune habitats

Figure 9. Plant species belonging to back dunes

3.4.3. Backdunes habitat

Back sand dunes extend to the inland after the interdunes. It has a more stabilized sandy soil and higher plant species diversity than the previous two habitats. Sand displacement is very low or absent. Backdune is mainly characterized by shrubby plant species such as *Punica granatum* and *Rhamnus pallasii*. The most important plant species identified in this sand habitat included: *Punica granatum*, *Mespilus germanica*, *Prunus divaricata*, *Rhamnus pallasii*, *Paliurus spina-christi*, and *Lonicera floribunda* come from tree species and *Avena sativa*, *Eryngium caucasicum*, *Sedum hispanicum*, *Convolvulus cantabricus*, *Allium rotundum*, *Petrorhagia saxifrage*, *Brassica tournefortii*, *Silene latifolia*, *Tragopogon graminifolius*, *Asparagus officinalis*, *Orobanche nana* and *Vicia tetrasperma* are the herbaceous species which is found only in this zone. This zone, with its distance from the coastline, has the highest richness and biodiversity. Abundance and presence of plant species in the back dune habitat that are the most belong to *Punica granatum*, *Rubus sanctus* and *Rhamnus pallasii*, which are important components of this habitat (Fig.9).

3.5. The intensity of biodiversity and plant habitats destruction

The results of aerial and satellite imagery as well as field observations in 11 zones, have been indicated the intensity of severity of different biodiversity and plant habitats. Also based on the criteria of degradation and erosion, the studied habitats were divided into three groups. The first group consisted of vegetation habitats located in zones 2 and 10 where they have been under high erosion and degradation conditions (Fig. 10). In this group, all plant habitats from the coastal embankment to the end of eroded back dunes section have been eroded and destroyed. Plant habitats located in zones 1, 3, 4 and 11, had moderate degradation properties (Fig. 10). In this group, most of the plant habitats which are located in the coastal embankment and front part of the active sand dunes have been eroded due to infiltration of the Caspian Sea. Plant habitats located on transects 5, 6, 7 and 8, have very low degradation and erosion processes (Fig. 10). In this group all coastal habitats have good

environmental equilibrium conditions without serious damages. Plants that are heavily present in degraded areas and replaced sand dunes include: *Euphorbia maculate*, *Melilotus indicus*, *Oenothera biennis*, *Oxalis corniculata*, *Tribulus terrestris var*. *terrestris*, *Carthamus lanatus*, *Juncus turkestanicus*, *Verbena officinalis* and *Kickxia elatine* subsp. *Crinita*.

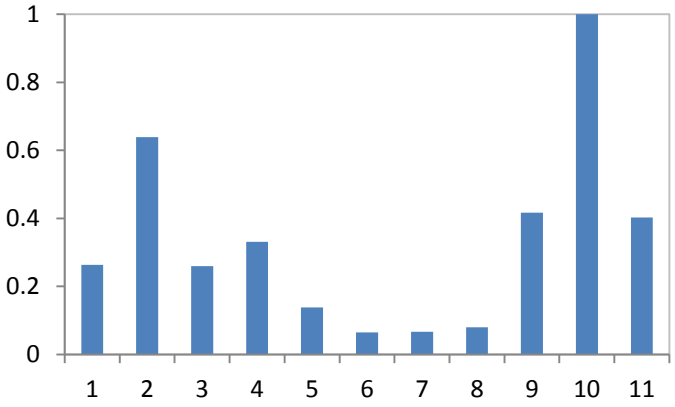

Figure 10. The rate of plant species alternation due to disturbance in 11 studied zones

4. Discussion

Rapid fluctuations in the Caspian Sea level are the most important hydrological characteristics of the area. So the rate of change in the Caspian Sea water level is more than 100 times compared to the oceans [27]. According to the latest reports from the United Nations Economic Program (UNDP), up to $15 billion of damages were imposed on the surrounded coastal states during the last phase of the Caspian Sea water level rise from 1978 to 1995. The last period of the Caspian Sea level rising, equal to 2.5m, from 1978 to 1995, caused degradation and severe coastal lands erosion, as well as environmental consequences, with the destruction of natural land cover, coastal habitats and destruction of coastal ecosystems (Kroonenberg et al., 2000). The dry part of the beach consists of sandy embankment and sand dunes, covered by diverse plant biodiversity. Plants play an important role in the stability of coastal sediments against erosive forces as well as the formation of sand dunes and the development of their morphological structure. Therefore, awareness about the ecological status of coastal areas of the Caspian Sea is of great importance for the organization of coasts and their conservation. As the results of compared aerial photos, satellite images and field observations over the period of 1983 to 2004 shows, morphological behavior of the dry coastal sector in response to increment in the Caspian Sea water levels and human interference, was very different in the 11 studied zones. Pressures of human actions in the eastern area of Babolsar and construction of the Neka power plant in this area, have caused severity in damages to sand dunes and plant ecosystems located on zones 1 and 11. In coastal areas regardless of human interference, located between the Tajan to Teskarud estuaries, the Caspian coastline displacement is the highest due to the mild coastal slope. Rivers and artificial barriers have also played an important role in sedimentary processing in the coastal zone. Therefore, with an increase in the Caspian Sea water level and the intensification of erosional forces, 200 meters of land penetration accurse into the Caspian Sea, in the eastern part of zone 1, overlooking the Neka Power Plant, (Table 1). Thus, despite the negative consequences of human role in morphological disturbance of coastal lands, it has also positive consequences. The extent of damage to coastal lands located in zones 5 to 8, is minimized and these areas have a balanced bio-structure and stable plant ecosystems. However, all the biodiversity of coastal plants in zones 2, 9, 10 and 11 are completely damaged and degraded. These subjects demonstrate the dual role of the impact of rising in the Caspian Sea level and human interference in the destruction of coastal ecosystems. The greatest displacement of the Caspian coastline occurred in zones 1, 3 and 11. These areas have been affected by industrial uses (Neka power plant) and sedimentation of the Tajan and Tskarud rivers and urban development in the coastal sector. The displacement of the Caspian Sea coast line in zones 5, 6 and 8 is much lower compared to other areas, which is strongly related to the geometrical structure of the coasts and their wide embankment. Most of the coastal land erosion occurred in zone 3 and the lowest in zone 1. This confirms the role of anthropogenic and environmental factors in deformation of coastal areas due to the Caspian Sea levels rise. The degradation of vegetation habitats as a result of rising in the Caspian Sea level, as well as the development of different land uses (agricultural, residential and industrial), have caused the loss of biodiversity and deformation of vegetation structure in some parts of the studied zones. In different coastal areas from Babolsar to Neka power plant, the species diversity located in the fore dune habitat is demolished on zones 1, 2, 10 and 11, because of numerous constructions. *Convolvulus persicus* and *Imperata cylindrica* were the most abundant species in this habitat. However, the abundance of *Convolvulus persicus* species has been drastically reduced in the dunes affected by higher degradation. *Saccharum ravennae* is observed in the habitat of fluvial dunes, in zone 9, which is part of the heavily eroded coastlines. Consequently, it can be deduced that if the process of habitat degradation is such that the soil still retains its sandy texture, along with some of the main constituents of the fluvial dunes, other species that are able to grow in sand dunes, can be replaced. It should be noted that if degradation, such as pomale and construction, continues, the soil texture may change in a short period of time, and even primary replacement plants will not be able to grow and invading plants will enter

the degraded habitat. The results of comparing the biodiversity of coastal plants in middle sand dunes show that *Artemisia tschernieviana* has the highest abundance compared to other plant species in this habitat and its distribution is almost uniform in most of the studied areas. In other words, it is not available just in areas where it has faced sever destruction. *Rubus sanctus* has been present in middle sand dunes in the Mirodsar to Karfun area. Its abundance has decreased sharply with increasing degradation of middle sand dunes. *Juncus acutus* has been observed in most of the coastal areas, where the presence of this species is conditioned by an increase in soil moisture and its texture stabilization. Evidence suggests that *Maresia nana* was extinct in transects with high degradation.

Acknowledgment

Authors wish to acknowledge the financial support of the Iran National Science Foundation (INSF) through the research project No. 96003657. Moreover, we greatly thank Ms. Zeinalzadeh who assisted us in editing the paper in advance.

5. References

1- Yılmaz, K.T., Harmancı, D., Ünlükaplan, Y., Alphan, H. and Tezcan, L., (2019), *Impacts of agriculture on coastal dunes and a proposal for adaptation to climate change: the case of the Akyatan Area in the Seyhan Delta*. In Climate Change Impacts on Basin Agro-ecosystems (pp. 165-182). Springer, Cham.

2- Nordstrom K., Psuty N., Carter B.(Eds.), (1990), *Coastal dunes: form and process*, John Wiley and Sons, Ltd., Baffins Lane, Chichester, West Sussex PO19 1UD, England, 392 p.

3- Kroonenberg, S.B., Badyukova, E.N., *Storms, J.E.A., Ignatov, E.I. and Kasimov, N.S., (2000), A full sea-level cycle in 65 years: barrier dynamics along Caspian shores*, Sedimentary Geology, 134(3-4), pp.257-274.

4- Khoshravan, H. and Rouhanizadeh, S., (2011). *The impact of coastal modification and Caspian rapid sea level change on the Amirabad coastal zone*, Ecopersia, (2), pp.81-91.

5- Van Der Maarel, E., (2003), *Some remarks on the functions of European coastal ecosystems*, Phytocoenologia, 33(2-3), pp.187-202.

6- Khoshravan, H., (2000), *Application of biological methods in conservation of coastal areas of southern part of the Caspian Sea*, Report by Ministry of Energy, Iranian Water Resources Management Organization, Caspian Water Resources Research Centre (In Persian).

7- Khoshravan, H., Banihashemi, S. and Shapouri, M., (2013), *Temporal and spatial variation of sand Dunes, the Caspian Sea*, International Journal of Marine Science, 3, pp.173-177.

8- Cam, K., (1972), *Beaches and coasts*, Edward Arnold, London, 570p.

9- Amini, A., Moussavi-Harami, R., Lahijani, H. and Mahboubi, A., (2012), *Sedimentological, geochemical and geomorphological factors in formation of coastal dunes and nebkha fields in Miankaleh coastal barrier system (Southeast of Caspian Sea, North Iran)*, Geosciences Journal, 16(2), p.139-152.

10- Pye, K., Saye, S.E. and Blott, S.J., (2007), *Sand Dune Processes and Management for Flood and Coastal Defence. Part 2*. Sand Dune Processes and Morphology. Joint Defra/Environment Agency Flood and Coastal Erosion Risk Management R & D Programme, R & D Technical report FD1302. TR.

11- Glushko, T., (1996), *Features of landscape structure of the coastal dunes of the East Caspian Sea, Landscape and urban planning*, 34(3-4), pp.183-188.

12- Lancaster, N., (1995), *Geomorphology of desert dunes*. Psychology Press, 290 p.

13- Honrado, J., Vicente, J., Lomba, A., Alves, P., Macedo, J.A., Henriques, R., Granja, H. and Caldas, F.B., (2010), *Fine-scale patterns of vegetation assembly in the monitoring of changes in coastal sand-dune landscapes*, Web Ecology, 10(1), pp.1-14.

14- Drius, M., Jones, L., Marzialetti, F., de Francesco, M.C., Stanisci, A. and Carranza, M.L., (2019), *Not just a sandy beach. The multi-service value of Mediterranean coastal dunes*, Science of the total environment, 668, pp.1139-1155.

15- Cakan, H., YILMAZ, K.T., Alphan, H. and Ünlükaplan, Y., (2011), *The classification and assessment of vegetation for monitoring coastal sand dune succession: the case of Tuzla in Adana, Turkey*. Turkish Journal of Botany, 35(6), pp.697-711.

16- Chytrý, M., (2000), *Formalized approaches to phytosociological* vegetation classification. Preslia, 72(1), pp.1-29.

17- Siadati, S., (2010), *Assessment of variation of floristic composition along the altitudinal gradient of kheyrud forest (50 to 1000 m)*, Master of science thesis, College of Science, University of Tehran, 112 pages (in Persian).

18- Kasymov, A. and Rogers, L., (1996), *Ecological description of the Southern Caspian Sea in the oil-field region of Guneshly*, Polish Ecological Studies, 22(3-4), pp. 83-93.

19- Naghinezhad, A., Saeidi, M.S., Norouzi, M. and Faridi, M., (2006), *Contribution to the vascular and bryophyte flora as well as habitat diversity of the Boujagh National Park*, N. Iran, Rostaniha, 7, pp. 83-105.

20- Naghinejad, A. and Khoshravan, H., (2010), *Plant biodiversity of international RAMSAR wetlands along the coastline of southern Caspian Sea towards a diverse and sustainable situation*, The International

Conference on "Biodiversity of the Aquatic Environment "Towards a diverse and sustainable world". Lattakia, Syria.

21- Naghinejad, A., (2008), *Contribution to threatened vegetation zone of sand dunes in southern Caspian coasts, Iran*, The 1st International Conference on the Caspian Region Environmental Changes, Babolsar, Iran.

22- Khodadadi, S., (2007), *Study of the flora and habitats of the estil wetland (astara)*. Master of science thesis, College of Science, University of Gilan (In Persian).

23- Seighali, N., (2008), *Floristic study of coastal section to intermediate heights of Shalamanrood watershed in Langrood city of Guilan province*, Master of science thesis, College of Science, University of Orumia (In Persian).

24- Khoshravan, H., (2007), Beach sediments, morphodynamics, and risk assessment, Caspian Sea coast, Iran, Quaternary International, 167, pp.35-39.

25- Rechinger, K. H., (ed) (1963-1998), *Flora Iranica, vols.1-178-Graz: Akademische Druck-und Verlasanstalt (1-174)*, Wien: Naturhistorisches Museum, (175-178).

26- Ghahreman, A., (1975-2007), *Colored Flora of Iran, 1-26*, Research institute of forests and rangelands press.

27- Khoshravan, H. and Vafai, B., (2016), *Caspian Sea level fluctuations (past, recent and future)*, Proceeding of 18th International Marine Industries Conference, Kish Island, Persian Gulf, Iran, pp: 71-79 (In Persian).

INTERNATIONAL JOURNAL OF
COASTAL & OFFSHORE ENGINEERING
IJCOE Vol.5/No. 3/Fall 2020 (35-41)

Available online at: www. Ijcoe.org

Positioning Using Classification and Regression: Case study of Oman Sea

Ali Ghorbani[1], Mohammad Reza Khalilabadi [2*]

[1] Department of Computer Science, Shiraz University, Shiraz, Iran;alighorbani29@gmail.com
[2] Assistant Professor, Faculty of Naval Aviation, Malek Ashtar University of Technology, Iran; khalilabadi@mut.ac.ir*

ARTICLE INFO

Article History:
Received: 15 Nov. 2020
Accepted: 26 Jan. 2021

Keywords:
Classification
Regression
Deep Learning
Ensemble Models

ABSTRACT

In the past few years, the location prediction played a critical role in many applications like intelligent self-learning vehicle, ocean location prediction because of the security and speed issues of GPSs. In this study, we proposed a model for location prediction on Oman's gulf using a NetCDF Data set. The proposed model is based on classification and regression which means it first mapped the data in a region on Oman's Gulf using classification and then using regression models to predict a specific location. This progress effect both response time and error of the system. And to the best of our knowledge, no researches are using the same idea. We used multiple classification models for classification tasks (both ensemble models and simple models) and two regression models (linear and XGboost regressor). The result shows reduce of man square error after using classification for regression task. Also, the result and explanation of the data capturing model are provided in the paper.

1. Introduction

The purpose of this study is to design and implement a positioning system at sea using machine learning algorithms based on environmental parameters. The occurrence of an event, tracking of a moving object, or monitoring the physical condition of an area are some of the applications in which the position and coordinates of the agent are very important. Also, in the case of underwater sensor networks, not knowing the location of a sensor causes the data collected by that sensor to be useless. This is especially important in underwater sensor networks, wherein many applications it is necessary to know the location of the nodes. Therefore, in underwater sensor networks as well as ground networks, determining the position of a sensor node is important.

Also, due to the risk of position information leakage of agents using satellite-based positioning systems for physical and strategic factors, the need to design and implement positioning systems without the risk of interception is essential. For example, the following can be mentioned as an example of these risks.

In data collection systems in insecure environments, an attacker may want to prevent the nodes from being positioned accurately and thus prevent the network from working properly. The enemy may compromise with some nodes and thus gain secret keys and other data stored in the nodes. This information can be used to provide misleading information to the base station as well as to other nodes in the network. Without an effective approach to refine or eliminate the effect of incorrect information, the positioning algorithm leads to an incorrect estimate of the sensor position. Therefore, it is necessary to design secure positioning algorithms that are resistant to attacks and obtain the correct position of the node in the presence of intrusion. One of the secure systems is systems based on environmental parameters that find the operating position according to characteristics such as seafloor pattern, water salinity, temperature, etc. In these systems, finding a pattern based on features is necessary for positioning, and considering the results of recent years, deep learning, and artificial networks, as well as cumulative models in finding patterns, classification, and regression, it makes sense to use these methods for this design.

The data used in this design is NetCDF format data, which after preprocessing is converted to CSV format, which is the format used and standard for data engineering and data analysis. The powerful Tensorflow library in the python language was also used to implement this design, as well as the numpy, sickitlearn, pandas, LightGBM, and XGboost libraries.

2. Back Ground

In this section, we provide a summary of the base concepts of our work:

2.1. Classification

Classification models are machine learning models that aim to assign one of the values of the discrete class k to a property called the label with respect to input x. [1] there are many classification models some of them are based on binary classification like SVM and Logistic Regression and some are not like Decision trees and Random forest. Many of these models predict the label by finding a decision boundary in x space which causes to divide the x space to different regions named decision regions. [2] some other algorithms are aimed to first map the data into another space named latent space and then tries to separate the different class labels like deep learning models. [3] Another way to categories of different algorithm models is ensembling. A summary of ensemble models and some of the ensemble models we used in this research have been provided in the next subsection and also a summary of Deep learning in the subsection after that.

2.2. Ensemble models

These models are models that select a set of models and hypotheses and combine their predictions for the final decision. These models are easy to understand and solve for complex problems because they break it down into simpler sub-problems. These models are also more reliable than single models. Figure 1 teaches a basic set learning model, using different training data or different learning algorithms, learn several alternative definitions of a concept. [4]

2.2.1. Random forest

Is an ensemble model for classification and regression and other task using multiple decision trees.[5] The random forest is very similar to the bagging of trees [6] only difference is they use a modified tree learning algorithm that selects, at each candidate split in the learning process, a random subset of the features. This process is sometimes called feature bagging.
Fig 2 shows the difference between decision tree and random forest.

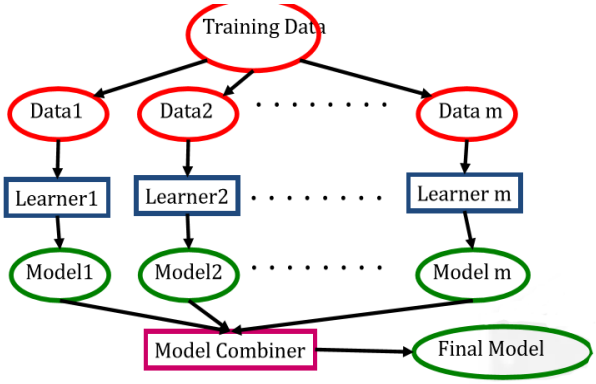

FIGURE 1. A simple ensemble learning algorithm

2.2.2. XGboost

XGBoost is a group algorithm that recently designed distributed slope amplifier libraries that are highly efficient, flexible, and portable in machine learning and Kaggel competitions for optimized structural or tabular data. It implements machine learning algorithms under the Gradient Boosting framework. XGBoost provides parallel tree amplification (also known as GBDT, GBM) that solves many data science problems quickly and accurately. [7]

2.2.3. lightGBM

LightGBM is a gradient boosting framework that uses tree-based learning algorithms. It is designed to be

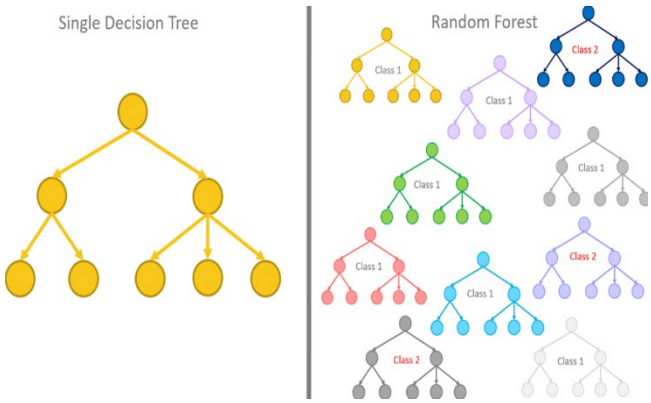

FIGURE 2. Difference between single decision tree and random forest

distributed and efficient with the following advantages: [8]

Faster training speed and higher efficiency.

- Lower memory usage.
- Better accuracy.
- Support for parallel and GPU learning.
- Capable of handling large-scale data.

2.3. Deep Learning

Deep learning is a subcategory of machine learning that tries to find high-level features from input data. [9]

Deep learning is based on the neural network (stochastic models that are directly inspired by the human and animal nervous systems and intend to find a relationship between input and output). Each neural network has two paths, forward and back-ward. In the forward, the input is mapped to the output by passing through a diagram with linear or nonlinear deformation layers, and in the backward, it calculates the cost slope according to the weights and tries to update the weights. In other words, it is based on feature and learning representation in different layers of the model. Deep learning models break down any complex

concept into simpler concepts. This process leads the model to find the basic concepts. In recent years, deep learning has achieved significant success in many areas such as machine vision, machine translation, speech recognition due to access to complex data patterns.

2.4. Regression

The goal of regression is to predict the value of one or more continuous target variables t given the value of a D-dimensional vector x of input variables.

3. Existing Works

Many studies used machine learning models for the natural area.[10] used random forest for Predictions of Seafloor Biomass which is similar to our research in the With a perspective of using ensemble models for prediction a biological metric. As the same perspective li liqi et al..[11] also used the ensemble of SVM with KNN for Eukaryotic Protein Subcellular Location Prediction.

Also, in the perspective location prediction, these models are the hot topic in machine learning and pattern recognition areas like tracking and mobility. Cadger et al. [12] used the machine learning models for location and movement prediction In mobile ad-hoc networks for optimizing the routing protocols. In this work instead of using classification models, they used regression-based machine learning algorithms that can predict coordinates as continuous variables. Stojmenovic et al.[13] proposed a depth-first search (DFS) method for routing decisions in the localized routing area. Chen et al. [14]proposed a model for geographic routing As nodes need to maintain up-to-date positions of their immediate neighbours for making effective forwarding decisions. As these works show, machine learning and artificial intelligence-based models achieved promising results in mobility and network location prediction so it is reasonable to use these models for location prediction on oceans.

4. Data Collection

In this research, we used the Massachusetts Institute of Technology general circulation model (MITgcm). This model solves the completely nonlinear and non-hydrostatic Navier-Stokes equations under the Boussinesq approximation for the inflexible fluid by discretizing the finite space in an orthogonal computational network. The model formulation includes implicit free surface topography and partial step. The MITgcm formulation described in detail by [15]and its source code and documentation are available at the MITgcm group Website [16].

The proportional design selected for this study is a finite third-order direct space-time flux design , [17], which is unconditionally stable.

Turbulent closure parameters for the viscosity and vertical penetration provided by [18] was used in this configuration:

$$\vartheta = \frac{\vartheta_0}{(1+\alpha Ri)^n} + \vartheta_b \quad , \qquad \mathrm{k} = \frac{\vartheta}{(1+\alpha Ri)} + k_b \qquad (1)$$

Where $Ri = \frac{N^2(z)}{(u_z^2+v_z^2)}$ is the Richardson number, $\vartheta_b = 1.5 \times 10^{-4} m^2 s^{-1}$, $k_b = 1 \times 10^{-7} m^2 s^{-1}$, and $\vartheta_0 = 1.5 \times 10^{-2} m^2 s^{-1}$, $\alpha = 5$ and $n = 1$ are adjustable parameters. Horizontal diffusivity coefficient is $k_h = 1 \times 10^{-2} m^2 s^{-1}$, While variable horizontal viscosity uses parameterization of [19]As shown by [20], Using these parameters, the numerical model gives quite solid results even if the wave breaks. This configuration is part of the numerical modeling of internal wave modeling in the Gulf of Oman. The main domain is between $56 - 59^{\circ}E$ and $23.4 - 27.4^{\circ}N$ and was discretized by a non-uniform orthogonal grid of 480*342 points. Spatial resolution along the longitudinal axis, Δx, ranges between 500m (near the sill region) to 1000m, and along the latitudinal axis, Δy, is 1000m. This model has 32 z-levels where the thickness of the layers increases from the surface down. Topographic data were obtained from the National Surveying Center (NCC) of Iran using high-resolution batimetric diagrams. No slipping was imposed on the bottom and side borders.

Average monthly sea surface temperature (SST), sea surface salinity (SSS) of the WOA database and climatic data (wind and heat budget components) database from NOAA [21]. These data prescribed in the model for 12 months of the year. The model range has two open borders on both the west and east sides. Western Open Boundary Conditions Imposed by Hourly Observation Data on Salinity, Temperature, and Flow Profiles from Surface to Bottom Layer at a Distance of 10 m, and Eastern Open Boundary Conditions Imposed by Hourly Observation Data of Sea Surface Height (SSH) predicted data of salinity, temperature, and current profiles. This data is prescribed in the Open Conditions section of the model.To validate the MITgcm model, the monthly average temperature and January salinity profile obtained from the WOD program are compared with the MITgcm simulation results.

Figure 3 shows theses comparison at a point (which situated at 24.7°N and 57.4°E). These plots show a reasonable comparison between WOD and the numerical results.

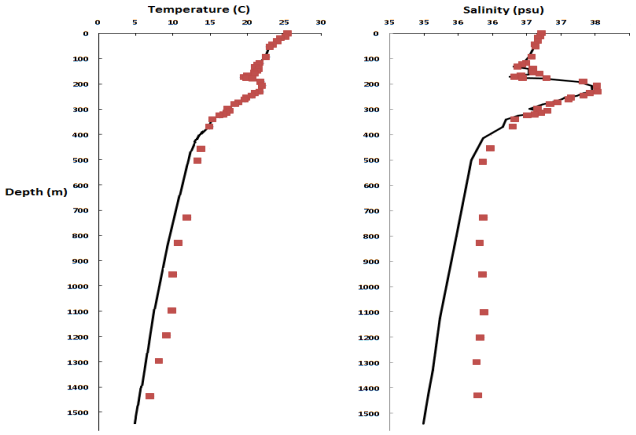

FIGURE 3. A comparison between the monthly averages of temperature and salinity profiles obtained from the WOD program and the numerical results.

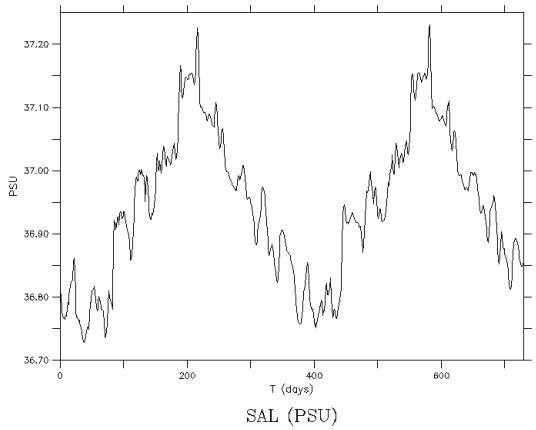

FIGURE 4. Time series of this surface layer salinity site

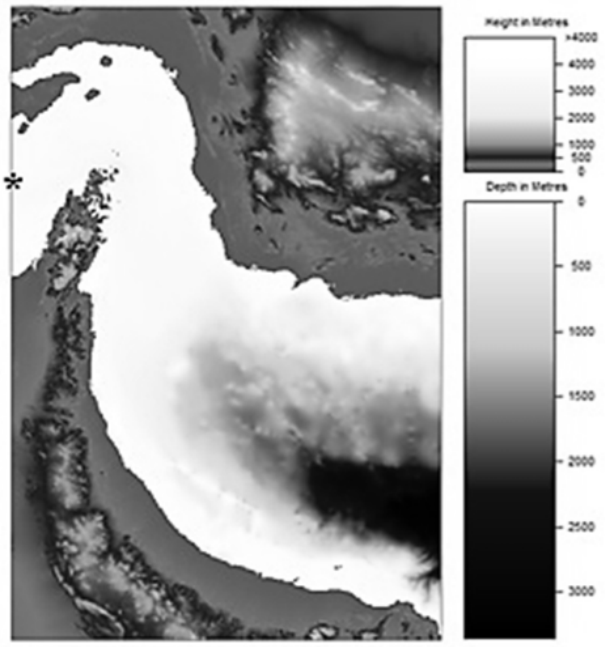

FIGURE 5. Topology of the study area

5. Proposed methodology

In this section, we will describe our model and its benefits in two parts which in part A, the description of our novel model based on classification and regression are provided, and benefits of it compared to the regression model will discuss in part B.

5.1. Region detection using classification and latitude-longitude prediction using Regression

In this research because of the high extent of the area in the Oman's Gulf first, we split the whole area into smaller regions (split latitude into 15 regions and longitude into 10 regions). After that, we assign a new label to data which is the number of the region each data is on it. The classification model job is to train using this new label and in test time predict the region of the data. After that, we train regression models for each region (150 regression models), and in the test time after finding the region of data we used the corresponding regression model to predict the latitude and longitude. We used the ensemble models for classification also Deep learning model result has been provided for comparison and regression we used linear regression, XGboost Regressor, and also Deep learning model for regression. See algorithm 1.

Algorithm 1: coordinate prediction using classification and regression

Input: Data X_train, X_test, latitude X_train, longitude X_train, latitude X_test, longitude X_test
Output: latitude and longitude for X_test
X_train ←Preprocessing(X_train)
X_test ← Preprocessing(X_test)
Region_train ← split latitude into 15 regions and longitude into 10 regions
Clf ← train classification model (input = X_train, label= Region_train)
 	
For i←1 to number of Region_train do
Regressor [i] ← Train Regressor model (input = X_train in Region_train [i])
Region_test ← Clf.predict(X_test)
For i←1 to size X_test do
Latitude[i], longitude[i] ← Regressor[Region_test].predict(X_test[i])

5.2 benefits of the proposed model

the first benefit of our model is the low error because the maximum error of the regression model is the distance of two boundaries of each region. Another benefit of our model compared to simple regression is training and testing speed even with the high number of regressors because these models are much simpler than one regressor they train and test very much faster.

6. Evaluation and result

Our proposed model implemented using GPU-enabled TensorFlow for deep learning models and sklearn library, python XGboost framework, python GPU enabled lightgbm framework. The models are performed on 64-bit Ubuntu 14.04 on PC with Intel(R) Core (TM) i5-6400 CPU at 2.70GHz, 16 GB ram, and NVIDIA GTX 1070 GPU.

6.1. evaluation metrics

To performed our evaluation, we used Accuracy rate (AC) for classification and mean square error (MSE) and mean absolute error for regression.

1. Accuracy rate:
   Percentage of correctly classified records overall records.

$$AC = \frac{number\ of\ correctly\ predicted}{number\ of\ all\ samples} \times 100\% \qquad (2)$$

2. Mean square error (MSE): The average squared difference between the estimated values and the actual value.

$$MSE = \frac{1}{n}\sum_{i=1}^{n}(Y_i - \widehat{Y}_i)^2 \qquad (3)$$

3. Mean absolute error (MAE): The average difference between the estimated values and the actual value.

$$MAE = \frac{1}{n}\sum_{i=1}^{n}(Y_i - \widehat{Y}_i) \qquad (4)$$

6.2. Data pre-processing

6.2.1. Delete Zero samples

In the used dataset there are some samples with zero values for all features with can be happened cause of noise etc. In the first step, we delete these samples to prevent the biasing of models.

6.2.2. Feature selection

The next step of pre-processing is to remove less important or irrelevant features from the dataset to reduce the complexity of the model and also prevent the negative impact of these features on the model. We used the correlation of each feature with labels for feature selection. The QLAT, QSOL, QNLW, NET are the features with minimum correlation with latitude and longitude of data so these features had been removed from the data set.

6.2.3 Normalization

Many features of this data sets consist of a broad range between maximum and minimum, which achieves computational complexity during the learning and testing process. Therefore, we normalized these features using min-max normalization map each feature to range between 0 and one according to equation 5.

$$x_i = \frac{x_i - Min}{Max - min} \qquad (5)$$

Where xi is a data point, min is the minimum value from all data points, and max is the maximum value for each feature.

6.3. Result and comparison

Because the relation between samples would be so different over the year which could hurt the model, we randomly select 10 weeks from the dataset and performed our algorithm. The process not even impact results but also on the complexity of models. For showing these impacts the result using all data also provided. This process means that for predicting the Coordinates in the current week you only need the data for last week.

6.3.1. Classification

In this section, the result of classification (region detection) considering different classification models (Random Forrest, XGboost, Lightgbm, Deep learning model) has been provided. We used 5-fold cross-validation using .7 of data as the training set and .3 data as the test set. As is shown in Table 1 we compared models in terms of the mean of accuracy, training, and

testing time for the randomly chosen 10 weeks and whole data. In the Deep learning model, we used 5 fully connected layers with sigmoid activation function and cross-entropy as loss and Nesterov momentum as the optimizer. As the result shows the XGboost model got the best accuracy rate and the Lightgbm model is the fastest.

Table 1. Training and testing time and accuracy for randomly chosen 10 weeks and full data

Data	Method	Training time	Testing time	Latitude Accuracy	longitude Accuracy
10 weeks	XGboost	1:22:30	3 min	92.97 %	93.41 %
10 weeks	Random Forrest	14 min	1.3 min	95.70 %	96.84 %
10 weeks	Lightgbm	7 min	30 sec	87.93 %	91.48 %
10 weeks	Deep neural net	2:33:22	2 min	64.3 %	68.2 %
Full data	XGboost	3:02:20	5 min	82.69 %	83.48 %
Full data	Random Forrest	1:32:20	4 min	81.22 %	84.26 %
Full data	Lightgbm	42 min	1 min	69.7 %	72.3 %
Full data	Deep neural net	5:33:12	10 min	48.3 %	52.2 %

6.3.2. Regression

In this section the result of regression models has been provided we consider two regression models linear and XGboost regressor which is similar to the XGboost classifier but just with the continuous label as objective. For showing the effect of classification the result of regression only using one regressor (no classification) has been provided in Table 2. As the result shows the classification effect significantly on MSE and MAE and also, we can see it makes the regression problem very simpler because if we use the classification the number of samples and also the area of regressor reduced.

Table 2. Regression result after using classification and without using classification

Using classification	Method	$\sqrt{MSE}$ X	MAE X	$\sqrt{MSE}$ y	MAE y
Yes	Linear	16.70	14.0	12.87	10.87
Yes	XGboost	4.53	2.74	3.55	2.44
Yes	Deep neural net	15.41	11.3	10.3	8.7
No	Linear	162.18	126.02	180.22	150.02
No	XGboost	36.218	20.00	75.02	45.52
No	Deep neural net	150.52	111.22	140.74	127.29

7. CONCLUSION AND FUTURE WORKS

In this research, a novel model for location prediction based on the NetCDF data set on Oman's Gulf has been proposed. This model is based on two tasks a classification and regression. The classification task provides a region labeling for each sample which cause reduces on complexity and error between predicted location and reallocation. For evaluation, we used 5-fold cross using .7 of data for train and .3 for the test. Also, in evaluation, we performed our model on randomly chosen 10 weeks to reduce the complexity of the model but the result on the whole data, also provided. This is the first paper using both classification and regression for positioning. The result shows magnificent improvement in terms of MSE and MAE compared to the scenario of not using classification. Also, the results show that after using the classification the complexity reduced dramatically, which is a great achievement as the model most competes with GPSs. Also, the MSE on regression shows improvement compare to models with no classification. For the feature, we plane to use time-series models for both classification and regression to observe the effect of time on the accuracy, MSE, and MAE.

8. References

1. Bishop, C.M., *Pattern recognition and machine learning*. 2006: springer.
2. Mitchell, T.M., J.G. Carbonell, and R.S. Michalski, *Machine learning: a guide to current research*. Vol. 12. 1986: Springer Science & Business Media.
3. Bishop, C.M., *Neural networks for pattern recognition*. 1995: Oxford university press.
4. Dietterich, T.G. *Ensemble methods in machine learning*. in *International workshop on multiple classifier systems*. 2000. Springer.
5. Ho, T.K. *Random decision forests*. in *Proceedings of 3rd international conference on document analysis and recognition*. 1995. IEEE.
6. Breiman, L., *Bagging predictors.* Machine learning, 1996. 24(2): p. 123-140.
7. *XGBoost Documentation — xgboost 1.3.0-SNAPSHOT documentation.*
8. Ke, G., Q. Meng, and T. Finley, *Welcome to LightGBM's documentation*. LightGBM.
9. Deng, L. and D. Yu, *Deep learning: methods and applications.* Foundations and trends in signal processing, 2014. 7(3–4): p. 197-387.
10. Wei, C.-L., et al., *Global patterns and predictions of seafloor biomass using random forests.* PloS one, 2010. 5(12): p. e15323.
11. Li, L., et al., *An ensemble classifier for eukaryotic protein subcellular location prediction using gene ontology categories and amino acid hydrophobicity.* PLoS One, 2012. 7(1): p. e31057.

12. Cadger, F., et al. *MANET location prediction using machine learning algorithms*. in *International Conference on Wired/Wireless Internet Communications*. 2012. Springer.
13. Stojmenovic, I., M. Russell, and B. Vukojevic. *Depth first search and location based localized routing and QoS routing in wireless networks*. in *Proceedings 2000 International Conference on Parallel Processing*. 2000. IEEE.
14. Chen, Q., S.S. Kanhere, and M. Hassan, *Adaptive position update for geographic routing in mobile ad hoc networks.* IEEE Transactions on Mobile Computing, 2012. 12(3): p. 489-501.
15. Marshall, J., et al., *Hydrostatic, quasi-hydrostatic, and nonhydrostatic ocean modeling.* Journal of Geophysical Research: Oceans, 1997. 102(C3): p. 5733-5752.
16. Adcroft, A., et al. *Overview of the formulation and numerics of the MIT GCM*. in *Proceedings of the ECMWF seminar series on Numerical Methods, Recent developments in numerical methods for atmosphere and ocean modelling*. 2004.
17. Hundsdorfer, W., B. Koren, and J. Verwer, *A positive finite-difference advection scheme.* Journal of computational physics, 1995. 117(1): p. 35-46.
18. Pacanowski, R. and S. Philander, *Parameterization of vertical mixing in numerical models of tropical oceans.* Journal of Physical Oceanography, 1981. 11(11): p. 1443-1451.
19. Leith, C.E., *Diffusion approximation for two-dimensional turbulence.* The Physics of Fluids, 1968. 11(3): p. 671-672.
20. Vlasenko, V., N. Stashchuk, and K. Hutter, *Baroclinic tides: theoretical modeling and observational evidence*. 2005: Cambridge University Press.
21. Boyer, T.P., et al., *World ocean database 2013.* 2013.

INTERNATIONAL JOURNAL OF
COASTAL & OFFSHORE ENGINEERING
IJCOE Vol.5/No. 3/Fall 2020 (43-48)

An analytical and field study on influence of breakwaters on beach morphological evolution: a case study (Astara Port)

Sahar Javansamadi[1], Ali Karami Khaniki*[2], Abbaas Ali Aliakbar Bidokhti[3], Kamran Lari[4], Majid Ghodsi[5]

[1] *Department of Environment, Science and Research Branch, Islamic Azad University, Tehran*
[*2] *Soil Conservation and Watershed Management Research Institute (SCWMRI), Tehran*
Akk7239@yahoo.com
[3] *Institute of Geophysics, University of Tehran, P.O. Box 14155-6466, Tehran*
[4] *Department of Marine Science and Technology, Islamic Azad University, Tehran North Branch, Tehran*
[5]*Department of Environment, Science and Research Branch, Islamic Azad University, Tehran*

ARTICLE INFO

Article History:
Received: 23 Aug. 2020
Accepted: 27 Oct. 2020

Keywords:
Morphological evolution
Modified equilibrium profile Astara Port
Sediment transport
Field measurement

ABSTRACT

Addressing the interaction of the presence of coastal structures, breakwaters for instance, and morphological changes is of great importance. The purpose of this paper is to investigate the influences of the extended breakwaters of Astara Port on sediment transport and beach morphological evolution in the vicinity of them so as to identify how the extension of breakwaters altered the sea bed topography. In order to describe evolving cross-shore profiles in the study area, beach profile surveys were conducted by a single-beam echo sounder. Results showed that the breakwaters considerably affected their surroundings, and scouring in front of them was obvious. Furthermore, comparisons of measured beach profiles with Dean's profile model for the equilibrium beach profile illustrated that the Dean's profile was not able to precisely represent the time- mean profiles. As a result, Dean's equilibrium profile was modified and a new model was developed so that it can represent more correctly cross-shore morphodynamics of the study area. The results revealed that modified equilibrium profile can be a better representative for the cross-shore profiles of the study area.

1.Introduction

Coastal protection engineering works, such as breakwaters, influencing waves, wave-induced nearshore currents, and sediment transport, are carried out so as to protect coasts or harbors against the effects of waves and longshore drift (Tang et al. 2017; Kristensen et al. 2013). The structures can affect bottom topography and the shoreline contour, resulting in overall and local deformations that would not evolve without the presence of them. Overall deformations can cause morphological evolution owing to the disturbance of longshore sediment movement, and the second ones can bring about changes in movements of sediments in the vicinity of the coastal structures during a given storm event (Jackson et al. 2015; Leont'yev 1999; Dolphin et al., 2005). Thus, gaining a deep understanding of changes is of great practical interest and importance (Nam et al. 2011; Leont'yev 1999; Turker and Kabdaşlı 2006).

Numerous investigations have been carried out to evaluate the effects of coastal structures on beach morphologies. Jackson et al. (2015) identified how breakwaters with different layout alter asymmetry of the salient. Basco et al. (1992) investigated beach profile change due to the presence of seawalls installed at Sandbridge so as to protect the land. Based on 14 years of data, they found that the berm lowering rate was marginally larger at seawalled sections in comparison to dune/beach sections. Also, they didn't find any convincing evidence to prove the claim that seawalls had caused higher shoreline recession rates in the study area.However, measuring changes in underlying bathymetry is so expensive that numerous reliable numerical models have been developed to simulate morphological changes. As a result, many numerical studies have been performed to understand the morphological evolution around coastal structures. Since waves, wave-induced nearshore currents have decisive

effects on sediment transport, these studies have placed considerable importance on correctly modelling waves and wave-induced nearshore currents. The results obtained from this approach look encouraging (Broker et al., 1995; Roelvink et al., 1995, Nicholson et al., 1997; Leont'yev, 1999; Zyserman and Johnson, 2002; Johnson, 2004; Saied and Tsanis, 2005; Birben et al., 2007; Du et al., 2010; Ranasinghe et al., 2010; Nam et al. 2011; Tang et al. 2017).Furthermore, an understanding of equilibrium beach profiles may be useful in some problems of coastal engineering (Dean 1991). Using equilibrium beach profiles, which approximately demonstrate the important features of cross-shore profiles a beach, the response of beach profiles under changing hydrodynamic conditions can be shown (Holman et al. 2014; Türker and Kabdaşlı 2006). In addition, this proxy can be particularly used for cases of unknown or poorly known bathymetry and also for evaluation of long-term sediment volume response to sea level rise (Özkan-Haller and Brundidge, 2007, Holman et al. 2014). The best known and most commonly used equilibrium beach profile form is Dean's profile,

2.Study Area

Astara port (38.4069 °N and 48.8815°E) is located at the southwestern section of the Caspian Sea, Iran (Figure 1) The port is bounded to the east by the Caspian Sea, to the north partially by Azerbaijan Republic, to the south by Guilan Province, and to the west by Ardabil Province. In 1996, Astara port was mainly built as a port for fishing, trading, and travelling. After the extinction of Kilka fish, the fishery activities of the port have been stopped. Due to the positive effects the port had on the development of the region, it has been enlarged. As a result, the northern breakwater with a length of 470 m and the southern breakwater with a length of 187 m have been built (Figure 2).

which determines the shape of equilibrium beach profile with regard to the offshore distance and the sediment. The profile does not consider the effects of wave climate, and coastal currents (Dean 1991; Türker and Kabdaşlı 2006; Gonzalez et al. 1999). Several equilibrium beach profiles have been characterized to represent cross-shore profiles subject to different conditions (Dean 1991, Özkan-Haller and Brundidge, 2007, Bodge 1992; Holman et al. 2014).Beach profiles are likely to stay the same under long-term wave climate and persistent sediment size, which means that the sediment transport is equal to zero (Bowen 1980). Bruun (1954) proposed the power law approach, most used form of equilibrium beach profile, but it is commonly known as Dean's profile. It can mathematically define the shape of equilibrium beach profile:

$$h = Ax^{2/3}$$

Where h is water depth, x is seaward distance from the shoreline and A is the sediment-dependent scale parameter (Dean 1991).

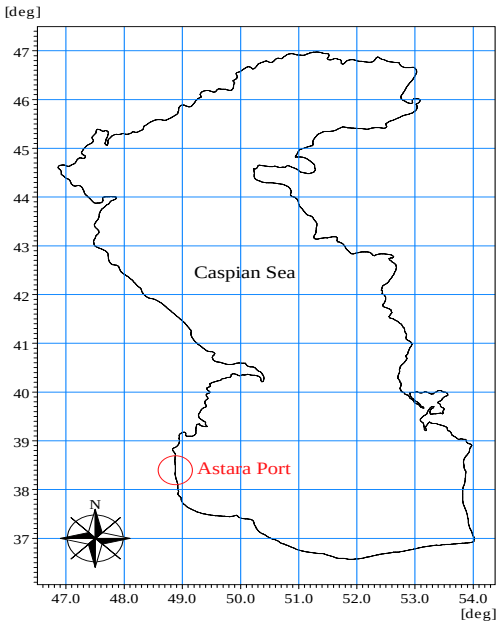

Figure 1. Location of Astara Port

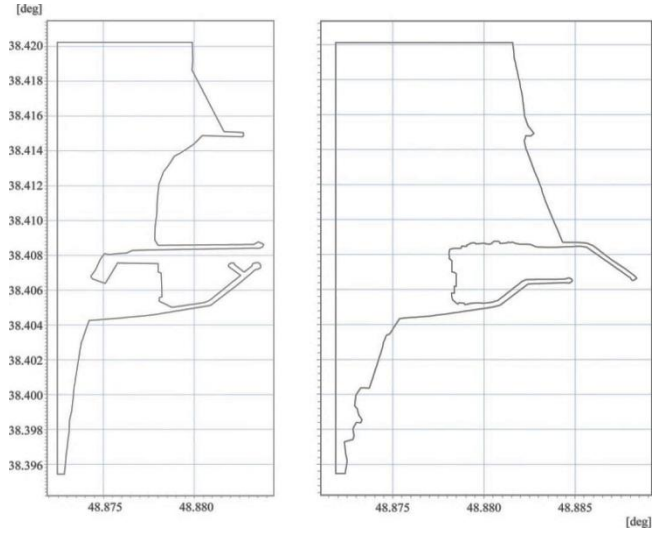

Figure 2. The layout of breakwaters constructed at Astara Port before (left) and after redevelopment (right)

The area under study is exposed to Mediterranean climate with warm summers, moderate and rainy winters. The annual prevailing winds in the area are northerly, northwesterly, and northeasterly. The water level of the port, like that of the Caspian Sea, is currently around 27 m below the level of world oceans. Since there are no tides in the Caspian Sea (Ranjbar and Hadjizadeh 2018; Beni et al. 2013), the tidal water-level fluctuations are negligible in the port. Wave rose for study site shows that the prevailing wave direction is from the north-east. In addition, the dominating current direction is southward (Figure 3).

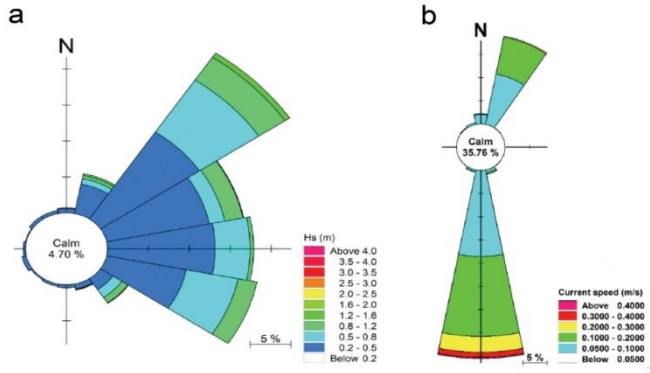

Figure 3. (a) Wave rose and (b) current rose for study site based on observations by Iran's Ports and Maritime Organization

2.1. Scope of present work

One of the objectives of this study was to identify how breakwaters extended in the port of Astara affected the beach topography. Therefore, changes in the bottom topography due to the structures were observed in different years. In addition, this study aimed to modify Dean's equilibrium beach profile model so that it can be a representative model for the study area.

3.Methodology

In this study, morphological evolution in the vicinity of the breakwaters constructed in Astara Port was monitored to investigate the effects of the structures on sediment transport and beach morphological evolution of the study area. After extracting the profiles, monitoring and comparing all the profiles obtained from the collection of topographic data of different years by Plot Composer method from the subsets of Mike Zero module of Mike software, is another step that was done at this stage and the results are graphs obtained from soft processing. Software provided. By analyzing and aggregating them, the sedimentary morphodynamics of the bed profiles in the study area was evaluated. Using Dean (1991) theory and its governing relations, an analytical relationship was presented for the profiles of the study area with the help of Spss and Excel software. Then the profiles extracted from historical and field measured data were compared with the profiles obtained from the analytical relationship (y= 0.02x¾)
, and thus, the degree of concordance of the proposed analytical relationship with the bedside profiles in the study area, Checked out. The results are shown in the form of processing graphs.

3.1. Field Works and Data Base

In order to assess changes in the bottom topography due to the extension of breakwaters of Astara Port, two data sets were used: bathymetric profiles, bathymetric surveys. Using a multi-beam echo sounder, cross-shore bathymetric profiles were surveyed by the Iran National Cartographic Center (INCC) in 2009 and 2011, four of which were extracted to represent the cross-shore profiles of the case study area (Figure 4). The data had a vertical accuracy of ± 5 cm and a horizontal accuracy of 1 m.

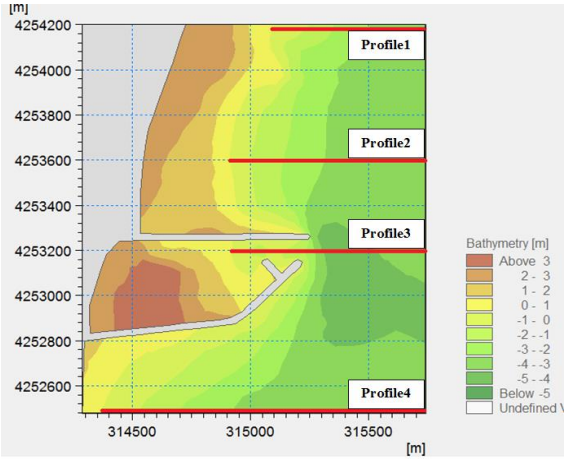

Figure 4. Locations of transects where cross-shore profiles were measured in 2009 and 2011

In 2015, four cross-shore bathymetric profiles were surveyed using a single-beam echo sounder, which had a spatial resolution of 4 m and a vertical resolution of ± 5 cm. The profiles were numbered B, E, G and M. Profile B was sited to the north of Astara Port; profile E was positioned to the upstream side of the port; profile G was located in front of the northern breakwater of Astara Port; profile M was sited to the downstream side of the port (Fig. 5). The profiles are spaced at intervals of approximately 400 m, with an offshore extension of 1400 m.Bathymetric soundings extended to a water depth of 5 m.

Figure 5. Locations of transects where cross-shore profiles were measured in 2015

4.Results

The equilibrium profile described by Dean (1991), $h = Ax^{2/3}$, is mainly based on sediment characteristics, in particular grain size (Karunarathna et al. 2011).(Figure 6) compares cross-shore profiles measured by INCC and Dean's profile corresponding to A=0.02, which was determined based on the sediment characteristics in the study area. It was noticed that there was a considerable difference between the cross-shore profiles and Dean's profile. Therefore, the equilibrium profile described by Dean was modified using SPSS statistics (SPSS Inc) and a new profile, representative for the study area, was proposed. This profile is given by the following:

h=Ax¾

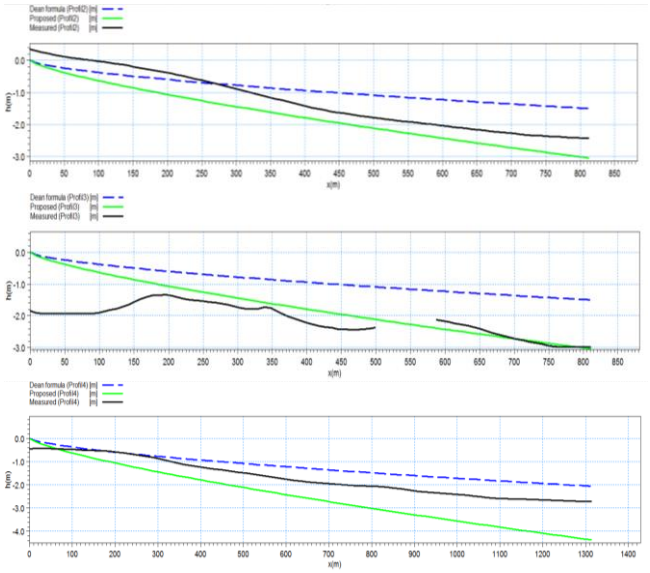

Figure 6. Comparison of cross-shore profiles measured in 2009 and 2011 with Dean's equilibrium profile and proposed equilibrium profile

As can be seen from (Figure 6), cross-shore profiles were better represented by the modified profile than Dean's one. In addition, (Figure 7) shows that there was also a good agreement between the profiles obtained from proposed model and the cross-shore profiles measured in 2015, in particular profiles located far from the breakwaters. As said before, the presence of breakwaters may affect waves, and wave-induced nearshore currents, causing changes in bottom topography, especially in vicinity of the structures. For example, scouring in front of the breakwaters of the port was noted. By investigating how cross-shore profiles changed at near and far distances from the breakwaters, it was also found that profiles sited far from the breakwaters were less affected by the structures and approximately maintained their natural shape. In addition, since the port obstructed the natural sediment longshore transport, accretion on the north side and erosion on the south side of the port were noticeable.

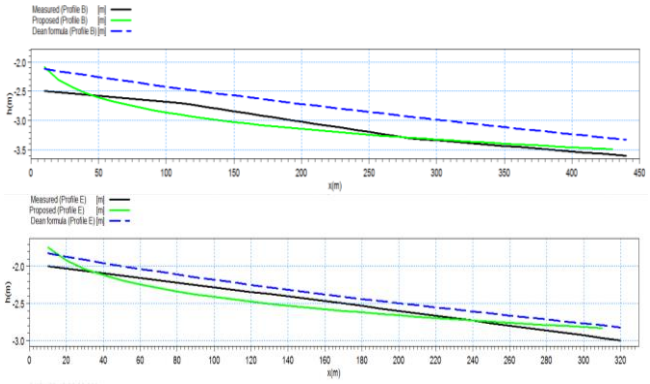

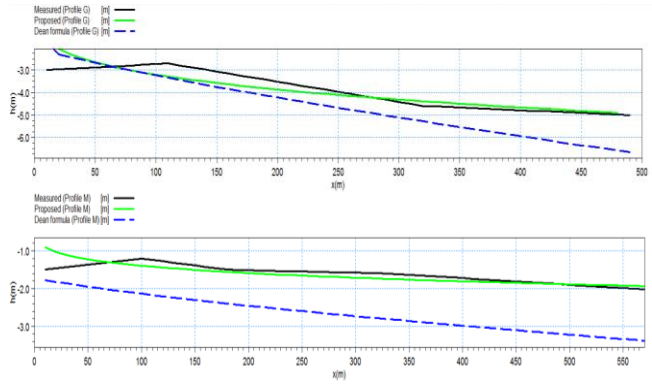

Figure 7. Comparison of cross-shore profiles measured in 2015 with Dean's equilibrium profile and proposed equilibrium profile

5.Conclusion

Coastal protection engineering works may result in changes in characterization of the hydrodynamics and bottom topography of the nearshore domain. Since measuring the changes in underlying bathymetry is very difficult and expensive, developing equilibrium beach profiles which can demonstrate the important features of the bottom topography is of importance. In order to assess the bottom topography of Caspian Sea in vicinity of Astara Port, some field measurements of beach profiles were carried out and some profiles were extracted from hydrographic data observed by Iran National Cartographic Center. The agreement between the profiles and the equilibrium profile described by Dean were investigated, and Dean's profile was modified using SPSS statistics. resulting in a new profile which was shown to be better representative for areas near Astara Port. The proposed equilibrium beach profile was y=0.02x¾. However, there was a good agreement between the cross-shore profiles far from the breakwaters and Dean's profile. This means that Caspian Sea's beach profiles which are not affected by coastal structures behave like those of other coastal waters and open seas. In addition, investigating profiles in vicinity of Astara Port showed that the breakwaters have caused the disturbance to the southward longshore sand transport, leading to beach accretion on the northern side and shoreline erosion in the lee of the structures. Results also showed that waves hitting the breakwaters suspend sediments from the toe of them, and as a results of presence of breakwaters, longshore currents in eastern area of the head of the primary breakwater have enough velocity to move suspended sediments.

In these areas, therefore, more considerable changes were observed in beach profiles. Furthermore, the northern breakwater of Astara Port causes sediments in its lee to deposit, and a lack of sediment within the littoral currents causes severe erosion on the southern coasts of the port.

6.References

1.Basco D.-R, Bellomo D.-A, Pollock C., (1992), *Statistically significant beach profile change with and without the presence of seawalls*, 23rd International Conference on Coastal Engineering, Venice, p. 1924-1937.

2.Beni A, Lahijani H, Harami R, Arpe K, Leroy S, Marriner N, Berberian M, Andrieu-Ponel V, Djamali M, Mahboubi A, Reimer P (2013) *Caspian sea-level changes during the last millennium: historical and geological evidence from the south Caspian Sea*. Clim Past 9:1645–1665

3. Birben, A.R., Özölçer, İ.H., Karasu, S., Kömürcü, M.İ., 2007. *Investigation of the effects of offshore breakwater parameters on sediment accumulation*. Ocean Eng. 34 2, 284–302.

4.Bodge, K.R., 1992.*Representing equilibrium beach profiles with an exponential expression*. J. Coast. Res. 8 (1), 47–55

5.Broker, I., Johnson, H.K., Zyserman, J.A., Ronberg, J.K., Pedersen, C., Deigaard, R., Fredsoe, J., 1995. *Coastal profile and coastal area morphodynamic modelling*. MAST 68-M Final Workshop, Gdansk, pp. 7-12–7-16

6.Bruun, P., 1954. *Coast erosion and the development of beach profiles*: technical memorandum Rep.

7.Bowen, A.J., 1980. *Simple models of nearshore sedimentation; beach profiles and longshore bars*. In: McCann, S.B. (Ed.), The Coastline of Canada. Geological Survey of Canada, pp. 1–11.

8.Dean, R. G. (1991). *Equilibrium beach profiles: characteristics and applications.* Journal of Coastal Research, 7(1), 53-84.

9.Dolphin, T.J., Taylor, J.A., Vincent, C.E., Bacon, J.B., Pan, S., O'Conner, B.A., 2005. *Storm-scale effects of shore-parallel breakwaters on beaches in a tidal setting (LEACOAST)*. Proceedings of the 29th International Conference on Coastal Engineering. 3. ASCE, Lisbon, Portugal, pp. 2849–2861

10.Du, Y., Pan, S., Chen, Y., 2010. *Modelling the effect of wave overtopping on nearshore hydrodynamics and morphodynamics around shore-parallel breakwaters*. Coast. Eng. 57 9, 812–826.

11.Gonzalez, M., Medina, R., Losada, M.A. (1999). *Equilibrium beach profile model for perched beaches*. Coastal Engineering,*36*, 343–357.

12.Holman, R. A., Lalejini, D. M., Edwards, K., & Veeramony, J. (2014). *A parametric model for barred equilibrium beach profiles*. Coastal Engineering,*90*, 85-94.

13.Jackson, N. L., Harley, M. D., Armaroli, C., & Nordstrom, K. F. (2015). *Beach morphologies*

induced by breakwaters with different orientations. Geomorphology,239, 48-57.

14.Johnson, H.K. 2004. *Coastal area morphological modelling in the vicinity of groins*. Proc., 29th International Conf. on Coastal Engineering, ASCE, pp. 2646-2658.

15.Karunarathna, H., Horrillo-Caraballo, J. M.,Spivack, M., & Reeve, D. E. (2011). *Analysis of key parameters in a diffusion type beach profile evolution model*. Continental Shelf Research,31(2), 98-107.

16.Kristensen, S. E., Drønen, N., Deigaard, R., & Fredsoe, J. (2013). *Hybrid morphological modelling of shoreline response to a detached breakwater*. Coastal Engineering,71, 13-27.

17.Leontyev, I. (1999). *Modelling of morphological changes due to coastal structures*. Coastal Engineering,38(3), 143-166.

18.Nam, P. T., Larson, M., Hanson, H., & Hoan, L. X. (2011). *A numerical model of beach morphological evolution due to waves and currents in the vicinity of coastal structures*. Coastal Engineering,58(9), 863-876.

19.Nicholson, J., Broker, I., Roelvink, J.A., Price, D., Tanguy, J.M., and Moreno, L. 1997. *Intercomparison of coastal area morphodynamic models*. Coastal Engineering 31, 97-123.

20.Özkan-Haller, H. T., & Brundidge, S. (2007). *Equilibrium Beach Profile Concept for Delaware Beaches*. Journal of Waterway, Port, Coastal, and Ocean Engineering,133(2), 147-160.

21.Ranasinghe, R., Larson, M., Savioli, J., 2010. *Shoreline response to a single shoreparallel submerged breakwater*.Coast. Eng. 57 (11), 1006–1017.

22.Ranjbar, M.H. & Hadjizadeh Zaker, N. Ocean Dynamics (2018) 68: 35.

23.Roelvink, J.A., Reniers, A.J.H.M., Walstra, D.J.R., 1995. *Medium-term morphodynamic modelling*. MAST 68-M Final Workshop, Gdansk, pp. 7-3–7-6.

24.Saied, U.M., and Tsanis, I.K. 2005. ICEM: *Integrated Coastal Engineering Model*. Journal of Coastal Research 21(6), 1275-1268.

25.Tang, J., Lyu, Y., Shen, Y., Zhang, M., & Su, M. (2017). *Numerical study on influences of breakwater layout on coastal waves, wave-induced currents, sediment transport and beach morphological evolution*. Ocean Engineering,141, 375-387.

26.Turker, U., & Kabdaşlı, M. (2006). *The effects of sediment characteristics and wave height on shape-parameter for representing equilibrium beach profiles*. Ocean Engineering,33(2), 281-291.

27.Zyserman, J.A., and Johnson, H.K. 2002. *Modelling morphological processes in the vicinity of shoreparallel breakwaters*. Coastal Engineering 45, 261-284.

INTERNATIONAL JOURNAL OF
COASTAL & OFFSHORE ENGINEERING IJCOE Vol.5/No. 3/Fall 2020 (49-56)

Available online at: www. Ijcoe.org

A Parametric Study of Critical Buckling Force in Snaked Lay Pipelines under HP/HT Condition

Yasaman Rezaie[1], Seyed Mohammad Hossein Sharifi[2*], Gholam Reza Rashed[3], Farzad Numani[4]

[1] *Master Student of Mechanical Engineering, Petroleum University of Technology; yasaman.rezaie@afp.put.ac.ir*
[2*] *Assistant Professor of Mechanical Engineering Department, Petroleum University of Technology; sharifi@put.ac.ir*
[3] *Asociated Professor of Mechanical Engineering Department, Petroleum University of Technology; g.rashed@put.ac.ir*
[4] *Head of Plant Inspection, Iranian Offshore Oil Company; Fnumani@iooc.co.ir*

ARTICLE INFO

Article History:
Received: 16 Mar. 2020
Accepted: 20 Feb. 2021

Keywords:
Offshore Pipeline
Snake Lay Configuration
Lateral Buckling
Critical Buckling Force
High Pressure/ High Temperature

ABSTRACT

Pipelines are an economical way for offshore oil and gas transportation. In operation conditions, flowing high pressure/high temperature (HP/HT) fluids may induce axial expansion. If this expansion is constrained, axial stresses will be created and they may cause pipeline buckling. In order to reduce damages and avoid buckling in unpredictable places, the controlled buckling concept is introduced. To use this concept in the present study, buckling is triggered at some predetermined locations by using the snaked laying method. This paper analyzes the global buckling process of a pipeline by using numerical simulation methods and the effects of loading (internal pressure and temperature) and section properties (diameter and thickness) are investigated on the critical buckling force of snaked lay pipelines under HP/HT conditions. Then, the analysis results of the finite element method (FEM) are compared with analytical solutions and previous simulation methods. This work includes performing nonlinear finite element analysis and modeling pipe-soil interaction of as-laid pipelines by the use of spring elements. The results show that the use of equivalent temperature instead of pressure difference, as already applied in previous studies, is not an authentic method and cannot introduce an accurate outcome. The analysis shows that by increasing pressure and decreasing temperature, the critical buckling force is decreased and the pipeline buckling occurs sooner. The investigation of section properties indicates that the most effective parameter is thickness. It is remarkable to know that at low values of thickness, the effect of diameter is negligible and by increasing thickness, the influence of diameter is increased. Comparing the analytical and numerical results reveals that at low values of circumferential stiffness (ratio of diameter to thickness), there are minor differences between numerical and analytical results.

1. Introduction

Submarine pipelines are one of the most efficient devices for oil and gas transportation. In operational conditions, the pipelines are subjected to high pressure/ high temperature (HP/HT) fluids to ensure the smooth flowing of oil [1]. The HP/HT conditions of hydrocarbon contents in pipelines establish longitudinal expansions. This expansion is limited by the pipe-soil interaction and end connections of the pipeline, resulting in compression forces [2]. Buckling occurs when the effective axial compressive force is increased to a critical load beyond which the pipeline becomes unstable and deforms to reduce compressive load and take a lower energy state. The buckling activation can damage the pipeline integrity and have unfavorable results [3].

There are two different methods to prevent inappropriate effects of lateral buckling: (a) totally constrained method, and (b) controlled lateral buckling concept. In the former method, the pipeline configuration is restricted and the pipeline movements are stopped in any direction, which is possible by trenching, burying and rock dumping, but these solutions are not economical. In contrast, the latter method, which is suggested to work with pipeline rather than operating against it, is much more cost-

effective. To be more specific, lateral buckling is triggered at a number of controlled buckle locations to prevent severe buckles occurring at a few random sites [4]. Some of the methods used in practice to control the number of buckles are terrain irregularities, vertical triggers, and snake lay which are described in more detail in [4]. The snake laying method is the most economical compared to the other suggested means. The main difference between this method and the vertical trigger is that there are no resulting spans and consequently no vortex-induced vibrations (VIV) or trawl hooking loads [2]. To understand the benefits of the snake laying method, Li et al. [5], Liu et al. [6], and Jiang Gung et al. [7] have compared various studies to reveal the advantages of this technique.

There are some successful projects, e.g. the Penguins project [8] and the Echo Yodel project [9], in which the snaked laying method has been used in practice. Preston et al. [10] presented a summary of accepted methodology and performed some analyses to specify an acceptable as-laid pipeline geometry. Rundsag et al. [4] and Rathbone et al. [11] implemented a parametric study to investigate the effect of snake lay geometry on the buckle initiation force, resulting bending moment, and strain by the finite element (FE) software ABAQUS. The investigated parameters included lay radius, arc length, and offset angle. Cumming and Rathbone [12] studied the relationship between the minimum buckle initiation force and the horizontal offset angle of a pipeline, considering an Euler buckling approach. In the end, a relationship is proposed that estimates the buckle initiation force based on pipeline stiffness and weight, offset angle, and friction factor which is then compared against idealized finite element models. Obele Ifena [13] studied the influence of pipe-soil interaction on the design of surface laid subsea pipelines susceptible to lateral buckling. Liu et al. [14] suggested a new configuration for curved section of snaked laying method. It is recommended to use a sinusoidal configuration instead of circular sections which can reduce the buckle initiation force. Wang et al. [2] proposed a new shape of snaked laying curve based on a combination of genetic algorithm (GA) and finite element analysis.

There are some basic analytical methods introduced many years ago. In 1984, Hobbs [15] suggested four models for lateral global buckling and obtained an analytical solution for buckling force, buckling length, and buckling deformation amplitude. In another study, Taylor and Gan [16] researched pipelines with imperfections and obtained analytical solutions which include the first and second order for a buckling model. All the studies mentioned above have addressed pipelines that experienced high temperatures, but they have overlooked the effect of external and internal pressures. More specifically, the effect of the pressure difference has been converted into an equivalent temperature difference, as explained in more detail in [17] and [18]. Besides, most parametric studies have focused on the snake laying geometry and the effect of the pipeline section has not been investigated.

The present study focuses on the assessment of critical buckling force F_{cr} (or the buckle initiator force) by considering the effects of the hydrostatic pressure and internal pressure of fluid contents. In the next step, the effects of external diameter and thickness are analyzed to establish how variations in pipeline section properties will influence the buckle initiation force.

2. Finite Element Modeling

The finite element method presents an appropriate way to assess the lateral buckling of pipelines. The finite element model of a subsea pipeline is described in detail on the basis of four aspects.

2.1. Configuration of Snaked Lay Pipelines

A typical configuration of snaked-lay pipelines composed of a straight section and a curved section is shown in Figure 1. The straight section is usually longer than the curve one and it can be described by L, V and β called laying wavelength, amplitude curvature, and laying chord length, respectively. In this figure, “ab”, “de”, “ef”, and “hi” are examples of the straight section. The configuration of a typical arc curve section is described in more detail in which the lay radius R and the offset angle θ control the shape of the curve section. Examples of the curved section include “bcd” and “fgh”. It is significant to know that the relationship between the lay radius, offset angle, and laying chord length can be expressed by Eq. (1):

$$\beta = R \times \theta \tag{1}$$

In this study, just three parameters, i.e. V, R, and θ, are used for simulation and these are equal to 26.25 m, 287.5 m, and 5.38. The purpose of choosing these values is to be ensuring that the third mode of buckling will happen. More detail about this mode are provided in the next sections. Because of symmetric loading and geometry, just a quarter of pipeline length is simulated in Figure 1, i.e. “cde”.

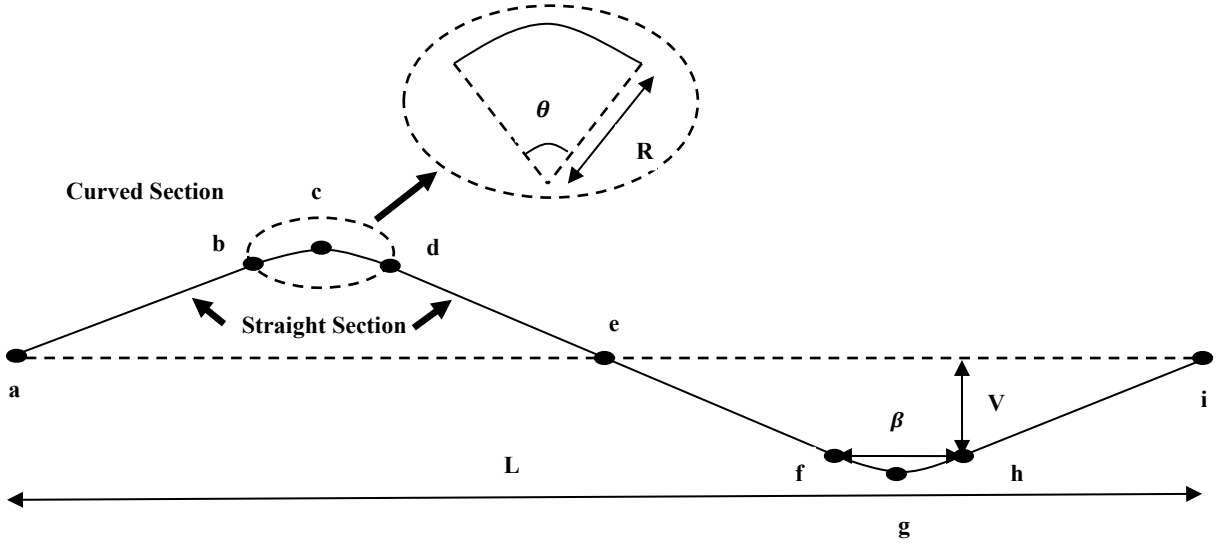

Figure 1. The snake lay configuration

2.2. Pipeline Properties

The inputs for material properties include basic data such as Young's modulus, Poisson's ratio, thermal expansion coefficient, and yield strength, which are listed in Table 1. The carbon steel material used for the pipe is API 5L grade X65.

Table 1. The material properties of pipeline [19]

Characteristic	Value
Elasticity modulus (E_{steel})	2.07×10^{11} $[N\ m^{-2}]$
Poisson's ratio (ν)	0.3 [-]
Thermal expansion coefficient (α)	1.1×10^{-5} $[℃^{-1}]$
Yield stress	545 $[MPa]$
Density (ρ)	**7850** $[\frac{Kg}{m^3}]$

The isotropic power law is adopted to describe the pipeline material behavior as expressed in more detail by Eq. (2):

$$\sigma = \begin{cases} E\varepsilon & \varepsilon \le \varepsilon_y \\ \sigma_0 (\frac{\varepsilon}{\varepsilon_y})^n & \varepsilon > \varepsilon_y \end{cases} \quad (2)$$

where σ_0 is the yield stress, n is the strain hardening assumed to be 0.05, and ε_y is the yield strain, which is equal to 0.00263. 3D-finite element simulations were performed using the ABAQUS standard code [20]. The pipe was modeled using eight-node 3D elements (C3D8R).

2.3. Pipe-Soil Interaction

In this research, submerged weight is considered. The presence of this loading introduces self-weight on each element of the pipeline and consequently creates an interaction between pipeline and soil. The simulation of this contact can be performed by using SPRING1 elements in order to consider axial, lateral and normal interactions as shown in Figure 2.

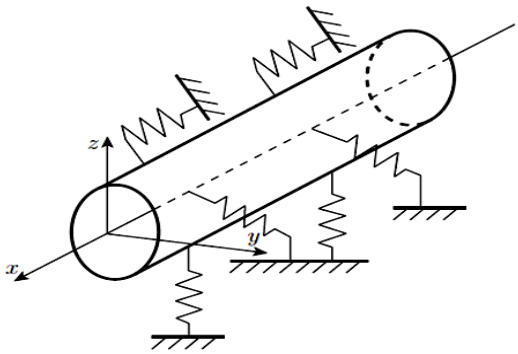

Figure 2. The pipe-soil interaction model by using SPRING elements [14]

SPRING1 is placed between the seabed and outer pipe nodes and acts in a fixed determined direction. Bi-linear and tri-linear resistance models are selected for axial and lateral pipe-soil interactions, respectively. For normal interaction, it is assumed that the spring has high values of stiffness in order to prevent the motion of the pipeline in this direction. The basic parameters for the description of resistance models are listed in Table 2.

Table 2. The basic parameters for the pipe-soil interaction [11]

Characteristic	Value
Axial break out displacement	10 $[mm]$
Axial friction coefficient	0.6 [-]
Lateral break out displacement	140 $[mm]$
Peak lateral friction coefficient	1.1 [-]
Residual lateral displacement	990 $[\boldsymbol{mm}]$
Residual lateral friction coefficient	0.6 [-]

2.4. Pipeline Loading

A 3D model is used to simulate the pipeline global buckling behavior. Disregarding the wave-current load and residual lay tension associated with the installation, five main forces act on a pipeline including hydrostatic pressure, the submerged weight of the pipeline, internal pressure, soil resistance, and temperature load [1]. The loading and boundary conditions of a part of the pipeline are shown in Figure 3.

3. Analytical Solution for Snake Laid Pipelines

Rathbone et al. [11] proposed a formula for calculating the critical buckling force, F_{cr}, of a curved pipeline with lay radius, R. To derive this equation, it is assumed that the pipeline deflection happens when the axial compression force exceeds the lateral soil resistance.
The relationship between critical buckling force, lateral resistance, and lay radius can be expressed as:

$$F_{cr} = \mu . W_{sub} . R \qquad (3)$$

where W_{sub} and μ are the submerged weight and lateral friction factor, respectively.

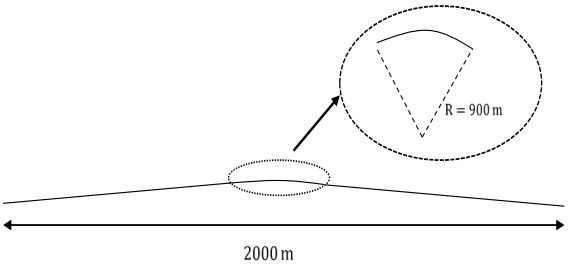

Figure 4. The geometric shape of pipeline

The axial compressive force of the pipelines with $\theta = 4°$ and $\theta = 2°$ are calculated in this section. It is important to know that the main difference between the present study and Rathbone et al. [11] is that the work introduced here is done in a 3D environment whereas Rathbone et al.'s study in a 2D environment.
Figure 5 shows the relationship between the axial compressive force and the value of displacement in the midpoint of the pipeline. The peak point of the curve shows the value of the buckle initiation force. Before this point, the pre-buckling stage happens and it can be seen that the axial compressive force increases with small variations in displacement. After the compressive force touches the peak point, the post

4.

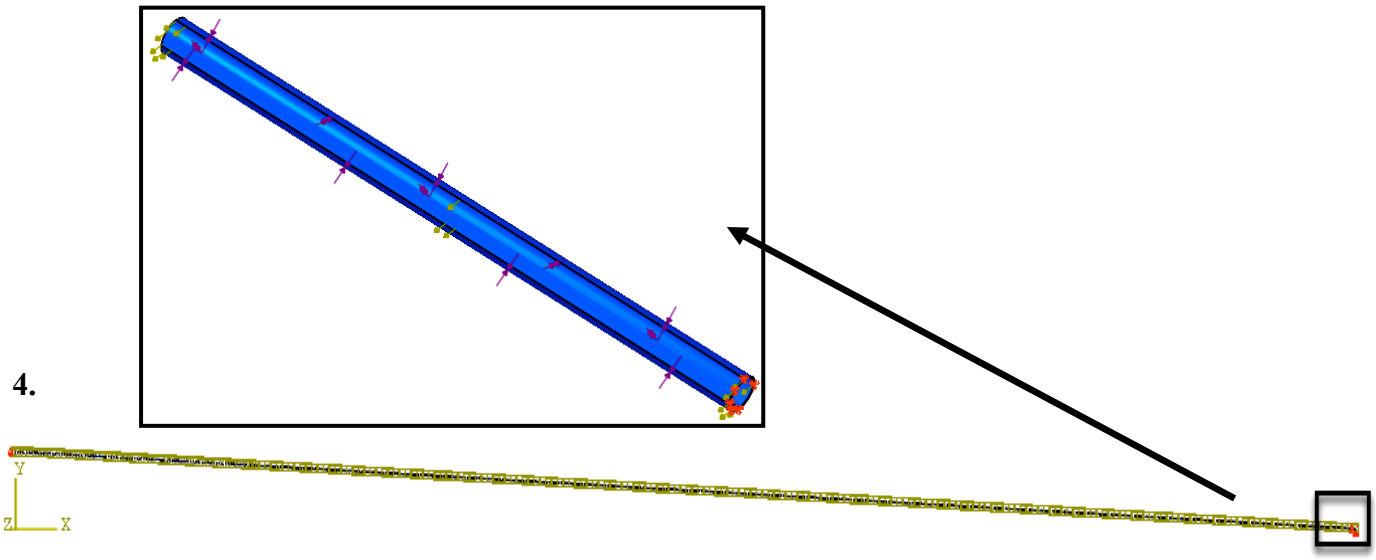

Figure 3. Close up view of loading and boundary condition of part of pipeline length

Verification

The same pipeline in Rathbone et al. [11] is selected to verify the proposed finite element model. The pipeline section properties, i.e. outside diameter and thickness, are equal to 508 mm and 23.1 mm, respectively. The geometric shape of the pipeline is shown in Figure 4.

buckling stage happens and it decreases quickly. As shown in Figure 5, the buckle initiation forces with $\theta = 4°$ and $\theta = 2°$ are 1.71 MN and 1.91 MN, respectively. The critical buckling forces in Rathbone et al. [11] are 1.738 MN and 1.966 MN and the relative error are 2.8% and 5.6%, respectively. Therefore, the proposed finite element model in this research can reach the true critical buckling force of snaked-lay pipelines.

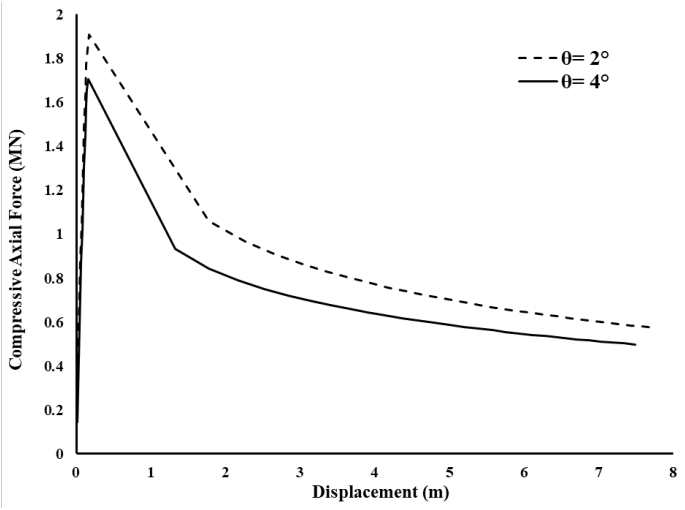

Figure 5. The axial compressive force versus the midpoint pipeline buckling amplitude

5. Factors Influencing the Initiation Force

In pipeline lateral global buckling analysis, there are several effective parameters investigated in this paper: thickness t, diameter D, internal pressure P, and temperature difference T. Obviously, these factors will affect the initiation force. The impact of these factors is revealed in the following analyses.

5.1. Internal Pressure and Temperature of Pipeline Content

Different combinations of pressures and temperatures are compared here. It is important to note that the value of hydrostatic pressure is fixed and it is equal to $1\ MPa$ to simulate the depth of $100\ m$. Figure 6 illustrates the resulting buckle shape from a full non-linear FE analysis that has been plotted for various temperature steps.

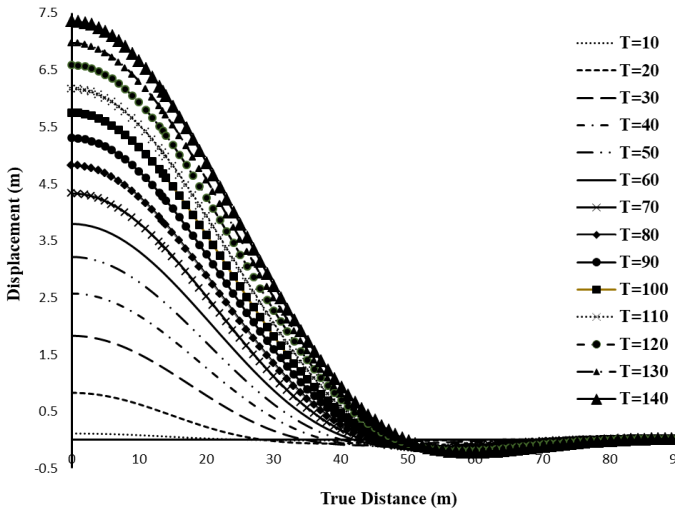

Figure 6. The buckle shape

It can be seen that about $90\ m$ of the investigated pipeline experienced buckling and the value of displacement grew with the increase in temperature. According to the lateral buckling mode shapes proposed by Hobbs [15], it is obvious that this pipeline is in mode 3. It should be noted that this figure displays the lateral displacement of a quarter of the pipeline starting from point zero on the horizontal axis.

In this study, three different temperatures are considered, i.e. 70℃, 120℃ and 170 ℃. The combination of each temperature with three different pressures, including $10\ MPa$, $20 MPa$ and $30\ MPa$, are investigated. It is significant to know that the values indicated for pressures are the difference between internal and external pressure. In this analysis, it is assumed that the section properties are fixed and the values of diameter and thickness are equal to $345\ mm$ and $16.195\ mm$, respectively. The results of this investigation are shown in Figures 7-9.

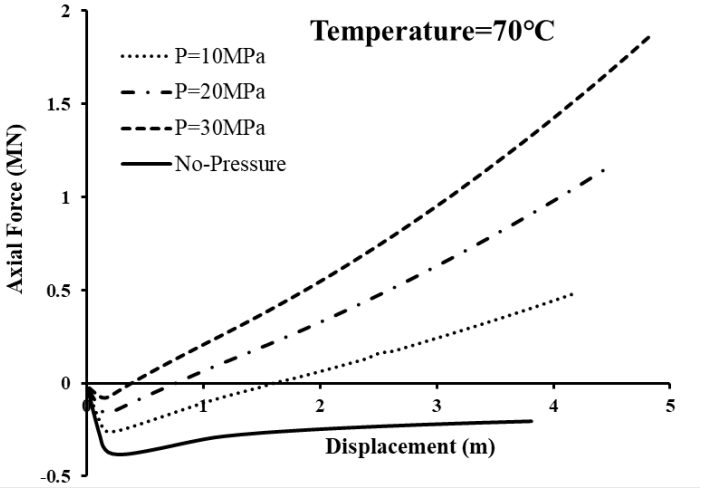

Figure 7. The change curve of buckling force for $T = 70$℃

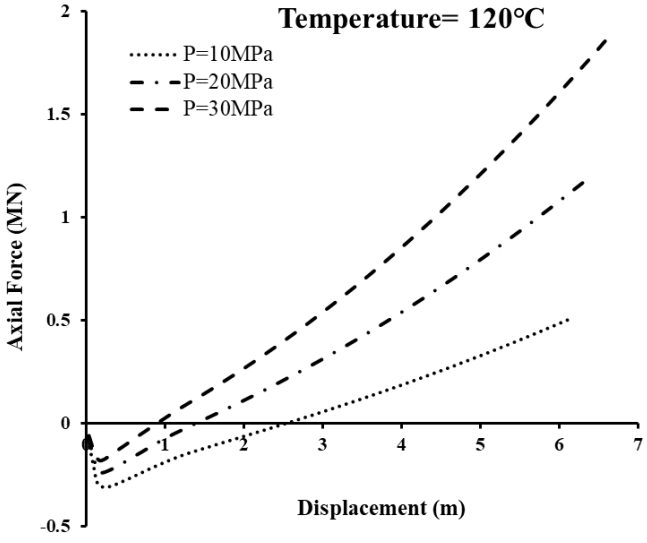

Figure 8. The change curve of buckling force for $T = 120$℃

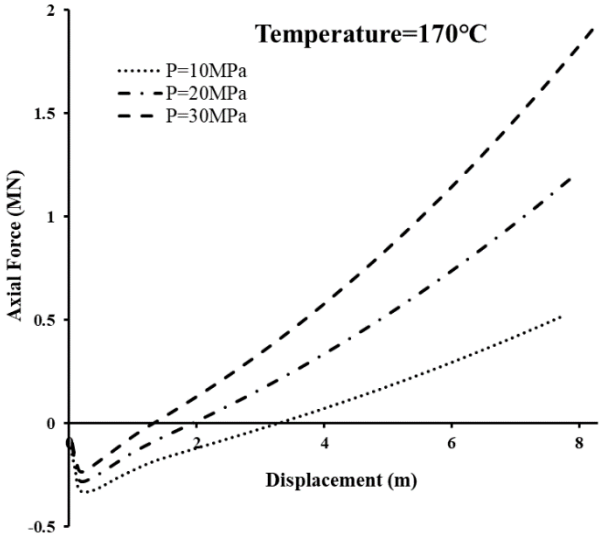

Figure 9. The change curve of buckling force for $T = 170$℃

In Figure 7, there are four curves, one of which is plotted for a condition in that external and internal pressures are not simulated. In order to have more accurate comparisons between the presented results, the initiation force of each curve is reported in Table 3.

Table 3. The comparison of the initiation force

Temperature difference (ΔT) [℃]	Pressure difference (ΔP) [MPa]	Compressive axial force [MN]
70	10	0.2585
	20	0.1581
	30	0.0776
120	10	0.3113
	20	0.2402
	30	0.1817
170	10	0.3241
	20	0.2799
	30	0.2349

The analysis of the results shows that:

a) By considering a fixed pressure difference, the compressive axial force is increased with the increase in temperature. In other words, at high temperatures, buckling occurs later. For example, if the pressure difference is assumed to be 30 MPa, the value of the critical axial force is increased by about 15% when the temperature varies from 70℃ to 170℃.

b) By assuming a fixed temperature difference, the buckling initiation force is decreased with the increase in pressure. To be more specific, buckling occurs sooner at high values of pressure. For example, if the temperature of the contents is considered 70℃, it can be seen that the value of the compressive axial force is decreased by about 18%, while the pressure varies from 10 MPa to 30 MPa.

In order to explain the two cases observed above in more detail, it is necessary to analyze pipeline forces more accurately, so the effect of pressure and temperature are described separately. When the pipeline is exposed to internal pressure, tensile stress develops in a hoop direction. Due to Poisson's effect, this hoop stress will tend to shorten the pipeline. Since this shortening is prevented by end constraints, the tensile stresses are increased. But, the effect of temperature is different, and the axial force gets into compression due to the thermal expansion when the pipeline is not allowed to move axially [21]. Since the final compressive axial force is a combination of temperature and pressure effects, an increase in the pressure will increase the tension stresses and consequently, it will decrease the compressive axial force, which is in agreement with obtained results but the temperature will build up the compressive axial force as supported by this study.

As shown in Figure 7, when the pressure difference is not simulated, buckling occurs at $0.3826\ MN$. By comparing this value with the initiation forces of Table 3, it is concluded that neglecting the effects of external and internal pressure is not a reasonable assumption and introduces imprecise results that are not useful in practical conditions.

For the pipeline analyzed in this section, the compressive axial force is calculated by Eq. (3) and the obtained value is compared with the FE results. Since the only effective parameters in the suggested equation are lateral friction factor, submerged weight, and lay radius and they are not influenced by pressure and temperature differences, the compressive axial force is fixed and it is equal to $0.349 MPa$. The maximum difference between analytical and numerical results is occurred in (70℃ , 30 MPa) which is about 27% and the minimum is occurred in (170℃ , 10 MPa) and it is equal to 2.5%. It is necessary to remind that in this study, friction factor is considered in lateral, axial and normal directions while lateral friction factor is the only effective parameter in Eq.(3) and other directions are ignored.

5.2. Effect of Pipeline Section Dimension

The pipeline section characteristics specify the flexural rigidity and influence stress and deformation [1]. Figures 10 and 11 illustrate the critical buckling force of the pipelines with different section dimensions by considering the temperature of 100 ℃ and pressure of 20 MPa.

In Figure 10, the effect of thickness is investigated and the buckling force curve is plotted by considering three different values of diameter. The results of FE simulations are compared with Eq. (3). In this section, the buckling force of Eq. (3) is not constant because the variation in thickness and diameter will influence the submerged weight.

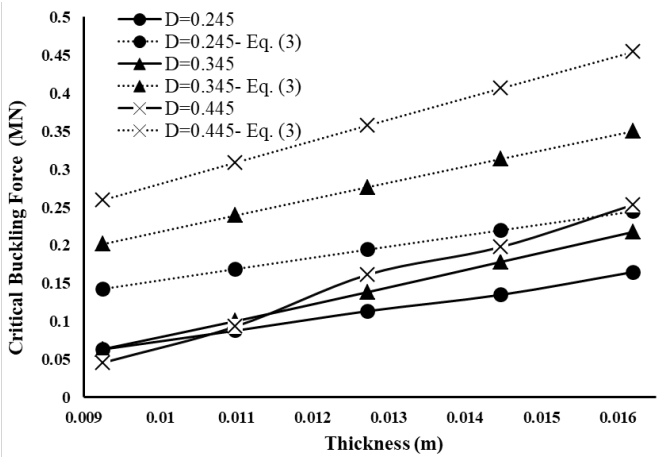

Figure 10. The critical buckling force of the pipelines for different thicknesses

It can be seen in Figure 10 that changes in t have a considerable effect on the critical buckling force so that with the increase in thickness, the critical buckling force is increased. Comparing the results of FE simulations with Eq. (3) illustrates that by increasing thickness, the differences between numerical and analytical results are approximately fixed and by growing diameter, it is increased. To be more specific, at low and high values of circumferential stiffness (ratio of diameter to thickness), differences are about 7% and 21%, respectively which minimum difference is occurred in diameter of 0.245 m and thickness of 0.00925 and maximum difference is occurred in diameter of 0.445 m and thickness of 0.016195.

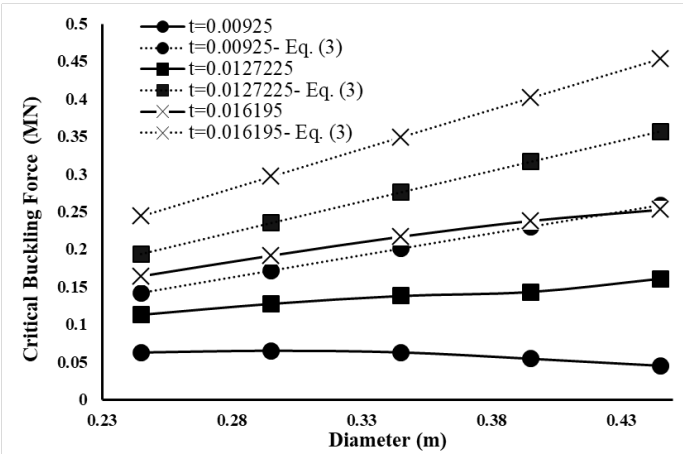

Figure 11. The critical buckling force of the pipelines for different diameters

It can be seen in Figure 11 that at lower thicknesses, changes in D does not have a considerable effect on the critical buckling force, but with the increase in thickness, the effect of diameter is increased and the critical buckling force grows. The differences between the analytical and numerical results increased with the increase in circumferential stiffness.

As a general conclusion, it was observed that by increasing thickness and diameter, the critical buckling force is increased and buckling happens later. This effect can be explained by the buckling behavior of beams and the value of critical buckling force is increased with the increase in the moment of inertia.

It is obvious that the numerical method yielded more conservative results versus the analytical method in both Figure 10 and Figure 11.

6. Conclusions

Deep offshore pipelines undergo lateral global buckling because of the HP/HT condition. The use of controlled lateral buckling methods such as snaked lay configuration triggers buckle at some predetermined locations. The common characteristic for the controlled lateral buckling is to reduce the buckle initiation force at the selected locations because in this condition the probability of buckling at the locations is increased and the rogue random buckles are prevented .

This paper investigated the effects of HP/HT loading and section properties on critical buckling force and compared analytical and numerical results. The main conclusions are as follows:

- The critical buckling force is increased with an increase in temperature and it is decreased with an increase in pressure. So, to increase the probability of buckling, the pipeline should experience higher pressures and lower temperatures.
- In most previous studies, it has been assumed that the effect of pressure difference can be equivalent to the temperature difference and it has the same effect, but this paper shows that there are significant differences between the obtained results, and the maximum value of this difference is reported at about 30.5% which is occurred in temperature and pressure difference of (70 ℃, 30 MPa).
- Critical buckling force is increased with an increase in diameter and thickness although changes in thickness have more considerable effects than the diameter.
- Comparing the results of the analytical and FE method illustrates that the proposed equation cannot calculate the critical buckling force with good accuracy and in most investigations, it experiences considerable differences with numerical results which are reported to be about 27%.

7. Acknowledgment

The authors are grateful for the support of the Iranian Offshore Oil Company (IOOC).

8. References

1- Z. Hong, R. Liu, W. Liu, and S. Yan, (2015), *A lateral global buckling failure envelope for a high temperature and high pressure (HT/HP) submarine pipeline*, Applied Ocean Research, Vol. 51, p. 117-128.

2- Z. Wang, Z. Chen, Y. He, and H. Liu, (2015), *Optimized configuration of snaked-lay subsea pipelines for controlled lateral buckling method*, in The Twenty-fifth International Ocean and Polar Engineering Conference.

3- D. Bruton, M. Carr, M. Crawford, and E. Poiate, (2005), *The safe design of hot on-bottom pipelines with lateral buckling using the design guideline developed by the safebuck joint industry project*, in Proceedings of the Deep Offshore Technology Conference, Vitoria, Espirito Santo, Brazil.

4- J. O. Rundsag, K. Tørnes, G. Cumming, A. D. Rathbone, and C. Roberts, (2008), *Optimised Snaked Lay Geometry*., in Eighteenth International Offshore and Polar Engineering Conference, International Society of Offshore and Polar Engineers.

5- Z.-G. Li, C. Wang, N. He, and D.-Y. Zhao, (2008), *An overview of deepwater pipeline laying technology*, *China Ocean Engineering,* Vol. 22, no. 3,p. 521-532.

6- W. Liu and J. Fu, (2018), *Global Buckling Behavior of Snaked-Laid and Straight Laid Subsea Pipelines*, in the 28th International Ocean and Polar Engineering Conference.

7- J. Guan, P. R. Nystrom, and H. F. Hansen, (2007), *Optimized solutions to control lateral buckling of pipelines with snaked-lay: theoretical and numerical studies*, in ASME 2007 26th International Conference on Offshore Mechanics and Arctic Engineering.

8- I. Matheson, M. Carr, R. Peek, P. Saunders, and N. George, (2008), *Penguins flowline lateral buckle formation analysis and verification*, in ASME 2004 23rd International Conference on Offshore Mechanics and Arctic Engineering.

9- M. Wagstaff, (2003), *Detailed design and operational performance assessment of pipeline buckle initiators to mitigate lateral buckling*, in Proceedings of the Petromin Pipeline Conference, Singapore.

10- R. Preston, F. Drennan, and C. Cameron, (1999), *Controlled lateral buckling of large diameter pipeline by snaked lay*, in The Ninth International Offshore and Polar Engineering Conference.

11- A. Rathbone, K. Tørnes, G. Cumming, C. Roberts, and J. Rundsag, (2008), *Effect of lateral pipelay imperfections on global buckling design*, in The Eighteenth International Offshore and Polar Engineering Conference.

12- G. Cumming and A. Rathbone, (2010), *Euler buckling of idealised horizontal pipeline imperfections*, in ASME 2010 29th International Conference on Ocean, Offshore and Arctic Engineering.

13- I. Obele, (2013), *Lateral buckling and axial walking of surface laid subsea pipeline*, Master's thesis, University of Stavanger, Norway.

14- Y. Liu, X. Li, and J. Zhou, (2013), *Post-buckling studies on snaked-lay pipeline with new shape*, Journal of information & computational science, Vol. 9(12), p. 3315-24.

15- R. E. Hobbs, (1984), *In-service buckling of heated pipelines*, Journal of Transportation Engineering., Vol. 110(2), p.175-89.

16- N. Taylor and A. Gan, (1986), *Refined modelling for the lateral buckling of submarine pipelines*, Journal of Constructional Steel Research, Vol. 6(2), p.143-62.

17- H. Karampour, F. Albermani, and J. Gross, (2013), *On lateral and upheaval buckling of subsea pipelines*, Engineering structures, Vol. 52, p.317-330.

18- Z. Hong, R. Liu, W. Liu, and S. Yan, (2015), *Study on lateral buckling characteristics of a submarine pipeline with a single arch symmetric initial imperfection*, Ocean engineering, Vol. 108, p.21-32.

19- Y. Zhang, D. Yi, Z. Xiao, and Z. Huang, (2015), *Engineering critical assessment for offshore pipelines with 3-D elliptical embedded cracks*, Engineering Failure Analysis, Vol. 51(1), p.37-54.

20- Hibbitt, Karlsson, and Sorensen, (2013), ABAQUS/STANDARD. User's Guide and Theoretical Manual, Version 6.13, 2013.

21- O. Fyrileiv and L. Collberg, (2005), *Influence of pressure in pipeline design: effective axial force*, in ASME 2005 24th International Conference on Offshore Mechanics and Arctic Engineering.